



UNIVERSITY OF TRENTO
DEPARTMENT OF PHYSICS
MASTER'S DEGREE IN PHYSICS

~ · ~

ACADEMIC YEAR 2023–2024

Time-resolved optical emission spectroscopy in CO₂ nanosecond pulsed discharges

Supervisors

Prof. Luca Matteo MARTINI
Prof. Paolo TOSI

Graduate Student

Alberto APPOLONI
247215

FINAL EXAMINATION DATE: 20/03/2025

Abstract

Nanosecond repetitively pulsed discharges at atmospheric pressure have demonstrated relatively high efficiency in the conversion of CO₂ to CO and O₂. However, the underlying mechanisms governing CO₂ dissociation in these transient discharges remain a subject of ongoing investigation.

This thesis investigates the temporal progression of a CO₂ nanosecond repetitively pulsed (NRP) discharge with time-resolved optical emission spectroscopy (OES). The primary objective is to characterize the temporal evolution of emitting species and gain insights into the underlying physical and chemical processes governing CO₂ dissociation.

One of the most relevant phenomena that NRP discharges have to account for is the reflections of electrical signals at the end of the transmission line caused by differences in the impedance of the conductors involved (impedance mismatching). Due to impedance mismatching in the transmission line, multiple current rebounds and retriggering events occur, leading to distortions in the optical emission profiles of the emitting species. This prevents a clear distinction of their temporal evolution. To address this issue, a new experimental setup was designed to minimize retriggering and impedance mismatching, ensuring precise control over the discharge conditions.

Initially, the results of Cepelli et al. [1] were successfully reproduced, with the additional identification of a previously unassigned oxygen emission, further confirming the validity of the experimental approach.

The optical emission at the cathode was then analyzed, revealing distinct temporal behaviors for atomic species and atomic ions. Furthermore, by implementing an impedance-matching resistance of 80 Ω with a discharge gap of 2.4 mm, reflections were significantly reduced in the second pulse of a two-pulse burst, enabling a more accurate assessment of the emission dynamics.

Time-resolved spectra were recorded at multiple time delays, with a selection of 20 ns, 100 ns, and 200 ns presented to examine the evolution of key species such as C, C⁺, C⁺⁺, and O. The results indicate that molecular emissions and ionic atoms dominate at early times, while atomic emissions become more prominent as the discharge evolves. The presence of residual ionization between pulses suggests a memory effect influencing the breakdown voltage and discharge characteristics.

Contents

1	Introduction	5
1.1	Evidence of climate change	5
1.2	CO ₂ as the main driver	6
1.3	Renewable energies: strengths and limitations	10
1.4	Storing energy	11
1.5	Non-Thermal plasmas	15
1.6	CO ₂ dissociation pathways	17
1.7	Nanosecond repetitively pulsed discharges	20
1.8	This thesis	22
2	Spectroscopy	23
2.1	Plasma diagnostic techniques	23
2.1.1	Optical emission spectroscopy	23
2.1.2	Absorption spectroscopy	25
2.2	Spectral Line Characteristics	25
2.2.1	Broadening mechanisms	27
2.2.2	Bremsstrahlung and recombination radiation	27
2.3	Energy levels nomenclature	28
2.3.1	Atoms	28
2.3.2	Molecules	29
2.4	Spectroscopic Instrumentation	31
2.5	Calibration	33
3	Experimental Setup	35
3.1	Setup	35
3.2	Electrical diagnostics	38

3.2.1	Electrical noise	41
3.3	Gas handling	42
3.4	Optical diagnostics	44
3.4.1	Lenses	44
3.4.2	Spectrograph	47
3.4.3	Spectrum calibration	51
3.4.4	Spectra noise	53
4	Data Analysis	55
4.1	Delay and parasitic line capacitance calculation	55
4.2	Temporal jitter	57
4.3	Impedance matching	59
4.3.1	Impedance matching	59
4.3.2	Dependence of Circuit Resistance on Voltage Maximum	61
4.3.3	Dependence of Impulse Time Delay on Impedance matching	62
5	Results	65
5.1	TR-OES	65
5.2	TR-OES - unmatched in impedance	66
5.3	TR-OES - unmatched in impedance cathode	75
5.4	TR-OES unmatched burst	76
5.5	TR-OES matched burst	82
6	Conclusions and future perspectives	99
7	Appendix	101

Chapter 1

Introduction

1.1 Evidence of climate change

The climate crisis has become undeniable, with reports of record-breaking global temperatures and frequent extreme weather events now an almost routine part of daily news. This steady escalation highlights one of the gravest challenges of our era: the accelerating impacts of anthropogenic climate change. The sharp rise in greenhouse gas (GHG) atmospheric concentrations, particularly carbon dioxide (CO_2), is the main cause, driven largely by human activities since the Industrial Revolution. The atmospheric CO_2 concentration, which historically fluctuated between approximately 200 and 280 parts per million (ppm) during the pre-industrial era, has risen sharply, exceeding 420 ppm as of 2023, as illustrated in Figure 1.1 [2].

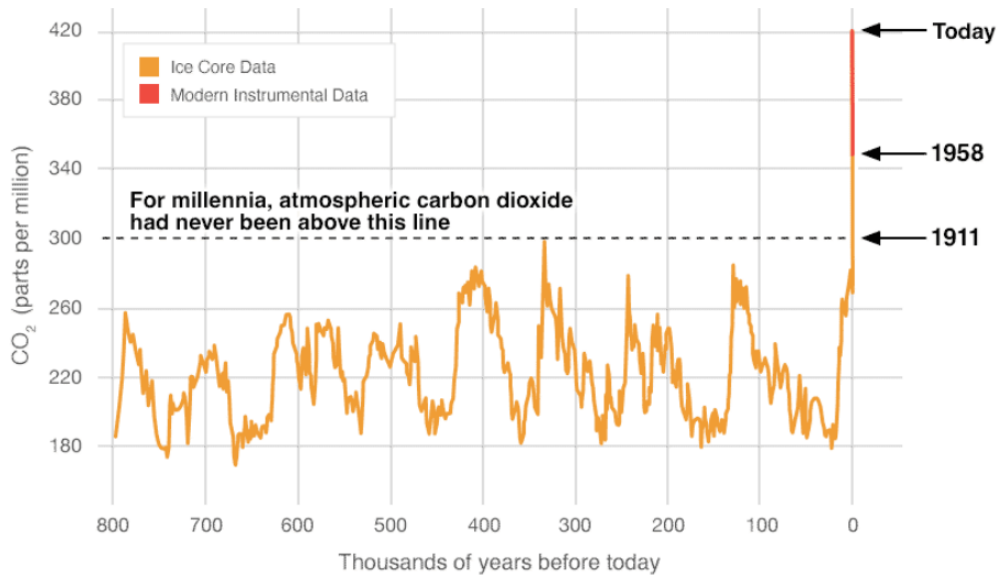


Figure 1.1: CO_2 concentration in the last millenia. Figure reported by [2]

This represents an unprecedented 50% increase compared to pre-industrial levels, disrupting the delicate balance of Earth's carbon cycle. Such a drastic alteration is primarily attributed to the combustion of fossil fuels, industrial processes, as well as deforestation. The Intergovernmental Panel on Climate Change (IPCC) has conclusively identified human activity as the dominant driver of global warming, with the current rate of CO_2 increase occurring at a speed unmatched in Earth's geological history[3].

1.2 CO_2 as the main driver

The greenhouse effect is a process crucial to maintaining the earth's temperature stability and, consequently, its climate. This phenomenon occurs because greenhouse gases (GHGs) absorb and re-emit infrared radiation, preventing heat from escaping directly into space.

CO_2 is pivotal in the greenhouse effect, which regulates Earth's climate by maintaining a stable surface temperature. Greenhouse gases (GHGs) absorb and re-emit infrared radiation, limiting the rate at which heat escapes into space.

Earth receives solar energy primarily as shortwave radiation. Clouds and other reflective surfaces reflect some of this energy while the surface absorbs the rest, which warms up and emits infrared radiation. Atmospheric components, including GHGs and clouds, intercept much of this radiation and re-radiate it both upward and downward, amplifying the Sun's warming influence and sustaining life. A stable climate requires the outgoing

heat radiation to balance incoming solar energy. At Earth's distance from the Sun, the average energy flux is about 341 W/m^2 , with roughly 30% reflected back into space. Of the remaining energy, the atmosphere absorbs approximately 78 W/m^2 , allowing 161 W/m^2 to reach the surface, while GHGs and clouds contribute about 333 W/m^2 of back radiation. Consequently, the surface emits around 396 W/m^2 , exceeding the energy leaving the top of the atmosphere by 157 W/m^2 —a phenomenon known as greenhouse trapping [4].

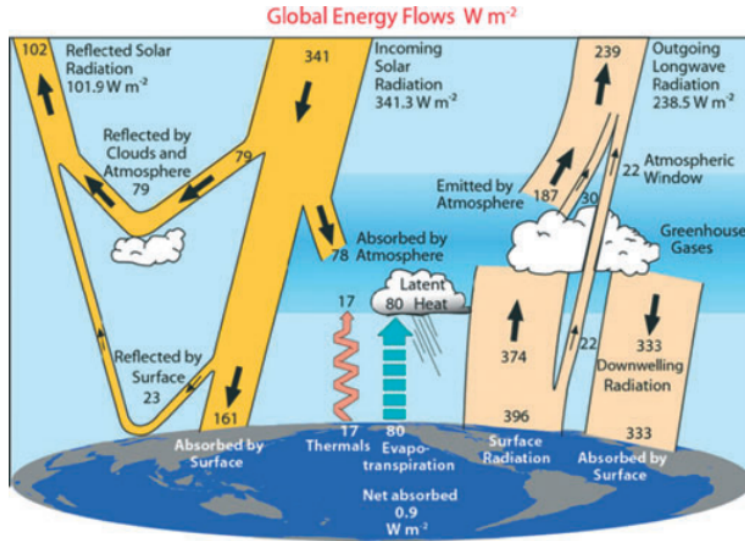


Figure 1.2: The global climate system's annual mean energy budget. Figure reported from [4]

Human activities have significantly increased the concentration of CO_2 , intensifying the greenhouse effect and leading to a net positive radiative forcing. This enhancement has already resulted in an approximate 1.1°C rise in Earth's average temperature since pre-industrial times, with projections indicating an additional increase of 2°C or more by the century's end if current trends persist.

Although CO_2 is the primary driver of anthropogenic global warming, other greenhouse gases also contribute to this effect. Methane (CH_4) and nitrous oxide (N_2O), despite their lower concentrations, have significantly higher global warming potentials and are primarily emitted through agricultural and industrial activities. Water vapor (H_2O), while the most abundant greenhouse gas, acts as a feedback mechanism rather than a direct driver of climate change. Its concentration responds rapidly to temperature changes, amplifying the warming effect initiated by other GHGs. Still, it has a short atmospheric residence time of approximately 9 days, maintaining a relatively stable average concentration. Beyond these direct contributions, feedback mechanisms further amplify the impacts of greenhouse

gas emissions. For instance, as global temperatures rise, the melting of polar ice reduces Earth's albedo, leading to greater absorption of solar radiation and accelerating warming. Permafrost thawing releases stored methane and CO₂, leading to a positive feedback loop that exacerbates warming. The capacity of oceans, which currently absorb approximately half of anthropogenic CO₂ emissions, is also at risk of saturation, diminishing their role as a carbon sink. These feedback effects underscore the urgency of addressing not only emissions but also the atmospheric accumulation of greenhouse gases.

Fortunately, the trapping of the outgoing infrared radiation by the CO₂ absorption bands is not directly proportional to concentration but follows a logarithmic relationship. The extent to which radiation is trapped in the Earth's atmosphere is largely influenced by the types of gases present and their spectral properties. While nitrogen and molecular oxygen, the main components of the atmosphere, do not absorb infrared radiation, carbon dioxide and water vapor are critical greenhouse gases. Figure 1.3 illustrates the infrared absorption characteristics of pure H₂O and CO₂ at a pressure of 600 mbar and a temperature of 250 K. The absorption spectrum of water vapor (black curve) exhibits broad absorption bands, with significant absorption in the far-infrared region ($\lambda > 15 \mu\text{m}$) and around 6.3 μm . These features create regions of comparatively lower absorption near 12 μm and 4 μm . Conversely, CO₂ displays distinct absorption peaks near 15 μm and 4.3 μm , which fall within spectral windows of H₂O absorption. This spectral distribution indicates that CO₂ and H₂O absorb infrared radiation in complementary spectrum regions.

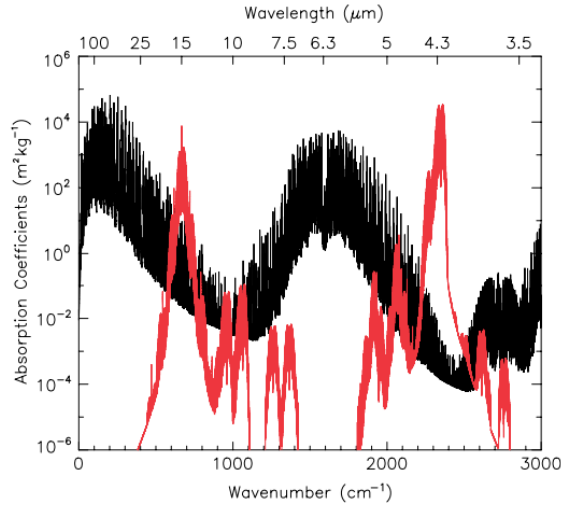


Figure 1.3: Absorption coefficients have been calculated using a line-by-line radiative transfer model (Francis and Edwards, 2007) applying the HITRAN2004 spectral database to water vapour (black curve) and carbon dioxide (red curve) as a function of wavenumber or wavelength. The horizontal scale is given in linear wavenumber (cm^{-1} , lower axis) to produce a plot where the area corresponds to the energy flux. The equivalent wavelength is shown on the top axis. HITRAN (high-resolution transmission molecular absorption) is a widely used spectroscopic database for modeling atmospheric radiation transmission and emission. Figure reported by [5]

Figure 1.4 illustrates the role of atmospheric gases in absorbing and trapping radiation, as observed in the top-of-atmosphere (TOA) radiative flux spectrum. This spectrum, computed for a cloud-free atmosphere, incorporates global average concentrations of H₂O, O₃, CO₂, CH₄, and N₂O. Additionally, the figure presents blackbody radiation curves corresponding to different temperatures, with the red curve representing the Earth's surface temperature of 287.13 K. The TOA spectrum would coincide with this blackbody curve in the hypothetical absence of atmospheric absorption. . However, deviations in the black curve highlight wavelengths where greenhouse gases effectively absorb radiation emitted from the surface, subsequently re-emitting it from cooler atmospheric layers([5]).

Significant departures from the surface-emitted radiation occur particularly around 15 μm , where CO₂ absorption is most pronounced, coinciding with the peak emission wavelength for Earth's temperature. Another major absorption feature is observed near 9.6 μm due to O₃. While CO₂ also exhibits absorption at 4.3 μm , its impact on the radiative balance is comparatively minor due to its position away from the peak blackbody emission. These spectral characteristics collectively validate radiative transfer theory and demonstrate excellent agreement with satellite observations of Earth's infrared spectrum, thereby corroborating the accuracy of spectral line databases.[5]

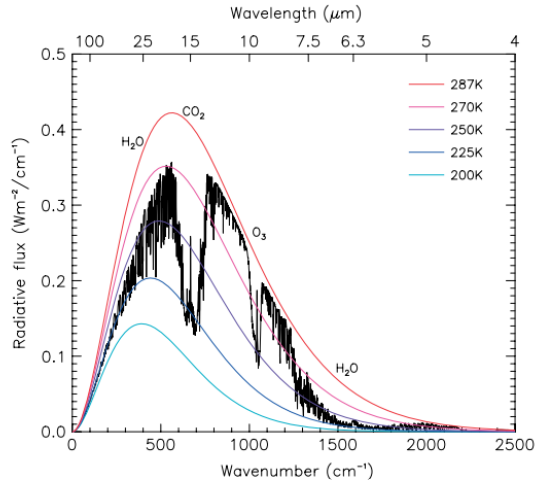


Figure 1.4: The black curve shows a model-generated spectrum of the infrared radiative flux emitted to space from the top of the atmosphere (OLR). Coloured lines indicate blackbody spectra at different temperatures (see legend). Notable reductions in OLR due to absorption bands are marked: the H_2O rotation bands ($0\text{-}540\text{ }cm^{-1}$), the CO_2 $15\text{ }\mu m$ band ($550\text{-}800\text{ }cm^{-1}$), the O_3 $9.6\text{ }\mu m$ band ($980\text{-}1100\text{ }cm^{-1}$), and the H_2O $6.3\text{ }\mu m$ band ($1400\text{-}1800\text{ }cm^{-1}$). Figure reported by [5]

Faced with these escalating challenges, mitigating climate change requires a multi-faceted approach, with the reduction of atmospheric CO_2 levels emerging as a critical priority. Traditional mitigation strategies, such as transitioning to renewable energy sources and enhancing carbon sinks through reforestation, are indispensable but may not be sufficient to achieve the rapid reductions necessary to meet global climate targets. This has spurred significant interest in innovative technologies capable of directly addressing atmospheric CO_2 .

1.3 Renewable energies: strengths and limitations

Renewable energy sources (RES) have emerged as a cornerstone of sustainable development, offering the potential to meet global energy demands while minimizing environmental impacts. Solar energy, for instance, delivers an annual potential of approximately 173,000 TW[6], vastly surpassing the current global energy consumption of around 20 TW [7]. Wind, geothermal, and hydroelectric power further enrich the portfolio of clean energy options, collectively representing a viable pathway to decarbonizing the energy sector. However, despite their promise, the large-scale adoption of renewable energy technologies faces a variety of technical, economic, and logistical challenges that must be resolved to achieve a sustainable energy future [8].

One of the most critical issues impeding the widespread deployment of RES is their in-

herent temporal variability. Solar and wind energy are both characterized by intermittent generation patterns driven by diurnal, seasonal, and weather-related fluctuations. This variability poses significant difficulties for grid operators, who must balance supply and demand to ensure a reliable and consistent power supply. The lack of predictable output from renewable sources requires advanced forecasting techniques, sophisticated grid management systems, and, most importantly, efficient energy storage solutions to smooth out fluctuations and maintain grid stability.

Spatial constraints present another obstacle. Renewable energy systems often require significant land and resource allocation to achieve meaningful energy output due to their low energy density. Furthermore, there is frequently a geographical mismatch between regions rich in renewable energy potential—such as areas with abundant sunlight or high wind speeds—and densely populated urban centers where energy demand is highest. Addressing these spatial and geographical challenges necessitates the development of extensive transmission infrastructure and strategic planning to connect energy-rich regions to demand centers.

In addition to these physical challenges, the integration of RES into existing energy systems requires significant technological adaptation. Traditional electrical grids were designed to support centralized, fossil fuel-based power generation. Transitioning to decentralized and distributed renewable energy systems demands the development of smart grids equipped with advanced monitoring, control, and energy distribution capabilities. Upgraded transmission networks and efficient storage technologies are essential to enable seamless integration and maximize the utility of renewable energy sources.

1.4 Storing energy

Energy storage systems play a pivotal role in overcoming the limitations of RES. By decoupling energy generation and consumption temporally, storage technologies allow surplus energy to be captured during periods of high production and released during periods of low availability. Despite their critical importance, current energy storage technologies remain a bottleneck in renewable energy deployment, spurring intense research efforts to identify, develop, and optimize new storage solutions.

A diverse array of energy storage technologies exists, each suited to different applications and requirements. Electrochemical storage systems, such as lithium-ion batteries, dom-

inate the energy storage landscape, offering scalability and adaptability. However, batteries are constrained by relatively low gravimetric and volumetric energy densities, long recharge times, and limited cycle lifespans. Mechanical storage solutions, such as pumped hydroelectric systems and compressed air energy storage, offer large-scale capacity but are geographically constrained. Emerging alternatives include thermal storage, which stores energy as heat for later use, and chemical storage, such as hydrogen production via water electrolysis or synthetic fuels. Each approach has its strengths and limitations, underscoring the need for tailored solutions to meet specific energy demands across various sectors, from transportation to stationary grid applications.

Direct electrification remains the preferred method for decarbonization wherever feasible. However, certain sectors—such as aviation and long-haul transportation—demand energy storage solutions with high energy densities and rapid recharge capabilities.

Power-to-X (PtX) encompasses a range of technologies that convert surplus renewable electricity into chemical energy carriers, enabling long-term energy storage and sector integration [9]. These processes include power-to-gas, power-to-fuels, and power-to-chemicals, which produce substances such as hydrogen, synthetic hydrocarbons, and ammonia. By storing energy in chemical bonds, PtX offers a versatile complement to conventional storage methods like batteries.

Among PtX approaches, power-to-fuels (PtF) focuses on converting renewable electricity into synthetic fuels such as methane, methanol, or liquid hydrocarbons. These fuels can be used in industry, electricity generation, and transportation, offering a pathway to decarbonize sectors that aren't easily reached by the electrical network [10].

A key benefit of e-fuels is their ability to achieve net-zero CO₂ emissions when produced from renewable energy and captured CO₂, as the CO₂ released during combustion is offset by the CO₂ used in their synthesis. By integrating intermittent renewable energy sources into fuel production, PtF plays a critical role in the transition to a sustainable energy system.

The energy densities of various fuels are critical factors in their selection for applications requiring efficient energy storage and transportation. Hydrogen is recognized for its high gravimetric energy density, offering ≈ 141 MJ/kg in its gaseous form at 700 bar, far surpassing gasoline (≈ 44 MJ/kg), diesel (≈ 45 MJ/kg), and methanol (≈ 20 MJ/kg). However, its low volumetric energy density of ≈ 0.53 MJ/L in the gas phase presents challenges, particularly for applications where compact storage is crucial. In contrast,

liquid hydrogen, with a volumetric energy density of $\approx 8 \text{ MJ/L}$, addresses this issue but requires cryogenic storage, adding complexity and energy costs. Conventional fuels such as gasoline and diesel offer much higher volumetric energy densities ($\approx 35 \text{ MJ/L}$ and $\approx 38 \text{ MJ/L}$, respectively), making them more practical for many applications (Figure 1.5) [11].

Energy Density

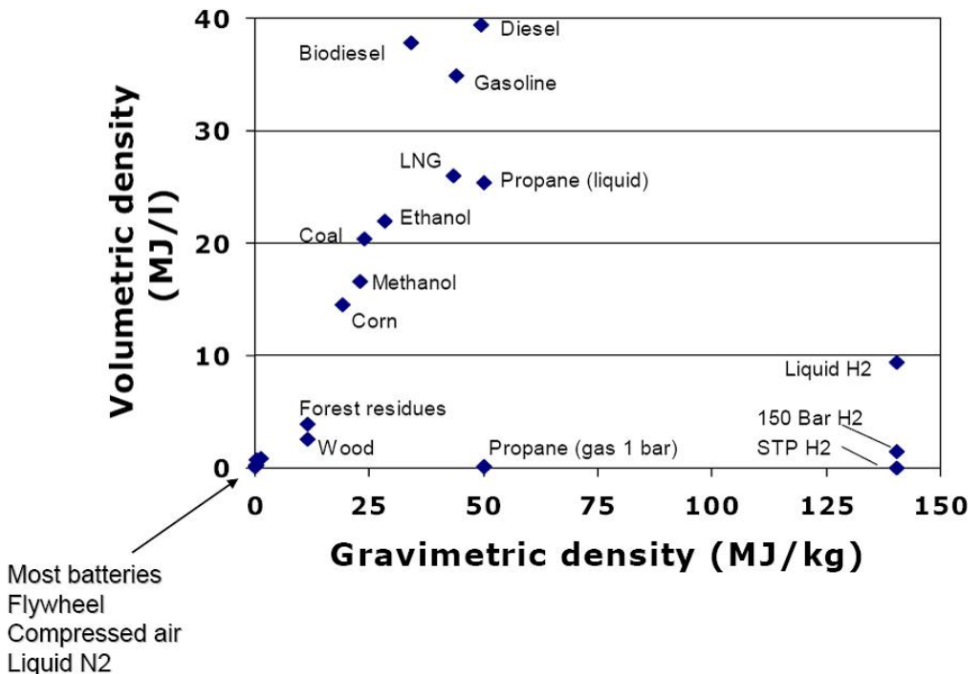
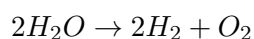


Figure 1.5: Volumetric Versus gravimetric energy density of different hydrocarbon fuels [12].

Thus, while hydrogen's gravimetric energy density is advantageous, its volumetric density is a limiting factor, necessitating advanced storage methods like compression or liquefaction. Nonetheless, hydrogen remains an important energy carrier, especially when produced from renewable sources through processes like water electrolysis:



Hydrogen produced via electrolysis offers a sustainable method for energy storage and usage, particularly when coupled with intermittent renewable sources like wind and solar. Moreover, transitioning to a hydrogen-based economy would require extensive infrastructure changes, including new storage and transportation systems. Although hydrogen plays a crucial role in the renewable energy landscape, its widespread deployment is often limited to niche applications, such as aerospace and heavy industry, where its mass-to-energy

ratio offers distinct advantages.

Nobel Prize George Olah proposed an innovative alternative: leveraging renewable electricity to synthesize liquid carbon-based fuels, commonly termed "solar fuels" or e-fuels, using CO₂ as the primary carbon source[13]. These fuels are carbon-neutral when derived from recycled CO₂, enabling their use as a sustainable replacement for fossil fuels.

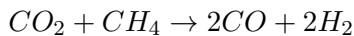
Key processes in solar fuel production include:

- **Methanol Production:**



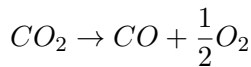
Methanol is a versatile liquid fuel with numerous advantages. It is easy to store, transport, and use in existing fuel infrastructures. Methanol can power internal combustion engines or be converted into electricity via fuel cells. Additionally, it serves as a precursor for producing dimethyl ether (DME), a potential substitute for diesel fuel.

- **Syngas Production:**



This reaction produces syngas, a mixture of carbon monoxide (CO) and hydrogen. Syngas can subsequently be transformed into liquid hydrocarbons through the Fischer-Tropsch process.

- **Carbon Monoxide Generation:**



This approach generates carbon monoxide (CO), which can be utilized as a feedstock for fuel synthesis, further expanding the range of carbon-neutral energy options.

Compared to conventional batteries or compressed hydrogen, synthetic fuels exhibit superior energy density and compatibility with existing infrastructure. For example, methanol provides an energy density of approximately 20 MJ/kg, vastly exceeding the 0.6–0.9 MJ/kg range of lithium-ion batteries. Furthermore, combining synthetic fuel production with carbon capture technologies enables a closed-loop carbon cycle, facilitating

CO₂ recycling and reducing net emissions. Innovative approaches are already being implemented in regions with abundant renewable energy resources, such as Iceland. Carbon Recycling International utilizes geothermal energy to produce hydrogen via water electrolysis and subsequently combines it with CO₂ to synthesize methanol. This system effectively transforms Iceland's clean, renewable energy into a valuable export commodity, exemplifying the potential for integrating renewable energy and synthetic fuel technologies.[14]

1.5 Non-Thermal plasmas

Despite their potential, the production of synthetic fuels through conventional methods involves several challenges:

- High-Temperature Requirements: Many of the key reactions, such as CO₂ hydrogenation and dry reforming, are strongly endothermic and require temperatures exceeding 1000 K for efficient conversion.
- Thermal Energy Losses: The reliance on heat as the primary energy input results in significant inefficiencies due to dissipation.
- Large-Scale Infrastructure: Traditional processes are typically conducted in large, centralized industrial plants, limiting their applicability to decentralized or small-scale energy systems.

In thermochemical processes, the energy required to drive chemical reactions is typically supplied as heat, which is then distributed uniformly across all molecular degrees of freedom. This indiscriminate energy distribution often results in significant heat losses. In contrast, non-thermal plasmas (NTPs), also known as non-equilibrium or cold plasmas, enable the selective activation of chemical reactions while maintaining a relatively low overall gas temperature. In these systems, energy is primarily directed toward specific molecular degrees of freedom that are critical for the desired reactions, rather than being wasted as generalized heating.

Non-thermal plasmas are generated through electrical discharges in gaseous media. Since these plasmas are powered by electricity, they can seamlessly integrate with renewable energy sources (RES), such as wind or solar power. This compatibility extends

beyond energy sourcing: the low switch-on/off inertia of NTPs allows them to respond rapidly to the intermittency and variability of renewable energy supplies, making them highly adaptable for modern energy systems.

The ignition of a plasma discharge requires the application of a sufficiently high voltage to accelerate free electrons within the gas. These electrons must gain enough kinetic energy to ionize gas molecules upon collision. The ionization process leads to the creation of positively charged ions, which are accelerated toward the cathode. Upon reaching the cathode, these ions induce secondary electron emissions, which further amplify the electron population. This cascading effect establishes a self-sustaining plasma state capable of driving high-energy chemical transformations.

Thermodynamic equilibrium is established when the energy distribution across all degrees of freedom in a system is uniform, represented by a single temperature, T_{eq} . This occurs when the rate of energy supply to the system is slow enough to allow complete redistribution among molecular degrees of freedom. In contrast, when energy redistribution is hindered—for instance, by operating under low-pressure conditions or by rapidly supplying energy—a single equilibrium temperature no longer applies, resulting in non-equilibrium conditions.

In non-thermal plasmas, the energy from the electric field primarily accelerates electrons due to their significantly lower mass compared to ions. Collisions between electrons and heavier species, such as ions or neutrals, are largely elastic, causing electrons to change direction without substantial energy loss. This inefficiency arises because the mass ratio $m_e/m_{\text{ion}} \sim 10^{-4}$ heavily favors electrons retaining their kinetic energy. In contrast, ions, with masses comparable to neutrals, readily lose energy during collisions. Consequently, ions gain energy primarily through acceleration in the electric field between successive collisions.

The processes of energy transfer in non-thermal plasmas are highly dependent on inelastic collisions, which are energy-specific. Once electrons acquire sufficient energy, they can excite internal molecular modes, such as electronic, vibrational, or rotational states, and induce ionization or dissociation of molecules. The specific cross-sections of these processes and the electron energy distribution function (EEDF) govern which atomistic degrees of freedom are selectively excited.

While temperature typically presupposes equilibrium, the mean energy associated with

each degree of freedom is often expressed as a temperature in plasma physics. Non-thermal plasmas thus exhibit a hierarchy of temperatures[15]:

$$T_{\text{el}} > T_{\text{vib}} > T_{\text{ion}} \sim T_{\text{rot}} \sim T_{\text{gas}},$$

where T_{el} , T_{vib} , T_{ion} , T_{rot} , and T_{gas} represent the electronic, vibrational, ionic, rotational, and translational (gas) temperatures, respectively. Typical values might range from $T_{\text{el}} \sim 10^4 - 10^5$ K, $T_{\text{vib}} \sim 10^3 - 10^4$ K, and $T_{\text{gas}} \sim 300$ K.

Under such non-equilibrium conditions, electron kinetics are described by solving the Boltzmann equation, leading to non-Maxwellian electron energy distribution functions and non-Boltzmann vibrational energy distribution functions [15].

1.6 CO₂ dissociation pathways

Non-equilibrium conditions in plasmas can drive strongly endothermic reactions, such as CO₂ dissociation, at relatively low temperatures. Three distinct dissociation pathways are possible depending on the electron energy distribution function (EEDF), as illustrated schematically in Figure 1.6.

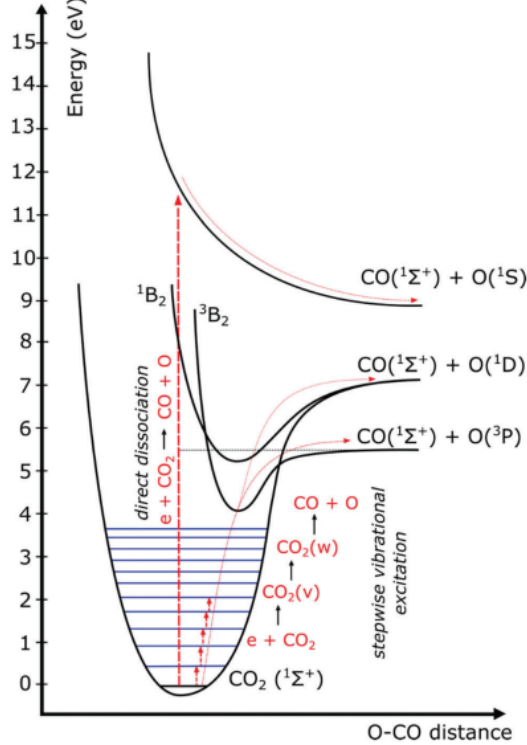
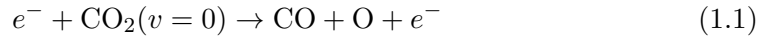


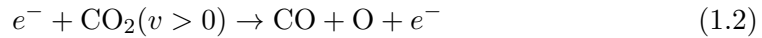
Figure 1.6: Potential energy for CO_2 dissociation and different pathways. Figure reported from [8]

These pathways include:

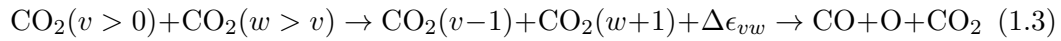
1. Direct electron impact dissociation:



2. Electron impact dissociation from vibrationally excited levels:



3. Vibrational excitation (vibrational ladder climbing):



Here, v and w denote vibrational states of the asymmetric mode, while $\Delta\epsilon_{vw}$ represents the positive energy defect arising from the anharmonicity of the molecular potential well. The dissociation energy of CO_2 from the ground state is 5.5 eV. Direct electron impact dissociation (Equation 1.1) requires electrons with energy exceeding 7 eV to promote the

molecule from the ground state to the first dissociative state[8]. The energy surplus, dissipated as heat, reduces the overall efficiency of this pathway. By contrast, dissociation via vibrationally excited levels (Equation 1.2) demands a lower energy surplus, making it more efficient. The most energy-efficient mechanism, vibrational ladder climbing (Equation 1.3), ideally requires only the minimum energy corresponding to the depth of the ground state. In this process, low-energy electrons populate low vibrational levels of CO₂, and collisions between vibrationally excited molecules gradually populate higher vibrational states, ultimately leading to dissociation[8].

This mechanism relies on vibration-to-vibration (VV) energy transfer, which promotes the population of higher vibrational levels due to the anharmonicity of the potential well [15], because the spacing between adjacent vibrational levels decreases as the vibrational number increases. Consequently, intermolecular collisions preferentially enhance the highest vibrational levels while depopulating the lowest ones. In particular, this effect is limited to the asymmetric stretching mode of CO₂ and does not apply to the symmetric stretching or bending modes, because the latter are coupled and can exchange energy mainly through intramolecular interactions[16].

The competing process, vibration-to-translation (VT) energy transfer, involves the loss of vibrational energy to translational (kinetic) energy. VT collisions depopulate high vibrational states and are strongly temperature-dependent, increasing with rising gas temperature. This creates a positive feedback loop, as VT processes further heat the gas, reducing overall efficiency [15]–[17].

The efficiency of different dissociation pathways is strongly influenced by the electron kinetic energy which depends, in turn, on the plasma discharge conditions. By adjusting the discharge parameters, specific reaction channels can be preferentially activated. Figure 1.7 presents the electron energy distribution among various processes as a function of the reduced electric field E/n , where n is the neutral gas density, and E is the electric field strength [18].

In nanosecond pulsed discharges of CO₂ at atmospheric pressure, the reduced electric field typically exceeds 200 Td [19]. Under these conditions, electronic excitation and ionization dominate the energy distribution. The energy fraction allocated to different modes, particularly vibrational excitation, plays a fundamental role in CO₂ dissociation efficiency. As previously mentioned, vibrationally excited CO₂ molecules can significantly enhance dissociation, making the energy partitioning within the discharge a key factor in

optimizing conversion processes.

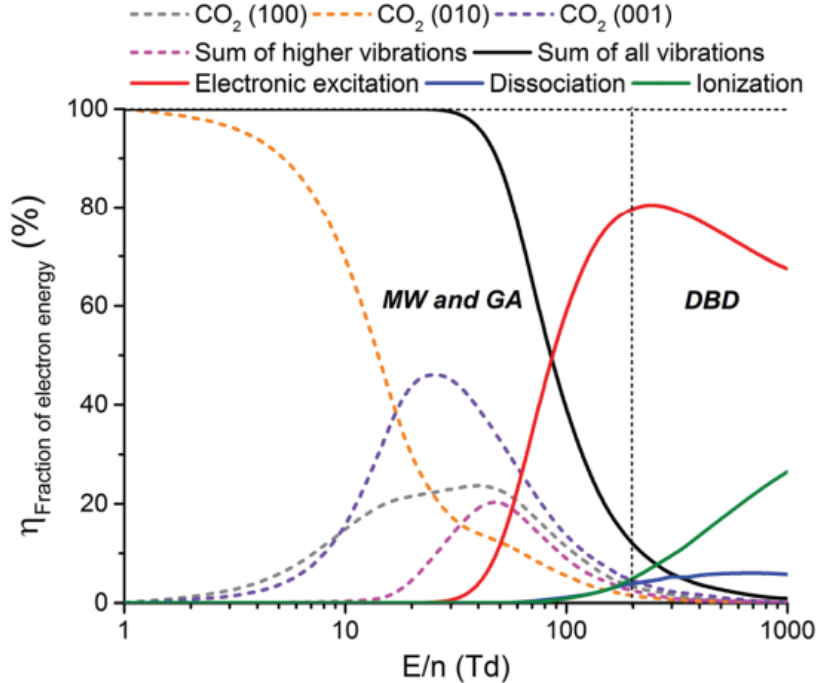


Figure 1.7: The transfer of electron energy to different excitation channels, ionisation, and dissociation of CO_2 is presented as a function of the reduced electric field (E/n). Figure reported from [8]

Various discharge configurations have been investigated for CO_2 valorization. These configurations differ in power supply type, reactor design, and operating pressure. Three main types of non-thermal plasmas are commonly employed: dielectric barrier discharges (DBDs)[20], [21], microwave (MW) discharges[22], [23], and gliding arc (GA) discharges[24], [25]. Other configurations, such as radiofrequency (RF)[26], corona[27], and glow discharges[28], are also widely studied.

Among these, nanosecond repetitively pulsed (NRP) discharges stand out as a promising technology particularly effective for generating non-equilibrium plasmas and driving efficient chemical transformations.

1.7 Nanosecond repetitively pulsed discharges

Nanopulsed repetitively discharges offer a promising method for CO_2 valorization, operating efficiently at atmospheric pressure without requiring low-pressure control systems. Although high-pressure environments typically limit non-equilibrium conditions due to frequent collisions that enhance relaxation and quenching, the rapid voltage variation in NRP discharges—characterized by several-kV amplitudes, nanosecond rise times, and

a full width at half maximum (FWHM) of approximately 10 ns—facilitates high non-equilibrium conditions.

The interpulse time (T_p)(see Figure 3.11) significantly influences NRP discharge behavior. As pulse repetition frequency increases, a memory effect arises from residual ions, free electrons, and other long-lived species in the discharge gap, affecting subsequent pulses. Higher repetition frequencies lead to increased species accumulation, lowering the breakdown voltage compared to single or low-frequency pulses[29], [30]. Gas heating and expansion from previous pulses can further facilitate breakdown, reducing impedance and enhancing plasma conductivity[31].

Experimental studies have demonstrated that reducing T_p to approximately 10 μs results in notable changes in the electric current/voltage (I/V) and in the spatial propagation of the discharge[32], [33]. While larger T_p values allow for spatially independent pulses, shorter T_p values cause pulses to become increasingly correlated, eventually following the same channels. This reduction in T_p also lowers breakdown voltage, increases current, and enhances CO_2 dissociation through vibrationally excited mechanisms, improving conversion efficiency [32].

Time-resolved optical diagnostics, such as optical emission spectroscopy (OES), have provided deeper insights into plasma dynamics. Ceppelli et al. [1] classified pulses into two types: Type I (with longer T_p , where each pulse is independent) and Type II (with short T_p , showing a strong memory effect). Type I pulses exhibit two phases: an early breakdown phase dominated by electron impact processes, followed by a spark regime characterized by high ionization and lower electron energy. In contrast, Type II pulses transition abruptly to the spark regime. Spectroscopic analysis reveals that CO_2 dissociation predominantly occurs in the later stages of the spark regime, even after the discharge current subsides, indicating a long-lasting dissociation mechanism. Montesano et al. [34] confirmed this, observing a delay between discharge breakdown and CO_2 dissociation, and showed that shorter T_p enhances process efficiency by achieving similar conversions with less energy input.

However, in the experiments conducted by Ceppelli et al. [1], the presence of an electrode gap in the transmission line led to an impedance unmatch. As a result, the current-voltage (IV) characteristics, and consequently the emission profile, exhibited reflections. These reflections could influence the observed temporal evolution of the generated species, potentially affecting the interpretation of the discharge dynamics.

1.8 This thesis

In this thesis, time-resolved emission spectroscopy is utilized to examine the dissociation dynamics of a CO₂ nanosecond repetitively pulsed plasma discharge, aiming to analyze the temporal evolution of the resulting species. The investigation is conducted in both burst mode(Type II), with an interpulse interval of 18 μ s, and continuous mode(Type I), at a frequency of 200 Hz, and also trying to match the impedance of the line.

Chapter 2 provides an overview of the fundamental principles of spectroscopy.

Chapter 3 describes the experimental setup, detailing the electric, gas handling, and optical components of the system.

Chapter 4 is dedicated to data analysis, including the estimation of time delays between the current and voltage, as well as the parasitic capacitance. It also examines the temporal jitter between the discharge signal and the spectrum acquisition system. Additionally, the process of impedance matching is discussed.

The results section presents TR-OES data for various configurations: the line unmatched in impedance in continuous mode at the center of the electrode gap (5.5 mm) and at the cathode (5.5 mm), line-matched in impedance in burst mode with an electrode gap of 2.4 mm for both the first and second pulses, and the line unmatched in impedance in burst mode for the second pulse with an electrode gap of 2.4 mm.

Finally, Chapter 6 discusses the conclusions derived from this study and outlines potential future research directions.

Chapter 2

Spectroscopy

2.1 Plasma diagnostic techniques

Spectroscopy is a fundamental diagnostic technique for analyzing the radiation emitted by atoms, molecules, and their ions. This method provides critical insights into plasma processes and parameters, enabling real-time observations of dynamic phenomena. Since spectroscopy is a non-invasive technique, it does not interfere with the plasma itself, making it widely applicable in plasma diagnostics.

Generally, plasma spectroscopy is divided into two classes of measurements: the passive method (e.g., optical emission spectroscopy) and the active method (e.g., absorption spectroscopy).

2.1.1 Optical emission spectroscopy

In optical emission spectroscopy, the light emitted by the plasma is recorded. Of particular relevance to this thesis is the investigation of particle excitation mechanisms, specifically the excitation of atoms, molecules, and ions due to electron impact. This process results in a transition from an initial energy level q to a higher energy level p ; this is followed by a spontaneous decay to level k with a transition probability A_{pk} , leading to line emission ε_{pk} . The recorded radiation can obtain the densities of excited species present in the plasma. However, the use of a model is required, and the making of assumptions regarding the distribution of energy levels that constitute the densities characterizing the non-equilibrium state. [35].

When excitation predominantly occurs from the ground state, as in the Corona equilibrium scenario, the measured intensity is approximately proportional to the ground-state

density. However, additional plasma processes, such as electron-induced de-excitation, can also influence this relationship.

Generally, a body at temperature T emits radiation following Planck's radiation law, which describes the radiation density per unit frequency, $\rho(\nu, T)$, as [35]:

$$\rho_\nu(\nu, T)d\nu = \frac{8\pi h\nu^3 d\nu}{c^3(\exp\left(\frac{h\nu}{k_B T}\right) - 1)} \quad (2.1)$$

where k_B is Boltzmann's constant, c is the speed of light, ν is the radiation frequency, h is Planck's constant, and T is the equilibrium temperature.. A plasma in thermodynamic equilibrium (TE) exhibits black-body emitter characteristics. With Planck's law, one could derive the equilibrium temperature and, with that, use the Boltzmann distribution to determine excited-state densities, the Saha equation for ion and electron densities in the case of charge neutrality, and the Maxwellian distribution for energy distributions of particles. As an example for the Boltzmann distribution the ratio between the populations n_p and n_q of energy states E_p and E_q is, as derived by [35]:

$$\frac{n_p}{n_q} = \frac{g_p}{g_q} \exp\left(-\frac{E_p - E_q}{k_B T}\right) \quad (2.2)$$

where g_p and g_q are statistical weights. For high electron density plasmas, there is equilibrium between excited states and the continuum, and the Saha equation quantifies the population of a given excited state p [35]:

$$\frac{n_p}{g_p} = \frac{n_e n_i}{g_e g_i} \left(\frac{2\pi m_e k_B T}{h^2} \right)^{3/2} \exp\left(-\frac{E_{\text{ion}}}{k_B T}\right) \quad (2.3)$$

Where g_e , n_e , g_i , and n_i are the statistical weights and densities of the electron and ion, respectively, and E_{ion} is the ionization energy of state p . The case is different for nonthermal plasmas: they are not in thermodynamic equilibrium (TE) and require continuous energy input to maintain their state. Such plasmas display temperature and density gradients, and local equilibrium (LTE) may only approximate Maxwellian, Boltzmann, and Saha distributions at high electron densities. Moreover, this kind of plasma, under these conditions, emits light, so Planck's law cannot be used to describe the intensity and spectral distribution [35].

2.1.2 Absorption spectroscopy

In absorption spectroscopy, excitation from a lower energy level q to a higher level p occurs via a radiation field. This process is characterized by the absorption probability B_{qp} , leading to a reduction in the intensity of the radiation field, which is then measured [35]. In these techniques, an external light source probes the plasma, where the radiation is either absorbed, leading to excitation, or scattered by particles. Laser-induced fluorescence (LIF) spectroscopy utilizes absorbed light to extract plasma parameters from the emitted spectral distribution or intensity variations with laser wavelength. Meanwhile, scattering techniques, including Thomson, Rayleigh, and Raman scattering, provide additional plasma diagnostics [35].

2.2 Spectral Line Characteristics

Line radiation occurs from transitions between two bound states within atoms or molecules. In atomic plasmas, this radiation spectrum consists of distinct lines at specific frequencies, resulting from transitions between various electronic states. Molecular spectra also exhibit such transitions; however, due to the additional vibrational and rotational states unique to molecules, their energy levels are much denser. Consequently, molecular emissions appear as bands, representing clusters of ro-vibronic (rotational-vibrational-electronic) transitions, especially visible in the optical spectrum [35].

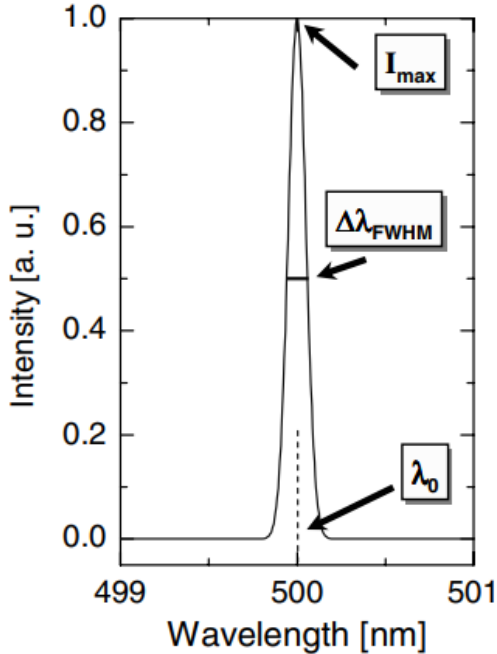


Figure 2.1: characheristics of line radiation. Figure reported from [36].

A spectrum is typically represented by two axes: wavelength and intensity (Figure 2.1). The central wavelength of an emission line, λ_0 , is determined by the photon energy

$$E = E_p - E_k,$$

which corresponds to the energy difference between an upper level p with energy E_p and a lower level k with energy E_k . Using Planck's constant h and the speed of light c , this relationship is expressed as

$$\lambda_0 = \frac{hc}{E_p - E_k} . \quad (1)$$

Since the transition energy is unique to each particle species, the central wavelength serves as an identifier for the radiating species.

The absolute intensity of an emission line, is proportional to:

$$I_{pk} \propto n(p)A_{pk} . \quad (2)$$

This expression indicates that the line intensity is proportional to both the Einstein coefficient for spontaneous emission, A_{pk} , which quantifies the probability of photon emission by an atom or molecule, and the population density of the excited state, $n(p)$.

2.2.1 Broadening mechanisms

Spectral lines are not infinitely narrow. An excited state with a finite lifetime that relaxes radiatively emits a line that has a finite width corresponding to the Heisenberg uncertainty principle. The natural lifetime τ of state p is given by:

$$\tau = \frac{1}{\sum_{q < p} A_{pq}}.$$

Through the Heisenberg uncertainty principle, this lifetime relates to the natural line width $\Delta\nu_{\text{nat}}$:

$$\Delta\nu_{\text{nat}} = \frac{1}{2\pi\tau}.$$

The resulting line profile $f(\nu)$, which describes the spectral intensity distribution, follows a Lorentzian shape:

$$f(\nu - \nu_0) \propto \frac{\Delta\nu_{\text{nat}}}{(\nu - \nu_0)^2 + (\Delta\nu_{\text{nat}}/2)^2},$$

where ν_0 is the center frequency and $\Delta\nu_{\text{nat}}$ the full width at half maximum (FWHM) [36].

Several broadening mechanisms affect the natural line profile, altering both its width and shape. Collisions between emitter and collider can increase the line width, this phenomenon is known as collisional or pressure broadening. Thermal motion of emitting species leads to Doppler broadening. Stark broadening arises from interactions with charged particles in the plasma. In contrast, Zeeman broadening, which occurs in the presence of a magnetic field, is negligible in non-magnetized plasmas like the one studied. Additionally, instrumental broadening, caused by the finite resolution of the spectrometer, further contributes to the observed line shape [36].

2.2.2 Bremsstrahlung and recombination radiation

In optical spectroscopy, there are other phenomena that can influence the representation of the emission spectra. Particularly, in plasma radiation, two primary types are identified: free-free emission (Bremsstrahlung) and free-bound emission (recombination radiation). Bremsstrahlung radiation results from Coulomb collisions, where charged particles, primarily electrons in low-temperature plasmas, accelerate upon interacting with ions, thus emitting radiation. This process, termed "free-free" radiation, involves tran-

sitions of the electron between two unbound states. Ion-neutral scattering is negligible because of the ion's larger mass. Electron-atom interactions contribute minimally, except in low-ionization plasmas (below 10^{-3}). Bremsstrahlung exhibits a continuous wavelength spectrum, peaking around 100 nm for 10 eV electrons [35].

Recombination radiation, or free-bound emission, occurs when an electron combines with an ion to form either the ground or an excited state of the atom, or transitions from a Z^+ to a $(Z-1)^+$ ion state. This recombination produces a continuous emission spectrum. Radiative recombination is more probable for lower quantum states, producing high-energy photons most frequently. Due to the need for both energy and momentum conservation, the cross-section for radiative recombination remains small [35].

2.3 Energy levels nomenclature

2.3.1 Atoms

Electrons in atoms are characterized by their orbital type, defined by the principal quantum number n and the orbital angular momentum quantum number l . The letters corresponding to l values are given in the following table:

$l = 0$	$l = 1$	$l = 2$	$l = 3$	$l = 4$...
s	p	d	f	g	...

Electron configurations are written as $3s^2$, $2p^4$, etc., where the superscript denotes the number of electrons in each orbital. Pauli's exclusion principle limits the number of electrons in each orbital to $2(2l + 1)$. The ground state configuration of an atom is the lowest energy arrangement of electrons in the orbitals.

For example, the ground state electron configuration of carbon is $1s^2 2s^2 2p^2$.

The spectroscopic term symbol describes the atom's angular momentum states, defined by:

$$2S+1 L_J$$

where L is the total orbital angular momentum quantum number, S is the total spin quantum number, and J is the total angular momentum quantum number. For a given L and S , J can take values from $|L - S|$ to $L + S$ in integer steps.

The multiplicity is $2S + 1$ for $S < L$ and $2L + 1$ for $L < S$, representing the number of distinct J values.

The degeneracy of a level with given J is $g_J = 2J + 1$, and for a multiplet with N components:

$$g_{\text{mult}} = \sum_{i=1}^N g_{J_i}.$$

This is the total degeneracy for a group of states differing only in energy due to spin-orbit coupling [37].

2.3.2 Molecules

- \hat{L} is the electronic angular momentum operator. For the commutation relation $[\hat{L}^2, \hat{H}] = 0$ to be valid spherical symmetry is necessary. Hence in diatomic molecules, L isn't a valid choice for a quantum number. \hat{L} precesses about the internuclear axis, and it originates a projection with components $\hat{\Lambda}$ that have values:

$$\Lambda = 0, 1, 2, \dots, L$$

$\Lambda = 0, 1, 2, 3, \dots$ states are referred to as $\Sigma, \Pi, \Delta, \Phi, \dots$

- \hat{S} , quantum number S , is the electronic spin angular momentum operator. In the cases where the angular momentum has a non-null value ($\Lambda \neq \Sigma$), the motion of the electron orbital makes \hat{S} be coupled with the internal magnetic field. The precession of \hat{S} around the internuclear axis originates a projection along the axis, with components $\hat{\Sigma}$, which is in the range:

$$\Sigma = -S, -S + 1, \dots, S - 1, S$$

- \hat{J} is the total electronic angular momentum operator, given by the sum of \hat{L} and \hat{S} . As $\hat{\Lambda}$ and $\hat{\Sigma}$ are parallel to the internuclear axis, $\hat{\Omega}$, the axial component of \hat{J} , is given by them:

$$\Omega = |\Lambda + \Sigma|$$

- $\hat{N} = \hat{J} - \hat{S}$ is the spinless total angular momentum operator.
- \hat{R} is the nuclei's rotational angular momentum operator.

- $\hat{\sigma}$ is the reflection operator against any plane parallel to the internuclear axis, which for diatomic molecules is always a symmetry plane. Non-degenerate states (Σ states) have electronic wavefunctions that either remain unchanged or are inverted when reflected. In the first noninverting case, the state is denoted as Σ^+ , otherwise as Σ^- .
- \hat{I} is the inversion operator through the symmetry center of the molecule. For molecules with an inversion center, the electronic wave function can again remain unchanged or be inverted upon reflection. If unchanged, it is defined as even (gerade, g), whereas if inverted it is defined as odd (ungerade, u).
- The term symbol defines the state of a diatomic molecule:

$$2S+1\Lambda^{(\pm)}\Omega(g/u)$$

An additional letter (X, A, B, C, etc.) preceding the state indicates the ground state, first excited state, second excited state, and so on [11].

Due to additional degrees of freedom, each electronic state contains vibrational levels characterized by the quantum number v , and each vibrational level has associated rotational levels characterized by the quantum number J .

An example of the energy level diagram for the CO molecule is shown in the figure 2.2.

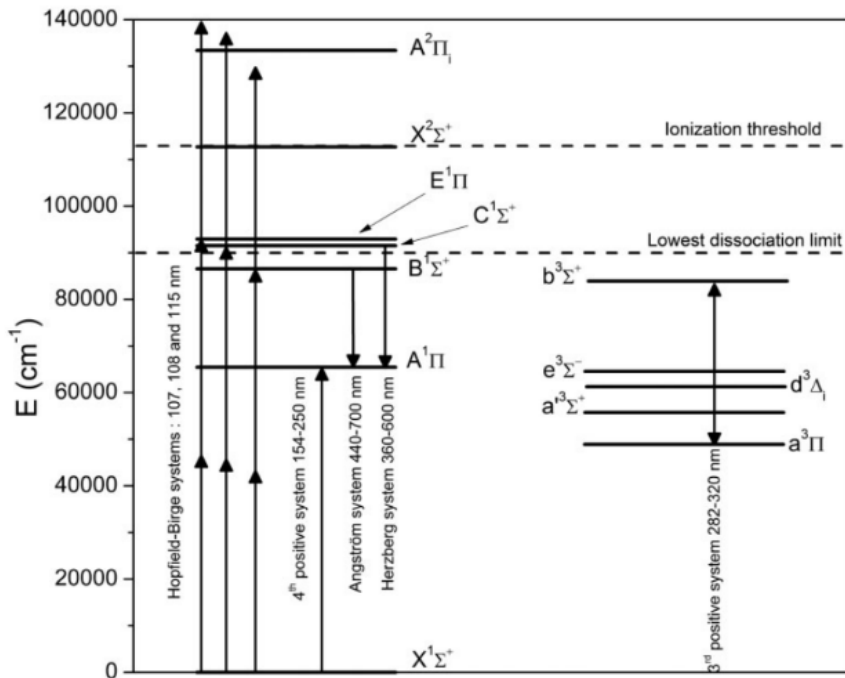


Figure 2.2: Energy level diagram of the CO molecule [38].

2.4 Spectroscopic Instrumentation

When performing Optical Emission Spectroscopy (OES), the first step is to collect the light emitted by the plasma and direct it towards an instrument capable of dispersing the light. The selection of spectrographs, detectors, and optical systems depends heavily on the specific diagnostic application, especially when high temporal resolution is required for studying transient discharges over time. A spectrometer generally consists of several fundamental components: entrance and exit slits, a dispersive element (such as a grating), and imaging mirrors. As shown in Figure 2.3 for the Czerny–Turner configuration, these components enable the separation of light into its constituent wavelengths. The light is dispersed by the grating and directed toward the exit slit, where a suitable detector then detects it [36].

To ensure that the spectrometer captures the emitted light effectively, optical systems may be used to image the plasma light source onto the entrance slit, or optical fibers can be employed. Additionally, in the case of studying transient phenomena, temporal resolution is crucial, necessitating detectors with high temporal sensitivity to resolve the rapid variations in emission over time [36].

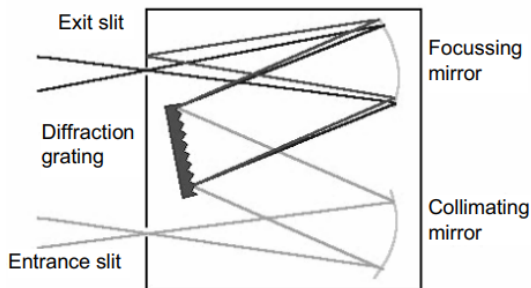


Figure 2.3: Monochromator in Czerny–Turner configuration. Figure reported from [36].

The various components of the spectroscopic system are responsible for determining key factors, including the light throughput, the spectral resolution, and the accessible wavelength range. The selection of grating, defined by the number of grooves per millimeter (lines/mm), has a substantial impact on the spectral resolution. A determining factor in the wavelength range with maximum reflection efficiency is the blaze angle of the grating, which in turn affects the sensitivity of the system. Furthermore, to achieve an improved spectral resolution, the spectrometer's focal length exerts an influence on spectral resolution, and in conjunction with the grating size, it defines the aperture and light throughput. Moreover, the intensity of the light is affected by the width of the entrance

slit; a wider slit increases the intensity but reduces the spectral resolution. A detector, at the exit, such as a photomultiplier, can be mounted behind the slit, or alternatively, at the image plane, a CCD (charge-coupled device) array can be placed directly. In the case of a photomultiplier, the exit slit width affects the spectral resolution, whereas in the case of a CCD array, the size of the pixels plays a similar role. Among the detectors that can influence the overall sensitivity, there are, for instance, photomultipliers with diverse cathode coatings or CCD arrays with varying sensor kinds, such as with intensification or back-illumination. Systems utilizing photomultipliers are typically scanning systems, whereas those employing CCD arrays can capture specific wavelength ranges. To achieve spatial resolution, one can use two-dimensional detectors, while temporal resolution is dependent on the detector in question. Photomultipliers offer rapid response times. In contrast, exposure and readout times constrain CCD arrays [36].

The ICCD (Intensified Charge-Coupled Device) consists of an image intensifier coupled to a CCD sensor. The image intensifier plays a crucial role in amplifying weak light signals, and the key component in this amplification process is the microchannel plate (MCP). Incoming photons are first converted into electrons by the photocathode. These electrons are then directed into the MCP, which significantly amplifies the electron signal. The MCP consists of thousands of tiny channels that multiply the electrons through a process known as electron cascade. This multiplication process greatly enhances the number of electrons, allowing for the detection of extremely faint light signals. The amplified electrons then strike a phosphorescent screen, producing an intensified light image that is captured by the CCD sensor and converted into an electronic signal. The MCP is, therefore, essential for increasing the signal strength and enabling high-sensitivity measurements, particularly in low-light conditions or when capturing transient phenomena with high temporal resolution [36].

Several typical system configurations can be used depending on the application. Small pocket-sized spectrometers are suitable for line monitoring (tracking the temporal behaviour of an emission line). While these systems have a poor spectral resolution ($\Delta\lambda \approx 1\text{--}2\text{ nm}$), they offer good time resolution and are effective for simple diagnostics such as monitoring plasma stability or particle density changes. A more advanced system might include a spectrometer with a grating with 1200 lines/mm and a focal length of 0.5–1 m ($\Delta\lambda \approx 40\text{ pm}$). In such systems, optics and optical components are significantly sharpened, and the detector influences the time resolution. A 2-dimensional CCD camera can

provide sufficient spatial resolution. This configuration represents a versatile setup, balancing spectral resolution with temporal performance [36].

2.5 Calibration

An essential aspect of spectroscopic systems is their calibration. By exploiting the plasma itself or spectral lamps in conjunction with wavelength tables, the wavelength axis calibration can be achieved. In my experiment, a Ne lamp is used, as their emission lines span a broad wavelength range and have lines with a known bandwidth [36]. An example of the Ne emission spectrum used to calibrate my spectrometer is shown in figure 2.4.

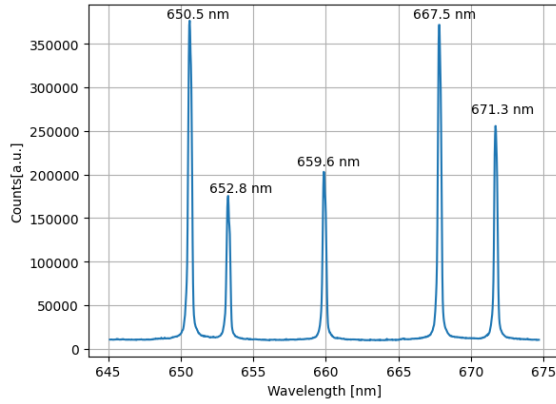


Figure 2.4: Example of Ne peaks used to calibrate the wavelength axis of 1200lines/mm grating of this experiment

Calibrating the intensity axis can be done either absolute or relative . A relative calibration only accounts for the spectral sensitivity of the system across the wavelength axis. In contrast, an absolute calibration also provides a conversion factor between the measured signals (counts or voltage) and physical units like $W/(m^2sr)$ or $Photons/(m^3s)$, as outlined in the corresponding equations.[36].

To calibrate the intensity, light sources with known spectral radiance are required. One critical aspect of this process is ensuring proper light source imaging onto the spectroscopic setup, while conserving the solid angle, often adjusted using apertures. Common calibration standards in the visible spectral range include tungsten ribbon lamps and halogen lamps. For extending into the ultraviolet range down to 200 nm, deuterium lamps are typically employed. These calibration sources must be highly accurate and are usually electrically stabilized, although they degrade over time, which affects their usability,

particularly for absolute calibration [36].

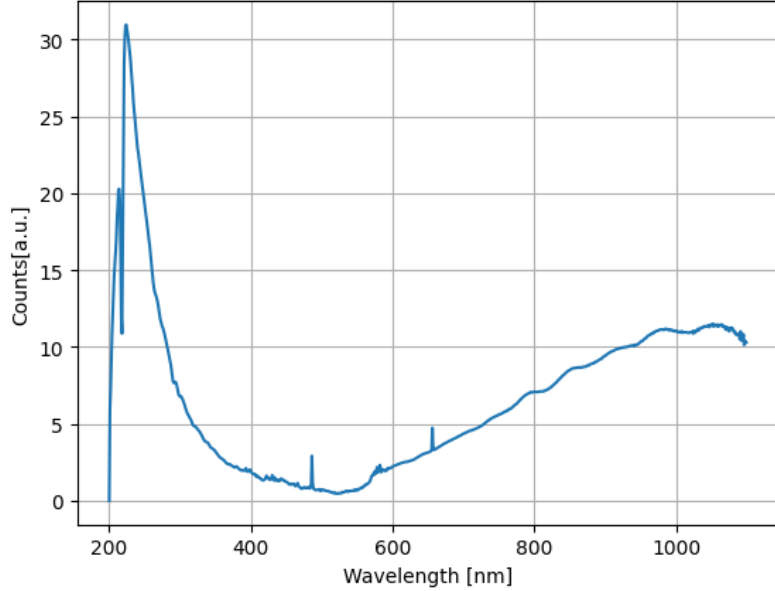


Figure 2.5: Calibration curve of the halogen-deuterium lamp used to calibrate the intensity axis of the spectra

In my experiment, a deuterium-halogen lamp was used to calibrate the y-axis. Figures 2.5 shows the employed calibration curve of the deuterium-halogen lamp AvaLight-DH-S, which operates in the 190 nm -2500 nm range with 90 W power consumption, a lamp lifetime of up to 2000 h, and an optical power output of 206 μ W in a 1000 μ m fiber [39]. To derive the conversion factor, which represents the spectral sensitivity of the system, the spectral radiance curve is divided by the recorded spectrum. [36].

Chapter 3

Experimental Setup

3.1 Setup

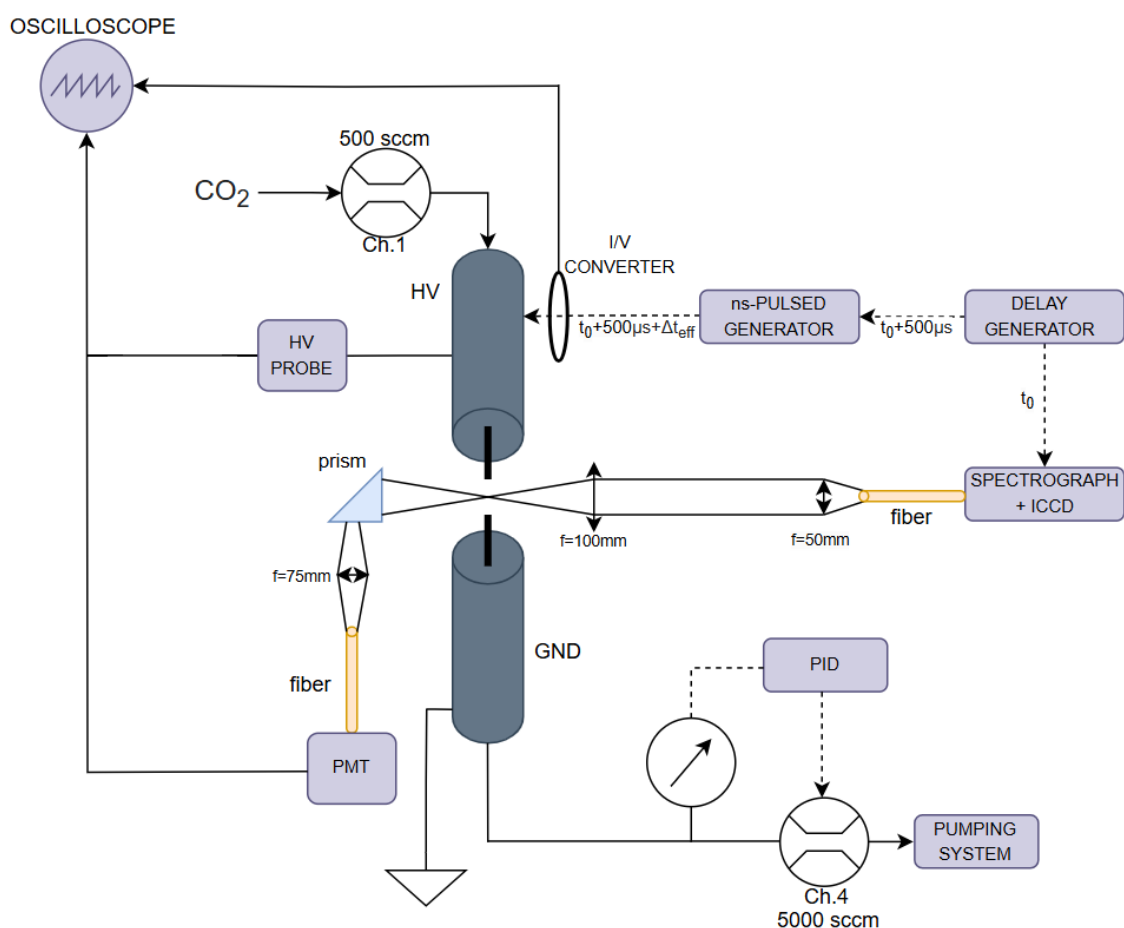


Figure 3.1: Schematic drawing of the experimental apparatus. ICCD: intensified CCD, PMT: photomultiplier, PID: proportional-integral-derivative

The experimental setup employed in this study is specifically designed to investigate the dissociation of CO₂ induced by the nanosecond pulsed electric discharge. The system is centered around a reactor comprising two thin tungsten electrodes arranged in a pin-to-pin configuration with a variable separation distance, which can be adjusted as needed. In this study, interelectrode gaps of 5.5 mm and 2.4 mm were used. These electrodes are housed within a quartz glass chamber. The high-voltage (HV) and ground electrodes are tungsten rods, while the gas inlet and outlet are integrated into the electrode supports. Each electrode has a diameter of approximately 1 mm. Quartz is selected for its optical transparency in the ultraviolet-visible range and its robust resistance to the thermal and electrical stresses generated during the discharge process. Tungsten is chosen for its high resistance to sputtering, ensuring durability under operating conditions.

The anode of the reactor is connected to a nanosecond pulse generator(NPG) (NPG18/100k, Megaimpulse Ltd) via a 3-meter cable, triggered by a digital delay generator. Between the end of the 3-meter cable and the reactor, a current probe and a voltage probe are positioned in sequence to measure the current-voltage (*I-V*) curves. BNC cables connect these probes to the oscilloscope(Teledyne LeCroy HD9104).

The experimental setup is structured into four primary components: electrical diagnostics, gas handling, optical diagnostics, and noise attenuation. The following sections provide a detailed explanation of each of these aspects. A drawing of the experimental setup is shown in 3.1, while pictures are shown in 3.2 and 3.17.



Figure 3.2: Picture of the experimental setup

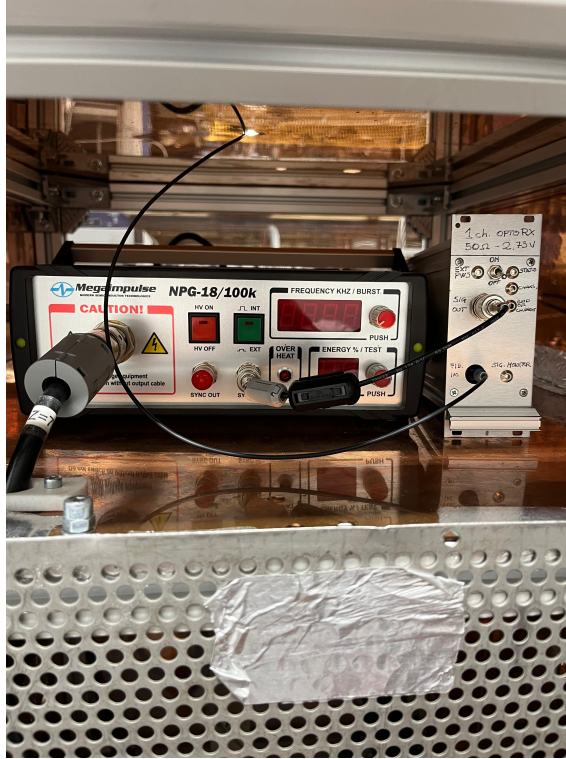


Figure 3.3: Picture of the generator and the OPTO-RX

3.2 Electrical diagnostics

In the experimental setup, the voltage and current signals exceed the direct measurement capabilities of the oscilloscope. To address this limitation, a voltage probe and a current probe are incorporated into the system. The acquired signals are subsequently adjusted to account for the attenuation factors specific to each probe, ensuring an accurate representation of the actual voltage and current values.

The voltage probe used is the Tektronix P6015 model, which has a capacitance of 3 pF and a resistance of $100\text{ M}\Omega$. When coupled with an oscilloscope having an input resistance of $1\text{ M}\Omega$, the probe attenuates the signal by a factor of 1000.

The current probe is a current transformer(CT-D 1.0, Magnelab), designed to convert current into a voltage signal with a conversion factor $k = 1\text{ V/A}$. It has a nominal resistance of $R_{\text{PROB}} = 50\text{ }\Omega$. To reduce the signal amplitude, a -20 dB attenuator is used, which decreases the voltage signal by a factor of $1/10$ when coupled with $R_{\text{osc}} = 1\text{ M}\Omega$.

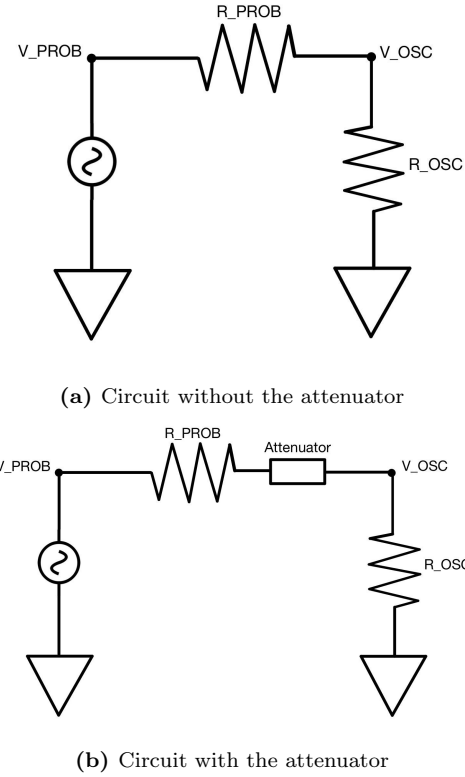


Figure 3.4: Configurations of the circuit with and without the attenuator.

The current probe transforms the current signal into a voltage signal according to the gain $k = 1 \text{ V/A}$, yielding $V_{\text{PROB}} = I_{\text{PROB}}k$. The voltage measured by the oscilloscope without the attenuator is given by:

$$V_{\text{OSC}} = \frac{R_{\text{OSC}}}{R_{\text{OSC}} + R_{\text{PROB}}} V_{\text{PROB}} \quad (3.1)$$

For $R_{\text{OSC}} = 1 \text{ M}\Omega$, it follows that $V_{\text{OSC}} = V_{\text{PROB}}$, resulting in a gain of:

$$g_{\text{noatt}} = \frac{V_{\text{OSC}}}{V_{\text{PROB}}} = 1.$$

When the attenuator is included, the oscilloscope voltage becomes $V_{\text{OSC}} = V_{\text{PROB}} \frac{1}{10}$, resulting in a gain of:

$$g_{\text{att}} = \frac{V_{\text{OSC}}}{V_{\text{PROB}}} = \frac{1}{10}.$$

For $R_{\text{OSC}} = 50 \Omega$, the oscilloscope voltage without the attenuator is $V_{\text{OSC}} = V_{\text{PROB}} \frac{1}{2}$, leading to:

$$g_{\text{noatt}} = \frac{V_{\text{OSC}}}{V_{\text{PROB}}} = \frac{1}{2}.$$

When the attenuator is included, the oscilloscope voltage becomes $V_{\text{OSC}} = \frac{1}{2}V_{\text{PROB}}\frac{1}{10}$, resulting in:

$$g_{\text{att}} = \frac{V_{\text{OSC}}}{V_{\text{PROB}}} = \frac{1}{20}.$$

All the system is encapsulated in a Faraday cage to isolate electrically the system and the environment.

A picture of the voltage and current probes is shown in 3.5.

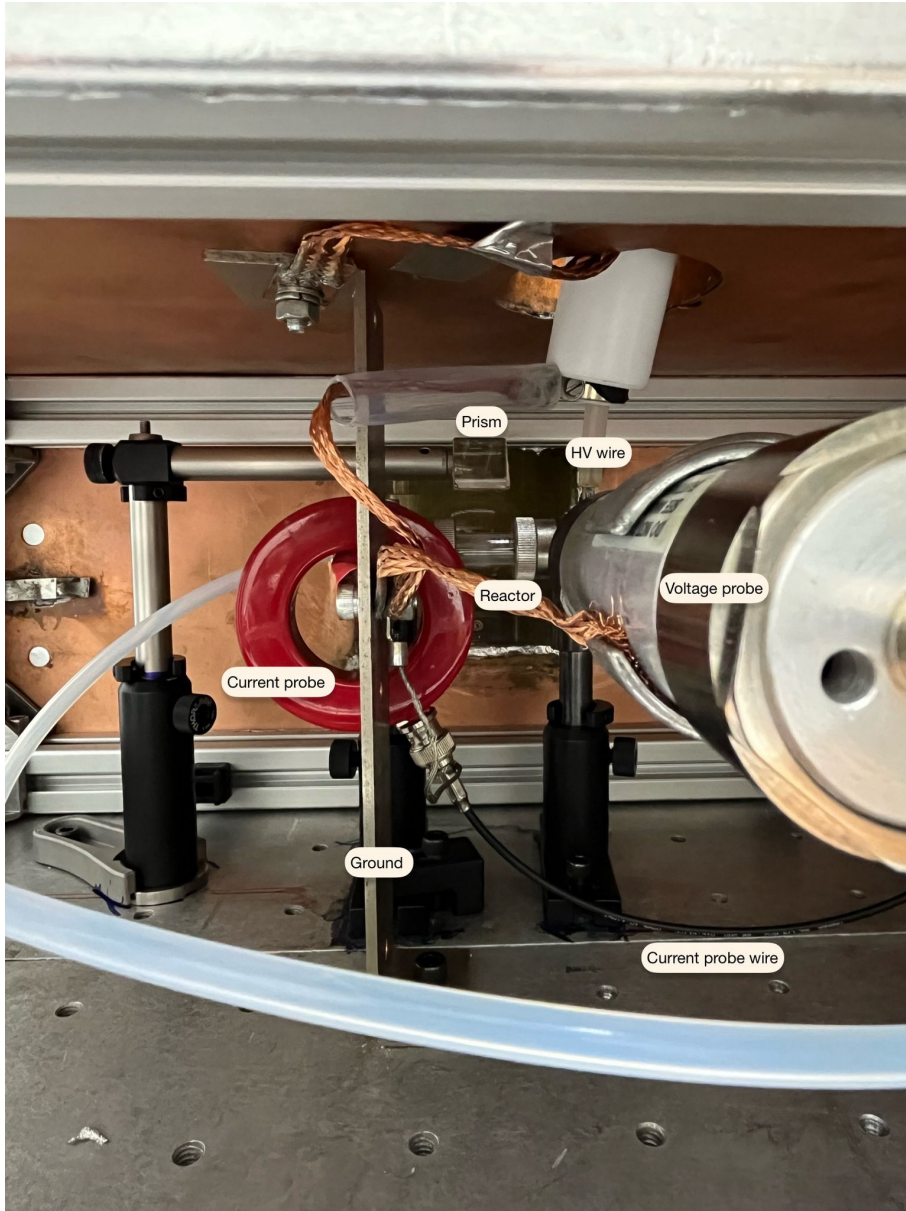


Figure 3.5: Picture of the current and voltage probes

3.2.1 Electrical noise

Electrical noise and electromagnetic interference (EMI) can significantly affect the accuracy of measurements in high-voltage pulsed discharge systems. The main noise source in this setup is the discharge itself, which generates strong electromagnetic fields that can interfere with measurements. To minimize these effects, several shielding and grounding strategies are implemented. One of the key measures is the encapsulation of the entire system within a Faraday cage. This enclosure effectively attenuates the measurement setup from the electromagnetic interference produced by the discharge, reducing unwanted noise.

and ensuring more reliable signal acquisition.

Additionally, the oscilloscope was placed as far away as possible from the discharge region (compatible with the wire lengths). This helps reduce direct interference with the measurement electronics, further improving the signal quality. Proper grounding and careful cable management also contribute to minimizing noise, enhancing the overall stability of the measurements.

The wires and the phototube are also encapsulated in a Faraday cage made of aluminum foil to further reduce electromagnetic interference, as shown in figure 3.2. This additional shielding ensures that any electromagnetic noise generated by the discharge does not affect the performance or measurements of the system.

3.3 Gas handling

The gas is injected between the electrodes, where the electric discharge is ignited. The reactor is connected to the gas feed system according to the following scheme:

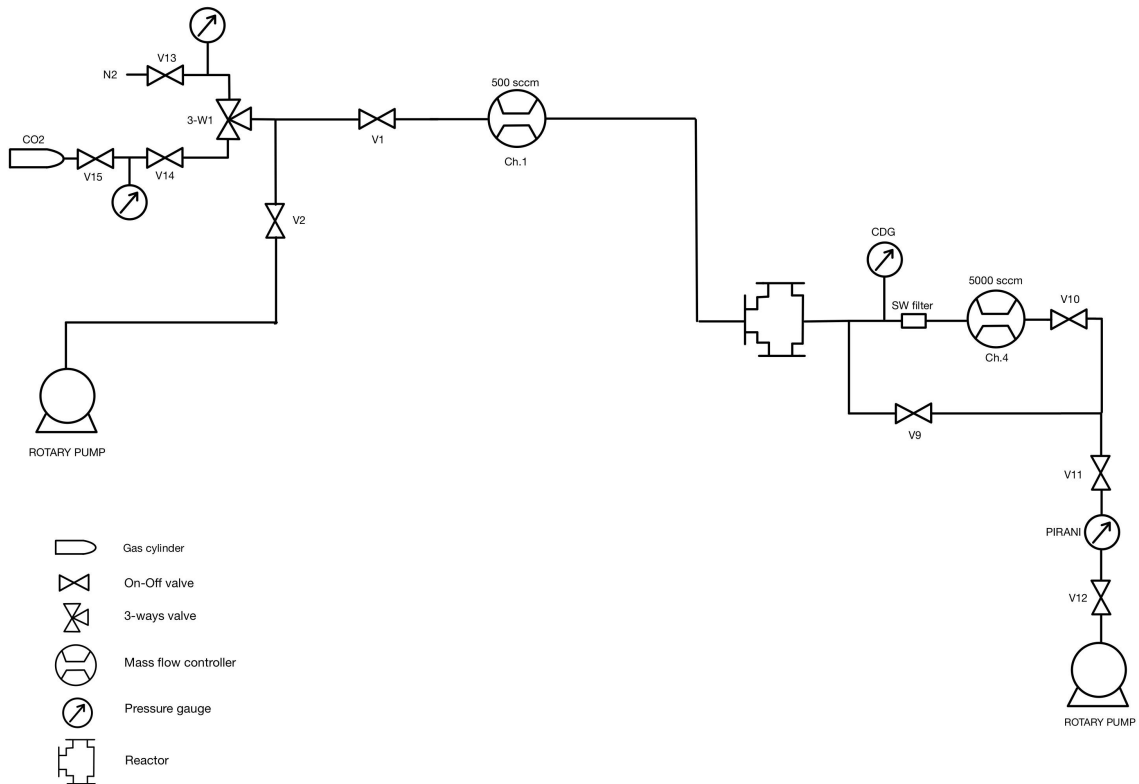


Figure 3.6: Gas feed system

The gas handling system incorporates a three-way valve (3-W1), which can be adjusted to supply either CO₂ or N₂. The N₂, sourced from the laboratory gas line, was used to measure the delay between current and voltage caused by the parasitic capacitance and inductance of the probes and wires. An advantage of using N₂ is that it does not contaminate the reactor, as it does not sputter carbon. The CO₂, supplied from a gas cylinder, serves as the primary working gas for the discharge process.

The output of 3-W1 is connected to both a bypass valve (V2), which vents directly to the rotary pump, and a valve (V1). Downstream of V1, the gas flow passes through a mass flow controller with a maximum capacity of 500 sccm, followed by the reactor. The reactor is connected to multiple components, including another bypass (V9) that leads to V11, a pressure gauge, and an SW filter. The SW filter is designed to remove solid particles emitted from the reactor before the gas passes through a second mass flow controller with a maximum capacity of 5000 sccm. Following the second mass flow controller, the gas flow continues through a valve (V10), which is also connected to V11. Downstream of V11, there is an additional pressure gauge, another valve (V12), and finally the rotary pump. The discharge is run at atmospheric pressure (975 mbar). A variable flow of CO₂ is introduced into the reactor via an MKS mass flow controller (Ch.1). Pressure stabilization at 975 mbar is achieved through a proportional-integral-derivative (PID) controller, which regulates a second mass flow controller located at the reactor's outlet (Ch.4).

The pressure within the system is monitored using a capacitive gauge (Varian Ceramcel, FS 1000 Torr), which provides input to the PID controller. The capacitive gauge was calibrated with a Torricelli barometer. Gas evacuation and circulation are facilitated by an Edwards two-stage rotary vane pump with a capacity of 80 m³ h⁻¹.

An inlet flux of 300 sccm was selected to achieve a residence time given by

$$t_{\text{res}} = \frac{V}{\text{flux}} = 0.08 \text{ s},$$

where the volume V is expressed as $V = A_{\text{react}} \cdot d_{\text{el}} = 0.39 \text{ cm}^3$. Here, $A_{\text{react}} = \pi r_{\text{react}}^2$ represents the cross-sectional area of the quartz reactor, with a reactor radius of $r_{\text{react}} = 0.50 \text{ cm}$. The electrode separation is $d_{\text{el}} = 0.55 \text{ cm}$.

Considering a discharge frequency of $f_{\text{disch}} = 200 \text{ Hz}$, the number of discharge impulses during each residence time is calculated as

$$n_{\text{imp}} = t_{\text{res}} \cdot f_{\text{disch}} = 16.$$

3.4 Optical diagnostics

3.4.1 Lenses

The optical emission from the plasma is collected using an optical system comprising two lenses and an optical fiber. The configuration of lens distances and types was chosen to achieve a magnification of the discharge, approximately $G \approx -0.5$. The thin lens equation is used to determine the distances:

$$\frac{1}{f} = \frac{1}{q} + \frac{1}{p} \quad (3.2)$$

where f is the focal length of the lens, p is the distance between the object and the lens, and q is the distance between the lens and the image.

The first lens(2 inches) has a focal length of $f_1 = 100$ mm, while the second lens(1 inch) has a focal length of $f_2 = 50$ mm. For the first lens, with $p_1 = 120$ mm and $f_1 = 100$ mm, the image distance q_1 is calculated as:

$$q_1 = \frac{f_1 p_1}{p_1 - f_1} = 600 \text{ mm},$$

resulting in a magnification of:

$$g_1 = -\frac{q_1}{p_1} = -5.$$

The second lens is positioned at $d_{12} = 150$ mm from the first lens, meaning the object distance for the second lens is $p_2 = d_{12} - q_1 = -450$ mm. The image distance q_2 for the second lens is then given by:

$$q_2 = \frac{f_2 p_2}{p_2 - f_2} = 45 \text{ mm},$$

where the optical fiber is placed. The magnification of the second lens is:

$$g_2 = -\frac{q_2}{p_2} = 0.1.$$

Thus, the total magnification of the optical system is:

$$g_{\text{tot}} = g_1 g_2 = -0.5.$$

This configuration allows us to have the same magnification ($g_{\text{tot}} = -0.5$) independently from the distance $p_1 > f_1$. To attenuate the intensity of the light signal, two neutral density filters (NDUV10B, Thorlabs) of optical density 1 are optionally placed between the last lens (1 inch diameter) and the optical fiber, and two long-pass filters (Thorlabs FEL 0400, FEL 0500) are placed between the last lens and the fiber to suppress the higher orders of the diffraction grating.

The light emitted by the discharge is collected to evaluate the time-resolved emission profile, utilizing a photomultiplier tube (PMT) (Hamamatsu H10721-210). To achieve this, a prism is positioned above the reactor to direct the emitted light, which is subsequently focused by a lens onto an optical fiber (as shown in Figure 3.8). This fiber transmits the signal to the PMT for detection. The resulting signal is then analyzed using an oscilloscope. A lens with a focal length of 75 mm (1-inch diameter), positioned at a distance of 225 mm from the reactor and 111 mm from the optical fiber, achieves a magnification of -0.5. This magnification is consistent with the value used in the previous setup and ensures compatibility with the diameter of the optical fiber.

A picture of the optical setup is shown in 3.7.

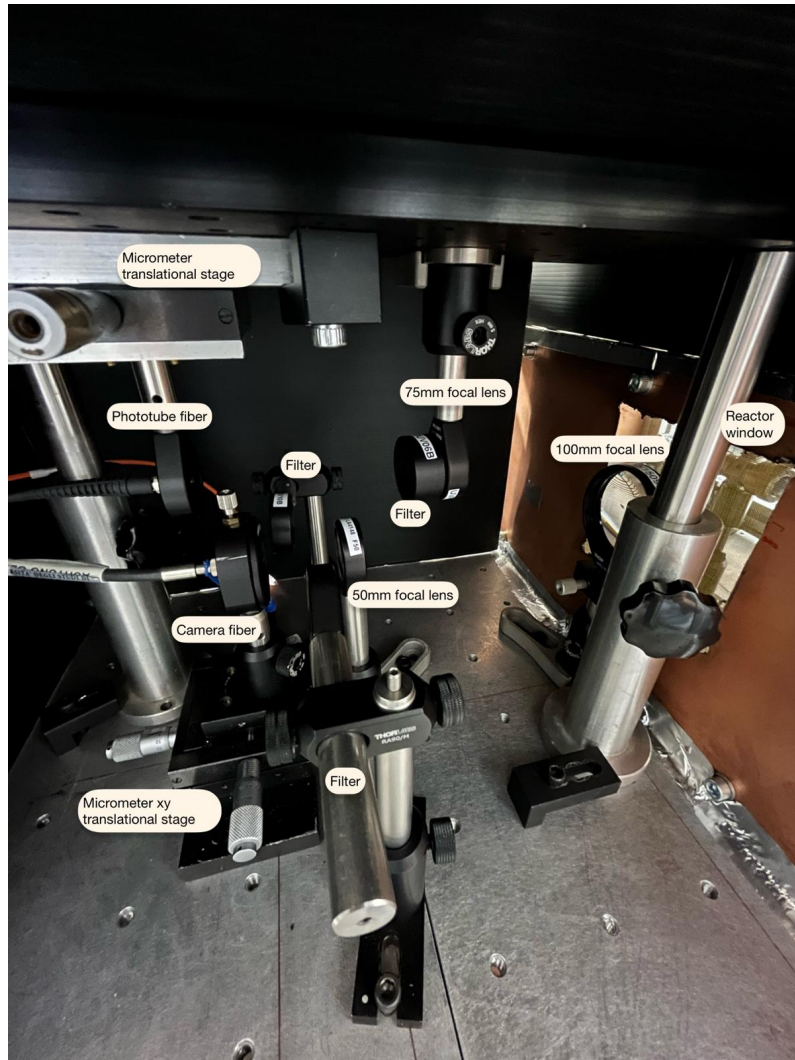


Figure 3.7: Picture of the optical system

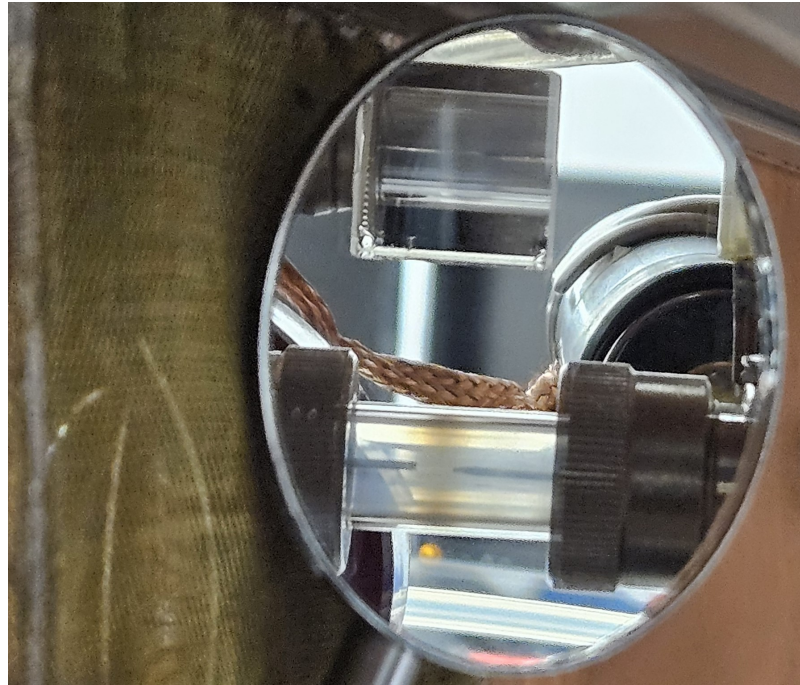


Figure 3.8: Zoom of the prism and the reactor

3.4.2 Spectrograph

The collected light is analyzed using a spectrograph consisting of a monochromator with a focal length of 300 nm (Shamrock SR303i-b) and an intensified, gateable CCD (ICCD) camera (Andor iStar DH334T-18U-03, 1024×1024 pixels). The light emitted from the source under investigation is first collected and focused into an optical fiber (LLB531 fiber bundle - round to rectangular, numerical aperture (NA) = 0.22), which subsequently directs it to an f-number matching device (Andor SR-ASM-0038) prior to its introduction into the entrance slit of the monochromator as we can see from the figure 3.9.

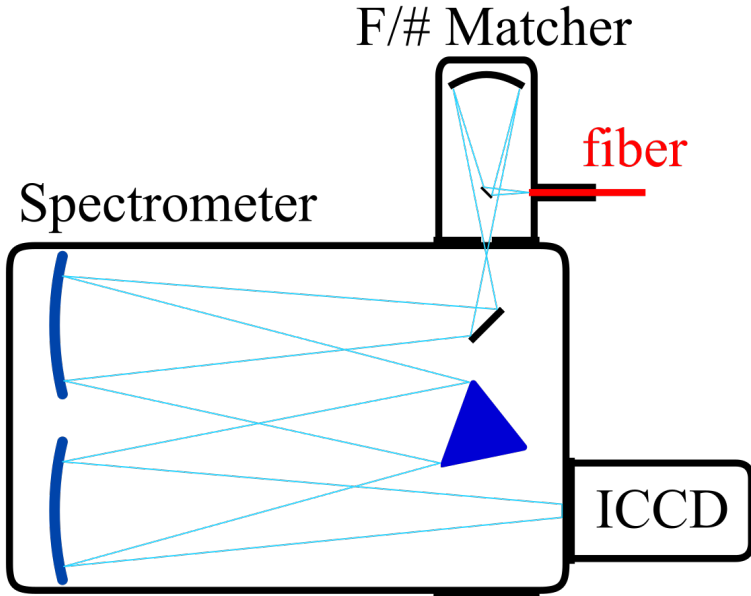


Figure 3.9: Working principle of a spectrograph and an f-number matcher

The monochromator disperses the incoming light using a diffraction grating, separating it into its constituent wavelengths. Three interchangeable diffraction gratings (2400 gr mm^{-1} , 1200 gr mm^{-1} , and 600 gr mm^{-1}) (the blue triangle in 3.9) are employed to achieve varying spectral resolutions and spectral ranges. The selected light is then directed onto the ICCD camera.

The gating capability of the ICCD allows precise temporal resolution, enabling the capture of transient events or the rejection of unwanted background light. By synchronizing the ICCD with the light source or other experimental triggers, time-resolved emission spectra can be obtained. The digital signal from the ICCD is then processed to analyze the intensity and wavelength of the emission, providing insights into the chemical composition and physical properties of the source.

In the following plot (Fig. 3.12), the operation of the temporal windows is illustrated. The discharge is set to operate at a frequency of 200 Hz. It is possible to adjust the delay with which the delay generator sends a signal to the generator relative to an arbitrary time reference (e.g., $500 \mu\text{s}$ in the plot) and the duration for which this signal remains active (onset = $5 \mu\text{s}$ in the plot). The rising edge of this signal triggers the generator and produces a high-voltage pulse with a duration of 10 ns. The nanosecond pulse generator adds a spurious delay to the discharge set rising edge (see "Effective discharge" in Figure 3.12). The effective delay of the discharge ignition with respect to the reference signal

is approximately $\Delta t_{\text{eff}} \approx 660\text{ns}$.

The generator can also operate in "burst mode," wherein two pulses are generated in succession with a predefined delay, which must not be shorter than $10\mu\text{s}$. This configuration was employed in the experiment using a series of two pulses in burst mode at a frequency of 200 Hz, with a temporal separation of $18\mu\text{s}$ between consecutive pulses. The hardware implementation of the auxiliary ns pulse was achieved with a custom-made OR-gate device(it sums up the original pulse sequence and the auxiliary pulse). This expedient allowed easily varying the impulse time delay without modifying the original pulse sequence[3.10].

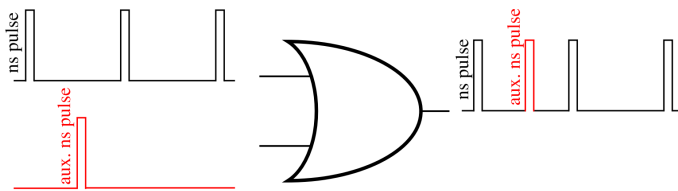


Figure 3.10: Schematics of the OR-gate used to add the auxiliary ns pulse to the pulsing scheme. The figure is taken by [40].

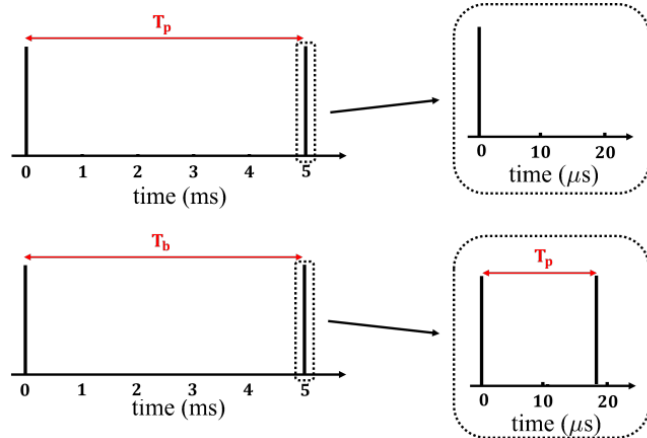


Figure 3.11: Top: Scheme of the continuous mode operating at a frequency of 200 Hz($T_p = 5\text{ ms}$). Bottom: scheme of a burst of two pulses separated by a time interval of $18\mu\text{s}$ operating at a frequency of 200 Hz. Adapted from [11].

The MCP and the CCD are both triggered by "Discharge reference". In particular, the CCD starts acquisition of approximately $30\mu\text{s}$ from the positive edge of the "Discharge reference", while the MCP must be configured to open at $500\mu\text{s} + \Delta t_{\text{eff}}$, ensuring that it is active when the discharge is initiated. The duration for which the MCP remains open (Δt_{MCP}) can be selected to achieve the desired temporal resolution. For instance, to investigate the time-resolved emission spectroscopy of the discharge, Δt_{MCP} can be set

to 10ns, allowing the MCP to open every 10ns and facilitating the study of the temporal evolution of the discharge emission. However, Δt_{MCP} cannot be shorter than the temporal jitter between the MCP opening and the delay generator signal. Moreover, for values below 5ns, the MCP gain becomes unstable.

If the signal from a single acquisition is weak, it can be enhanced by integrating over multiple acquisitions using the integration-on-chip (IOC) feature. The camera can integrate over multiple MCP exposures by setting the CCD exposure time to a specific value. In the plot, the CCD exposure time is configured to integrate over three signals ($T_{CCD} = (1/200\text{Hz}) \cdot 3 = 15\text{ms}$), allowing the camera to accumulate data from multiple MCP openings.

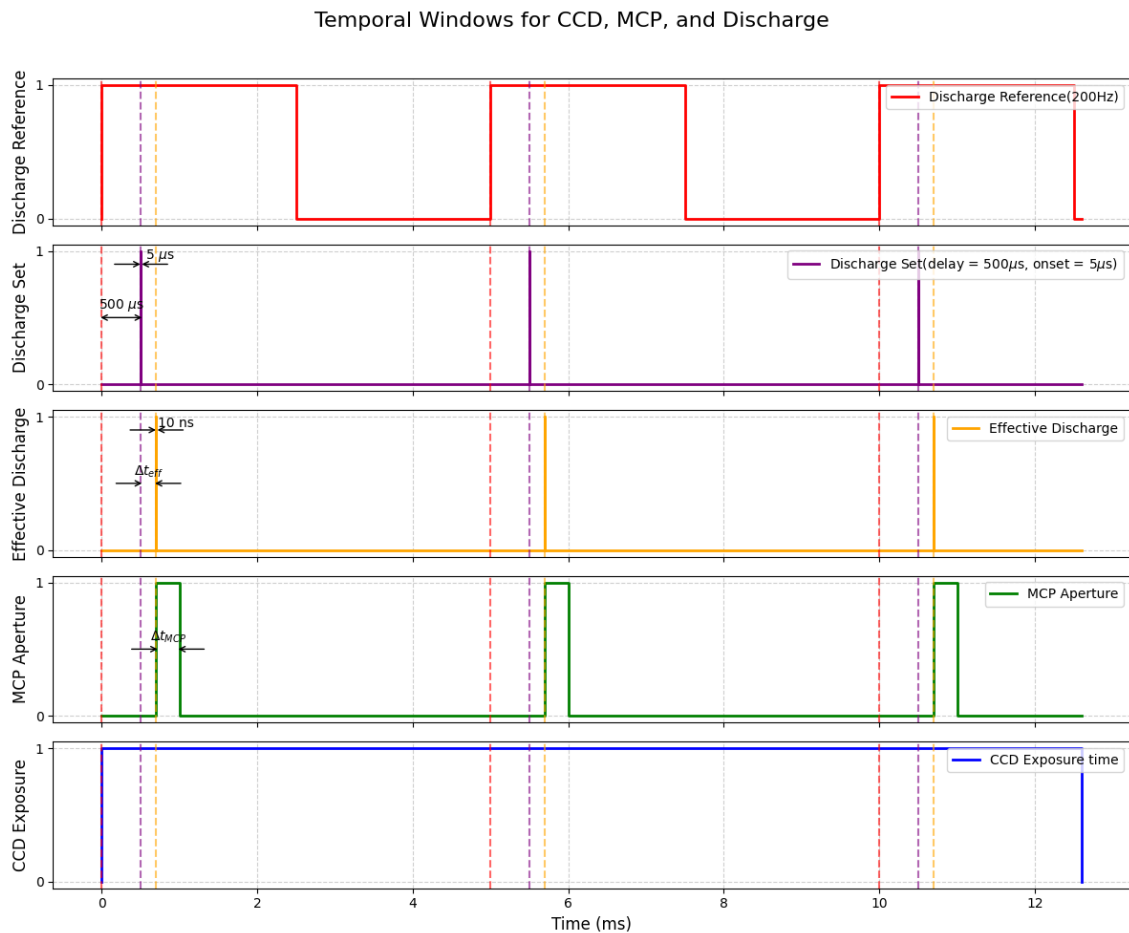


Figure 3.12: Temporal windows scheme for the emission spectroscopy acquisition(graph not to scale)



Figure 3.13: Picture of the camera

3.4.3 Spectrum calibration

The camera calibration was performed using a deuterium-halogen lamp (Avantes Avalight-DH-S), covering the spectral range from 200 nm to 900 nm. By comparing the known reference intensity of the lamp with the corresponding spectral measurements obtained from the camera, a calibration factor was determined. This factor is subsequently applied to the raw spectral counts to account for the camera response which depends on the wavelength.

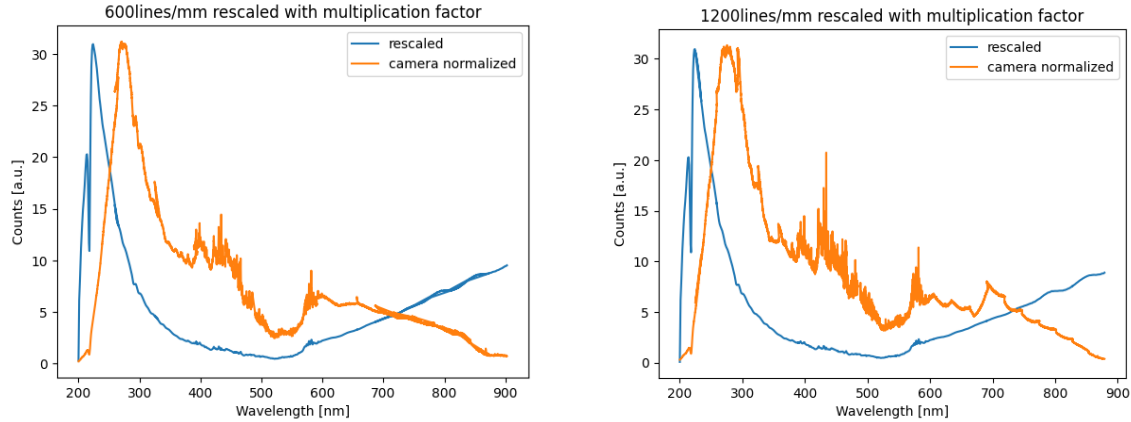


Figure 3.14: Comparison between the camera signal normalized and the signal after multiplication factor rescaling for 600 and 1200 lines/mm gratings

Following the calibration, baseline subtraction was conducted for all recorded spectra. The baseline was established by acquiring measurements in the absence of discharge, thereby accounting for background signals and instrumental noise.

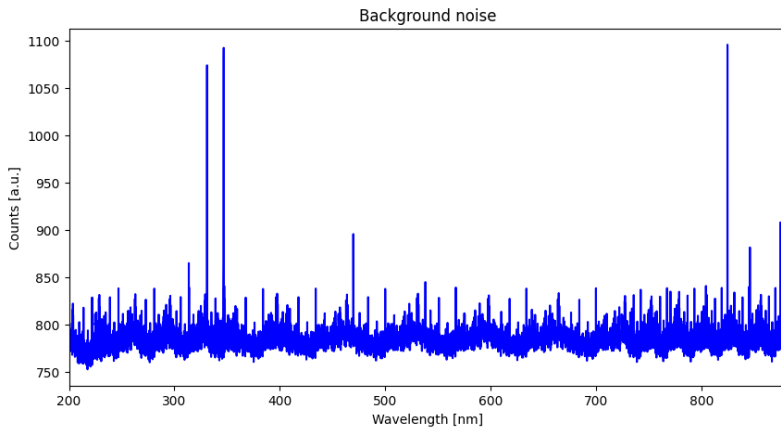


Figure 3.15: Background noise without the discharge

In cases where optical filters were employed, the measured signals were corrected by multiplying them with the wavelength-dependent transmission coefficients provided in the filter datasheets. This correction ensures that the spectral measurements accurately reflect the transmission characteristics of the filters across the relevant wavelength range.

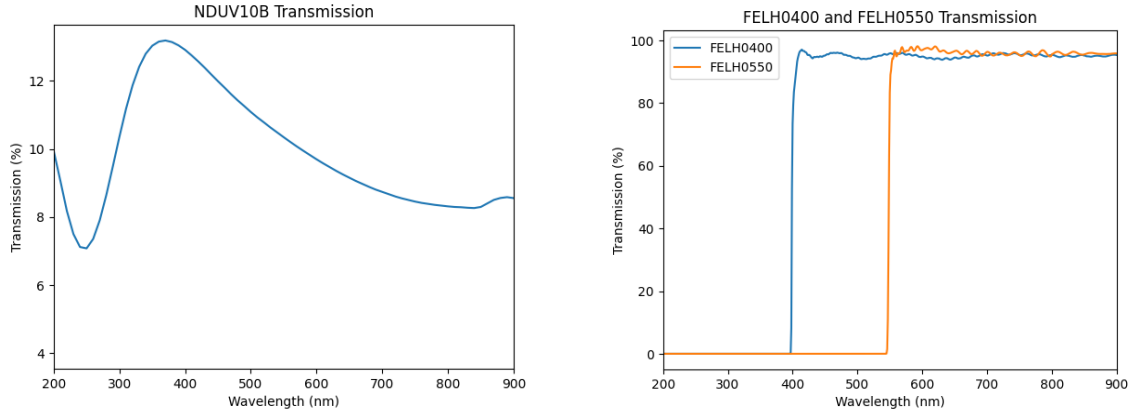


Figure 3.16: NDUV10B, FEL 0400 and FEL 0550 transmission as a function of wavelength [41]

3.4.4 Spectra noise

The noise impacting the spectral measurements can be categorized into three distinct components: readout, thermal, and environmental noise. The set temperature of the camera governs thermal noise, while readout noise is inherent to the measurement process and is determined by the intrinsic noise characteristics of the camera system. The optical setup is enclosed within a black plastic enclosure to mitigate environmental noise, providing a controlled environment that minimizes external interference, as shown in the figures 3.17 and 3.7.



Figure 3.17: Picture of the gas feed system, camera, and the black plastic box that covers the optical setup

Chapter 4

Data Analysis

4.1 Delay and parasitic line capacitance calculation

To accurately determine the energy dissipated during the discharge process, it is essential to account for the delays introduced by the voltage and current probes, cables, and oscilloscope input stages. This analysis requires a constant circuit impedance, prompting the collection of current-voltage (I - V) data when the discharge is not ignited. Under these conditions, the current consists solely of the so-called "displacement current":

$$I_{\text{disp}}(t) = C \frac{dV(t)}{dt} \quad (4.1)$$

Here, C represents the parasitic capacitance of the circuit, which arises from the voltage probe and the reactor. Measurements of I_{disp} and V as functions of time are acquired using an oscilloscope.

To estimate the delay between the displacement current and the voltage signal, a fitting routine is employed to model the measured current with the function:

$$I_{\text{disp}}(t) = A \frac{dV(t + d)}{dt} \quad (4.2)$$

where A and d are the fit parameters, corresponding to the parasitic capacitance and the delay, respectively.

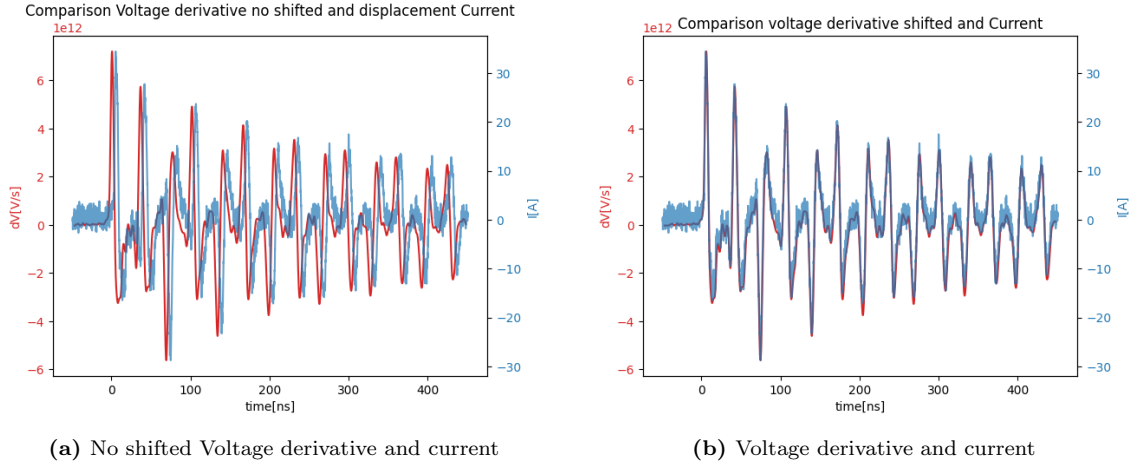


Figure 4.1: Comparison between voltage derivative shifted and no shifted and current curves without the discharge using N_2 as the injected gas

As additional proof of correct estimation of the delay, the energy dissipated in the circuit in the absence of discharge is evaluated. Since the load is purely reactive in these conditions, the energy integral should be zero:

$$E = \int_{\text{pulse}} I(t)V(t+d) dt = 0 \quad (4.3)$$

The absolute value of the energy is computed for various delay values (d), and the delay corresponding to the global minimum is identified.

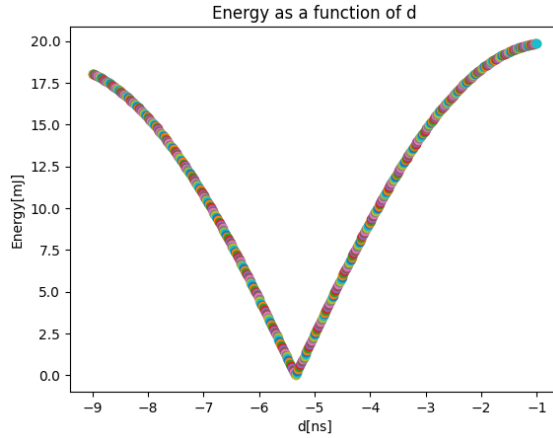


Figure 4.2: Energy as a function of the various delays

The best delay comes out to be $d = -5.3 \pm 0.3\text{ns}$ and the best $A = 4.0 \pm 0.4\text{pF}$. When applied to periodic functions, the minimum-based method of E yields multiple local minima due to the oscillatory nature of the signals involved. Specifically, this method is

based on the condition that the integral of the current V and I overtime must be zero in the absence of discharge. However, since I and V exhibit multiple local extrema (rebounds), their quasi-periodic behavior leads to multiple points where the integral condition is satisfied. Consequently, identifying the absolute minimum requires an initial fitting procedure. This fitting step is critical for constraining the search space for the global minimum and mitigating the ambiguities introduced by the presence of multiple local minima.

In the following plot, the voltage and current as functions of time are displayed both before and after the time shift. It is evident that, following the time shift, the voltage and current increase simultaneously during the initial pulse.

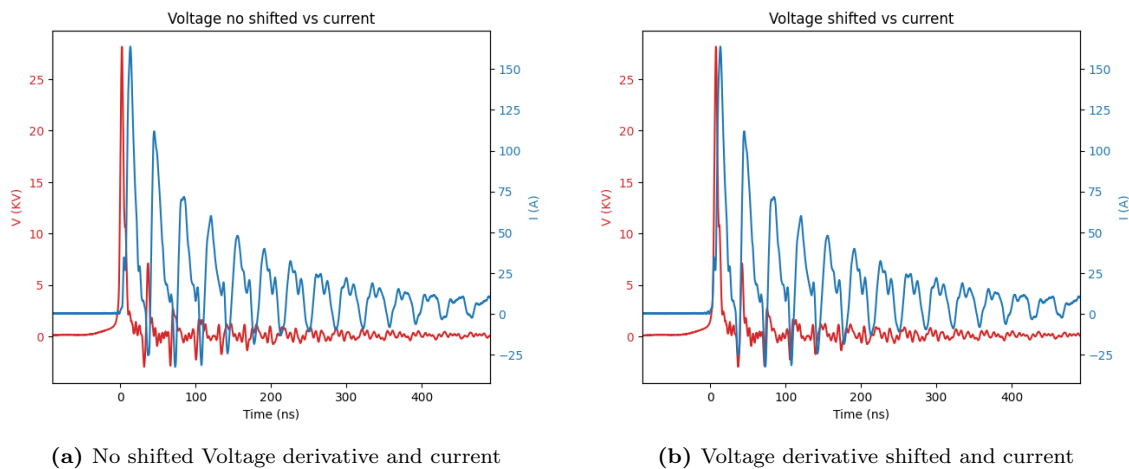


Figure 4.3: Comparison between voltage shifted and no shifted with current curves with the discharge

4.2 Temporal jitter

The delay generator produces a clock signal simultaneously transmitted to the spectroscopy camera and the high-voltage nanosecond power supply, as described in Section 3.4.2. The temporal offset between the microchannel plate (MCP) activation and the signal that initiates the discharge is called the *temporal jitter*.

The temporal fluctuations between the MCP activation and the discharge trigger provide an estimate of the uncertainty in the time resolution when tracking the emission evolution of the discharge. Specifically, the MCP exposure time determines the minimum temporal resolution achievable in time-resolved emission spectroscopy. If the MCP exposure time, Δt_{MCP} (see Figure 3.12), is equal to the temporal jitter, then the error associated with the time evolution of the discharge emission corresponds to the MCP aperture time.

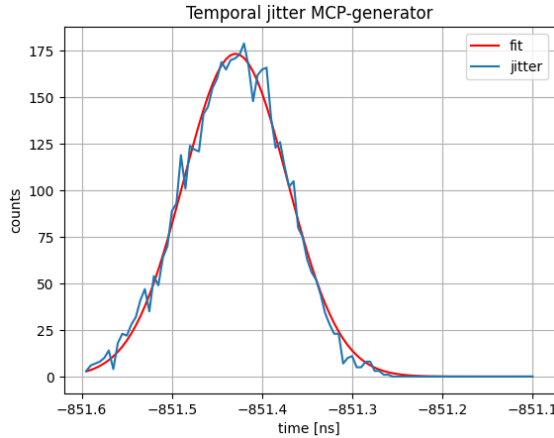


Figure 4.4: Temporal jitter between the MCP aperture signal and the generator signal

Figure 4.4 displays the time difference distribution between the "MCP Aperture" and the "Discharge Set" signals(see Figure 3.12). The standard deviation of this distribution, obtained as the sigma of the Gaussian fit to the data, is $\approx 60\text{ps}$.

The plot 4.5 illustrates the temporal jitter between the "Effective Discharge" and the "MCP Aperture" signals, operating at a frequency of 100 Hz, and the MCP aperture.

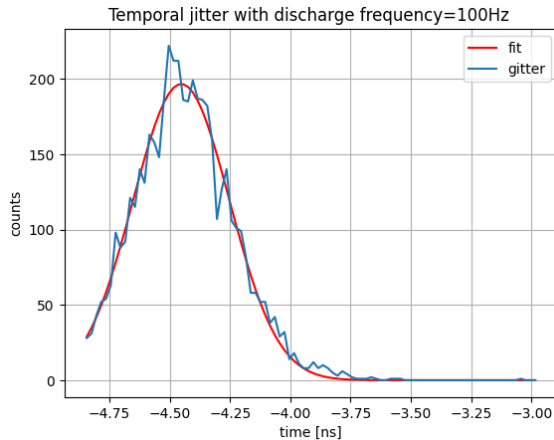


Figure 4.5: Temporal jitter between discharge voltage signal and MCP aperture, discharge frequency: 100 Hz

The standard deviation of this jitter is approximately 200ps . This increase indicates that an additional jitter is introduced during the ignition of the discharge.

When employing the integration-on-chip (IOC) method for 20 signals at a discharge frequency of 200 Hz, the temporal jitter is presented in Figure 4.6.

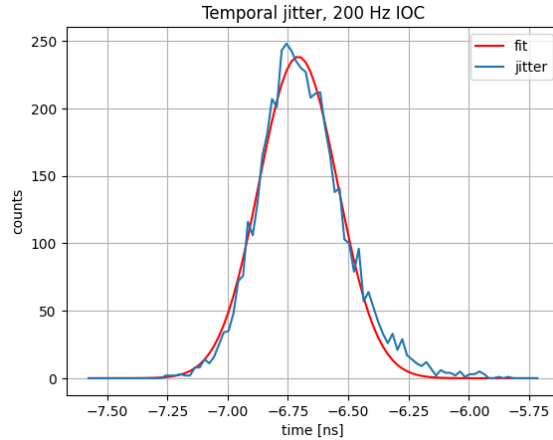


Figure 4.6: Temporal jitter using integration on chip (IOC) on 20 pulses at a discharge frequency of 200 Hz

The standard deviation, approximately 160ps , decreases further as the discharge frequency increases.

During time-resolved emission spectroscopy measurements, a discharge frequency of 200 Hz is used, with the IOC integrating over 20 pulses. Consequently, the temporal uncertainty in the measurements is 160 ps. Given this uncertainty, setting a minimum exposure time for the MCP of $\Delta t_{\text{MCP}} = 5 \text{ ns}$ can be considered a reasonable choice.

4.3 Impedance matching

4.3.1 Impedance matching

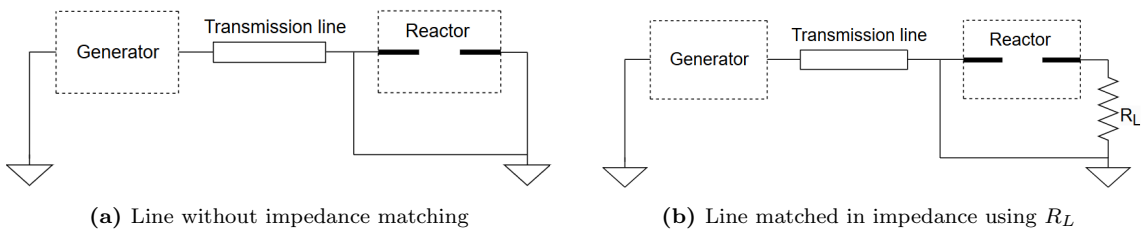


Figure 4.7: Line matched and unmatched in impedance

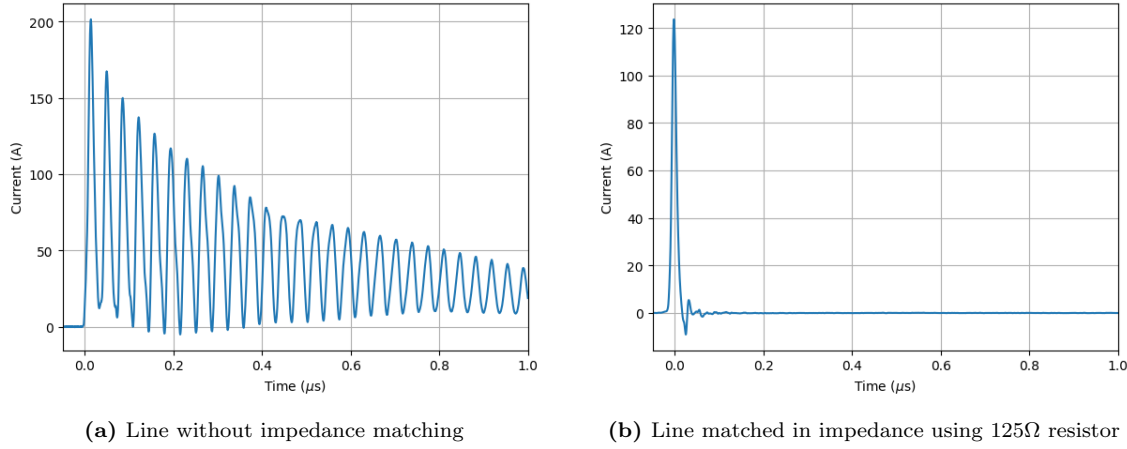


Figure 4.8: Current as a function of time for the line matched and unmatched in impedance

In order to perform absorption-emission spectroscopy on the first pulse without reflections, impedance matching with the transmission line at 75Ω was implemented. Initially, two 150Ω resistors were connected in parallel between the generator and ground to minimize power dissipation in the resistors. However, an impedance unmatch was still observed. In particular, by evaluating the ratio between the maximum voltage and current, the effective resistance of the circuit was found to be lower than 75Ω , indicating that the impedance was not adequately matched.

To address this issue, various resistor configurations were tested.

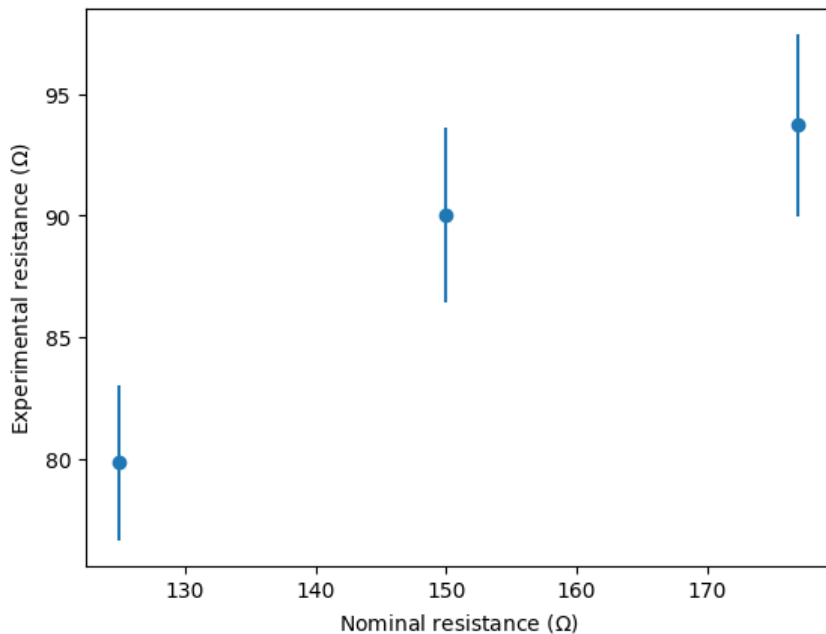


Figure 4.9: Experimental resistance as a function of the nominal resistance, 1Hz and 75% generator power, the resistance is evaluated as $R = \frac{V_{max}}{I_{max}}$

The optimal impedance matching was achieved using a nominal resistance of 125Ω , implemented by placing three 150Ω resistors in parallel in series with two additional 150Ω resistors in parallel.

The primary reason for this behavior is that, despite the low signal repetition rate (1 Hz), the extremely fast potential drop (on the order of nanoseconds) causes the real resistor to deviate from purely ohmic behavior. Instead, it exhibits parasitic effects—primarily capacitance and, to a lesser extent, inductance—that influence its impedance.

The physical structure of the resistor, as well as its mounting configuration, introduces a small capacitance between its terminals. When the potential changes on a nanosecond timescale, this capacitance presents a low impedance, partially bypassing the resistor and leading to a measured impedance (given by V_{\max}/I_{\max}) lower than its nominal value.

A signal with a rapid voltage drop contains transient components that interact with parasitic elements. These parasitic effects become relevant even at low signal frequencies when the transition time is extremely short, leading to a deviation from the expected resistor behavior. Consequently, the instantaneous voltage-to-current ratio appears lower than the nominal resistance value.

To compensate for this phenomenon and achieve proper impedance matching to the network (75Ω), a resistor with a higher nominal value (125Ω) must be selected so that, at the timescale of interest, the effective impedance equals $80 \pm 3 \Omega$.

Thus, the apparent decrease in resistance is due to the transient response of parasitic components—particularly capacitance—which reduces the total impedance when the potential varies very rapidly.

4.3.2 Dependence of Circuit Resistance on Voltage Maximum

To further investigate the variation in circuit resistance, the generator power percentage was adjusted, thereby varying the maximum voltage, while maintaining a nominal resistance of 125Ω . This approach enabled an analysis of how the circuit resistance changes as a function of the voltage maximum.

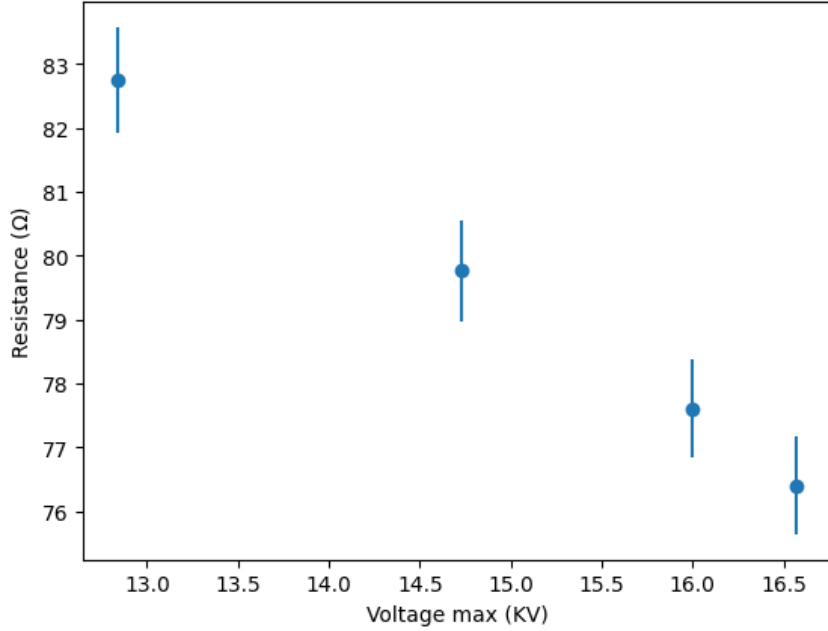


Figure 4.10: Experimental resistance as a function of the generator's voltage maximum using a nominal resistance of 125Ω at 1 Hz. The resistance is evaluated as $R = \frac{V_{\max}}{I_{\max}}$.

As illustrated in Figure 4.10, the experimental results indicate that an increase in the voltage maximum, which corresponds to an increase in the rate of potential drop, results in a linear decrease in the measured resistance.

4.3.3 Dependence of Impulse Time Delay on Impedance matching

To investigate the variations in line-matching impedance as a function of gas pre-ionization, the generator is operated in burst mode, delivering two consecutive pulses separated by a time interval of $18\ \mu s$ at a repetition frequency of 200 Hz. The purpose of the first pulse is to pre-ionize the gas, thereby reducing its initial impedance. Consequently, when the second pulse is applied, the gas no longer presents an effectively infinite impedance. As a result, the generator interacts primarily with the impedance introduced downstream of the reactor, which is designed to be impedance-matched.

The resistance, determined as the minimum of $\frac{V}{I}$ in the time window of the breakdown with V and I aligned using the delay found as explained in the Data Analysis section, is plotted as a function of the time interval between two successive pulses. The uncertainty in the resistance measurement is estimated as the standard deviation across ten acquisitions. As illustrated in Figure 4.11, the resistance exhibits a linear decrease as the logarithm of the time delay of the second pulse decreases. The resistance values are considered reliable

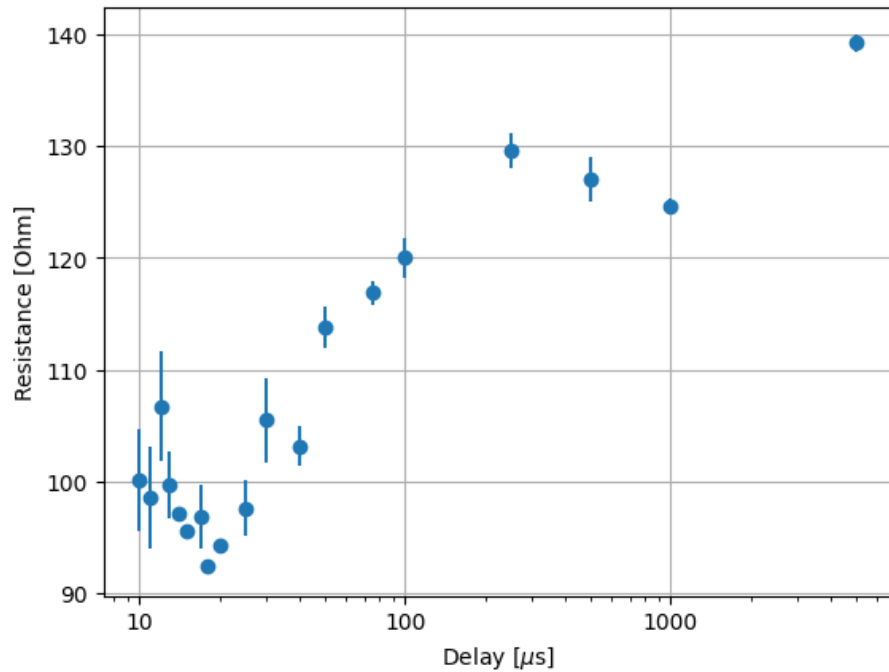


Figure 4.11: Resistances calculated as the minimum of $\frac{V}{I}$ after the breakdown as a function of the time interval between the two pulses in burst mode(200 Hz).

only when the discharge undergoes breakdown within the first few nanoseconds of the voltage rise.

Chapter 5

Results

5.1 Time Resolved Optical emission spectroscopy(TR-OES)

In the results section, time-resolved optical emission spectroscopy (TR-OES) is employed to analyze the temporal evolution of species generated in a CO₂ discharge. Initially, a comparative analysis is conducted with the work of Ceppelli et al.([1]) under similar experimental conditions: an electrode gap of 5.5 mm, the same CO₂ flow rate, and an impedance-unmatched transmission line. Due to this impedance unmatch, both the current-voltage (IV) characteristics and the emission profile exhibit oscillatory behavior. The discharge is initiated at a frequency of 200 Hz in continuous mode, using single-pulse excitation (5.2).

Then, thanks to the possibility of moving the fiber along the discharge axis, TR-OES measurements are performed near the cathode with the same electrode gap to investigate spatial variations in the emission profile.

Subsequently, impedance matching is introduced by incorporating an effective 80 Ω resistor(R_L) downstream of the cathode (see section 4.3.1 and Figure 4.7).

The electrode gap is reduced to 2.4 mm, facilitating an earlier breakdown. In combination with burst mode operation, this reduction in gap impedance allows the overall impedance in the second pulse to approach zero. In burst mode, the second pulse exhibits diminished oscillations due to the memory effect (as discussed in Section 1.7), which drives the gap resistance toward zero. Consequently, the generator effectively perceives only the resistance downstream of the cathode, which is matched to the transmission line impedance. This configuration enables a more precise characterization of the emission profile corresponding to the first peak in emission intensity, minimizing the influence of rebound effects. TR-

OES measurements are performed for both pulses in the burst sequence(5.5).

TR-OES measurements are also taken for the second pulse of the burst mode with the line unmatched in impedance with an electrode gap of 2.4mm(5.4).

First, the current-voltage (IV) characteristics, cumulative energy, and power are analyzed for each configuration. Subsequently, optical emission spectra at selected time delays after discharge initiation (20 ns, 100 ns, and 200 ns) are examined to investigate the temporal evolution of the emitting species. This analysis provides insights into the progression of optical emissions and enables the identification of species appearing at different time intervals. The chosen time delays correspond to key phases of the discharge: shortly after breakdown (20 ns), during the final stage of the primary optical emission associated with the first current rebound in the impedance-matched configuration (200 ns), and at an intermediate stage (100 ns).

Finally, line integrals of specific atomic emissions are presented alongside the current and phototube signal for each configuration to gain deeper insight into the emission profiles of selected species. The transitions for the atoms analyzed are summarized in the following table 5.1:

Species	Transition	Wavelength (nm)
C	$2p^2 \ ^1P_2 \leftarrow 3s \ ^1P_1^0$	247.86
C ⁺	$2p^2 \ ^2P_{1/2,3/2} \leftarrow 2p^3 \ ^2D_{3/2,5/2}^0$	250.91, 251.21
C ⁺⁺	$2p \ ^1P_1^0 \leftarrow 2p^2 \ ^1P_2$	229.68
O	$3s \ ^5S_2^0 \leftarrow 3p \ ^5P_{1,2,3}$	777.19, 777.42, 777.54

Table 5.1: Spectral lines of carbon and oxygen observed in the experiment, identification using [42].

The main molecular transitions seen during the experiment are:

Species	Transition	Wavelength Range (nm)
CO	(A $^1\Pi \rightarrow X \ ^1\Sigma$) Fourth Positive System (4PS)	140 – 280
CO	(b $^3\Sigma \rightarrow a \ ^3\Pi$) Third Positive System (3PS)	260 – 380
CO ₂ ⁺	(A $^2\Pi \rightarrow X \ ^2\Pi$) Fox Duffendack Barker System (FDBS)	285 – 450
CO ₂ ⁺	(B $^2\Sigma \rightarrow X \ ^2\Pi$) $\lambda\lambda$ 2883 – 2896 System	\sim 290

Table 5.2: Summary of observed molecular emission systems, identification using [43], [44], [45], [46].

5.2 TR-OES - Transmission line unmatched in impedance

For the first configuration, the discharge is initiated using a single pulse at 200 Hz with an electrode gap of 5.5mm, and the study is done in the center of the electrode gap. Due to an impedance unmatch in the transmission line, the IV curves exhibit signal reflections(as

we can see in 5.1 and in 5.7 for the phototube and current curves). The mean energy deposited in the discharge is 19.6 ± 0.2 mJ. It is noteworthy that the majority of the energy is deposited during the initial few nanoseconds, corresponding to the breakdown phase.

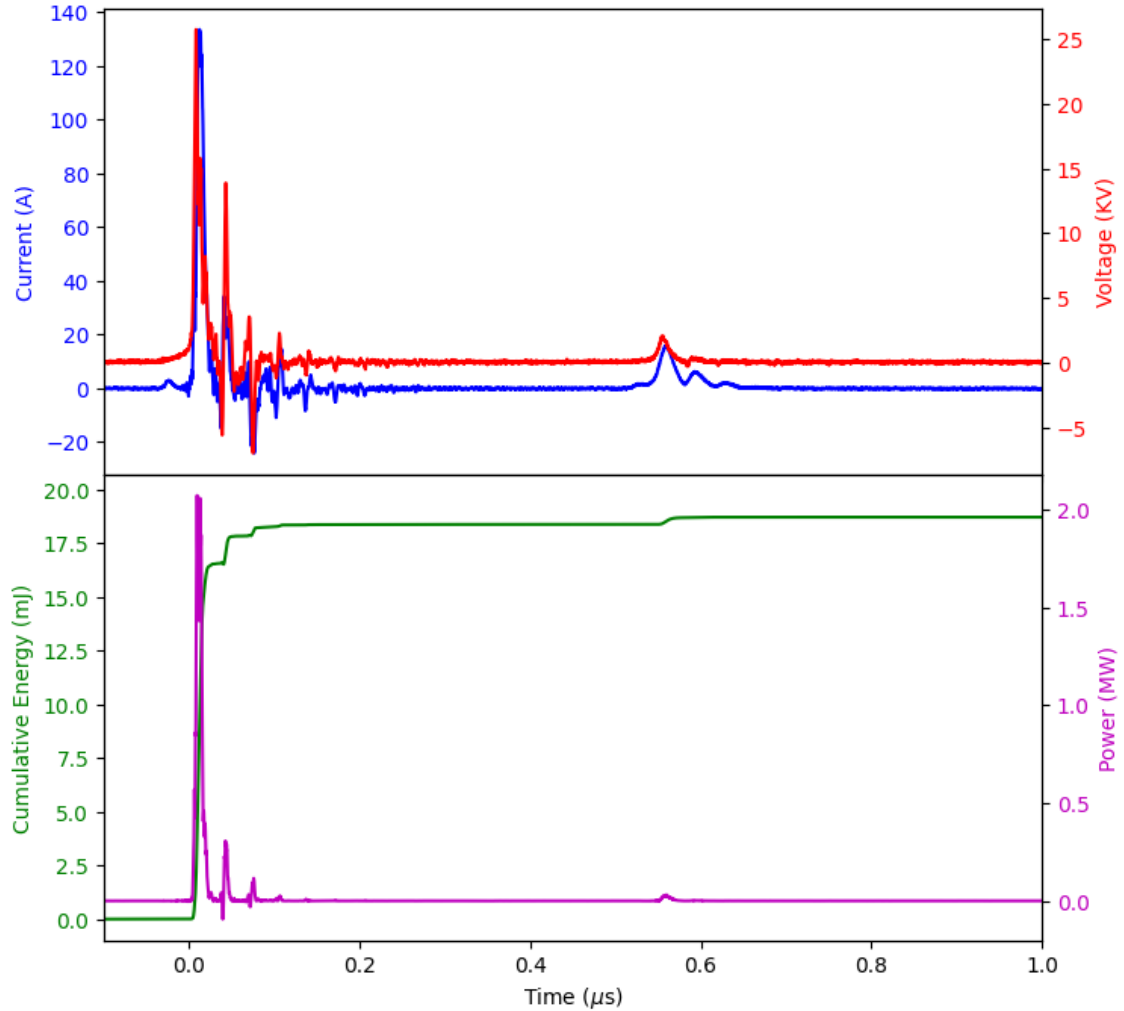


Figure 5.1: IV characteristics in the upper plot and energy and power in the bottom plot for the line with unmatched impedance, 5.5 mm electrode gap, and 200 Hz operation in continuous mode.

In the following plots, the spectra are presented as a function of wavelength, with intensity expressed in arbitrary units (counts) at 20 ns, 100 ns, and 200 ns after discharge ignition.

Initially, molecular bands and ionic species dominate the emission, as shown in Figure 5.3, which presents a zoomed-in view of the molecular emission between 280–390 nm at 0 ns after discharge ignition. The presence of CO 3PS, CO_2^+ FDBS, and $\lambda\lambda$ systems can be identified, as summarized in Table 5.2. The emission from CO appears significantly

weaker compared to that of CO_2^+ , suggesting that ionization is the dominant process over dissociation.

Similarly, Figure 5.5 illustrates the emission at 200 ns, highlighting the presence of ionic species.

Neutral and ionic atomic lines are generally much more intense than molecular bands due to their higher Einstein coefficients. For instance, the CO Fourth and Third Positive System exhibit Einstein coefficients on the order of 10^{-7} s^{-1} or lower [47]. In contrast, these values are significantly higher for atomic and ionic species, such as C^{++} (229.68 nm) with $1.37 \times 10^8 \text{ s}^{-1}$ and C^+ (251.2 nm) with $5.61 \times 10^7 \text{ s}^{-1}$, as reported in the NIST Atomic Spectra Database [42]. Furthermore, the atomic emission population is concentrated in relatively narrow spectral lines, whereas molecular emission is distributed over broader bands due to the additional rotational and vibrational degrees of freedom.

Consequently, following the 20 ns spectrum, a progressive decrease in molecular band emissions and atomic ion intensities is observed(Figures 5.4, 5.5), and the atomic lines of carbon and oxygen become dominant.

At 100 ns and 200 ns, there is also an evident broadening of the neutral atomic species due to the Stark effect(Figures 5.4, 5.5).

It can be observed that a continuum emission is present in the 20 ns spectra, which can be attributed to electron recombination and electron-neutral/ion Bremsstrahlung. This last phenomenon has been widely reported in atmospheric pressure discharges [48]–[54].

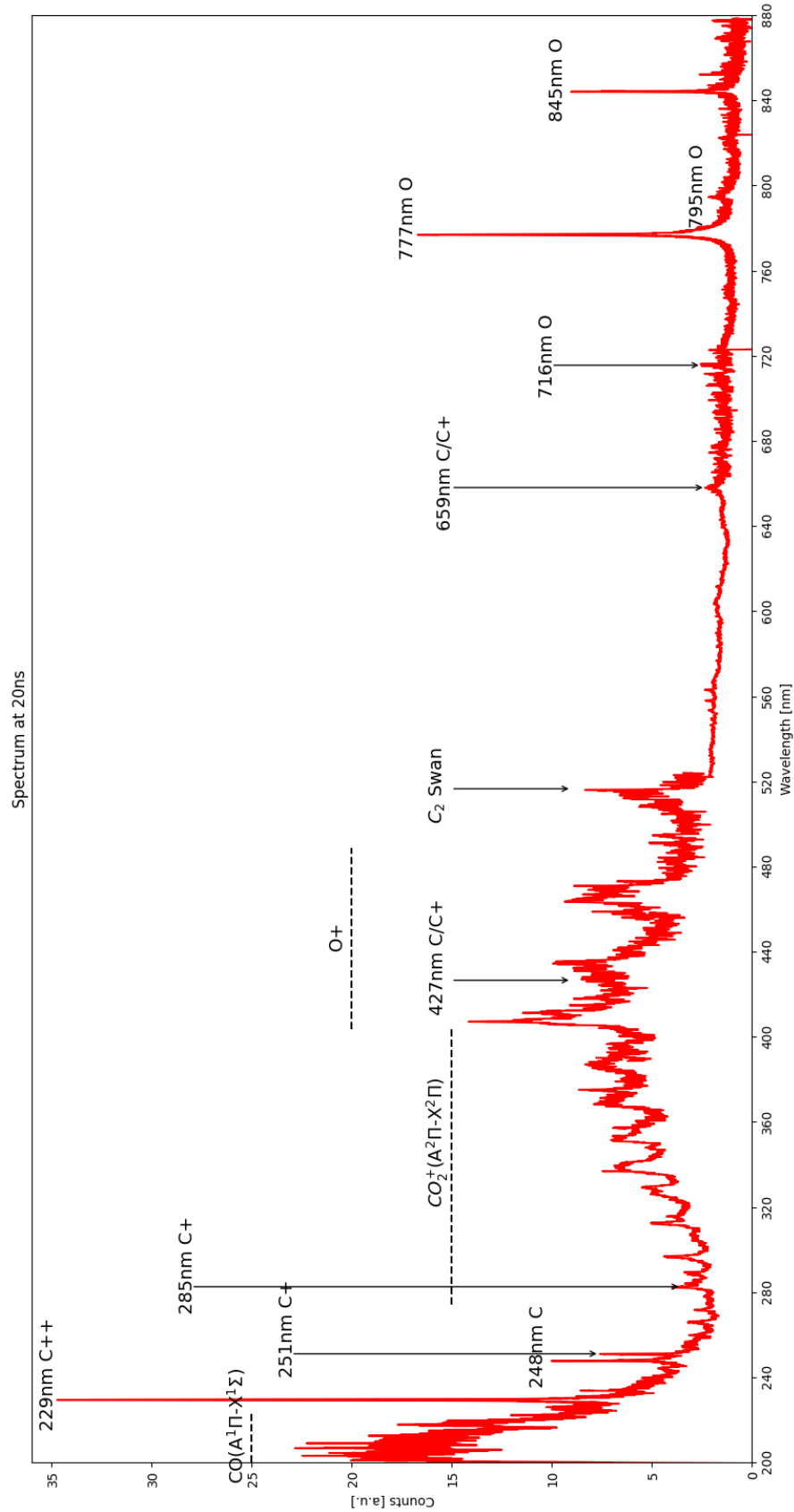


Figure 5.2: Spectrum 20ms after the start of the discharge for 200Hz unmatched in impedance, 5.5mm electrodes gap, the MCP exposure time is set to 5 ns.

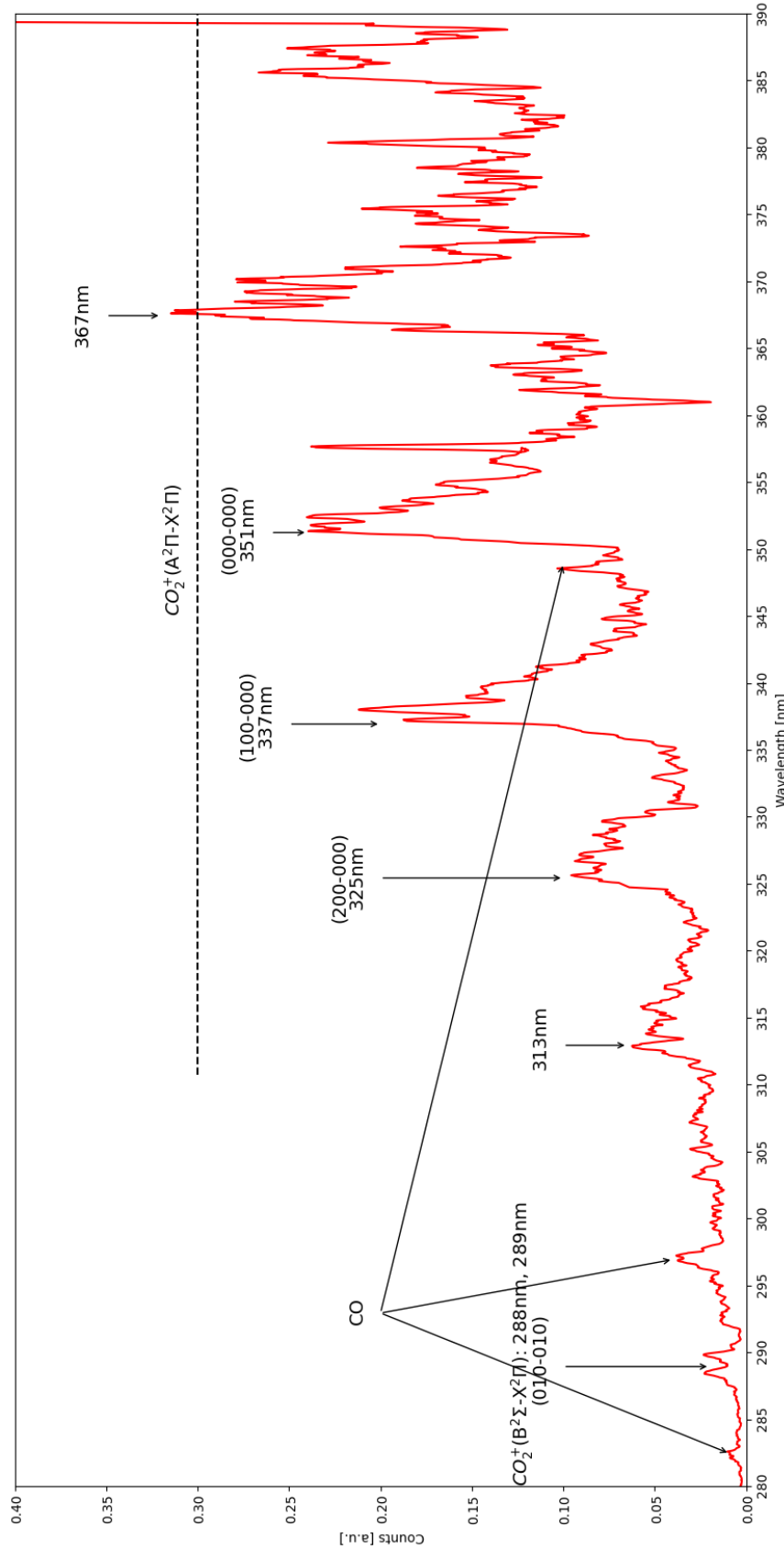


Figure 5.3: Molecular bands at 1ns after the start of the discharge for 200Hz unmatched in impedance, 5.5mm electrodes gap, the MCP exposure time is set to 5 ns.

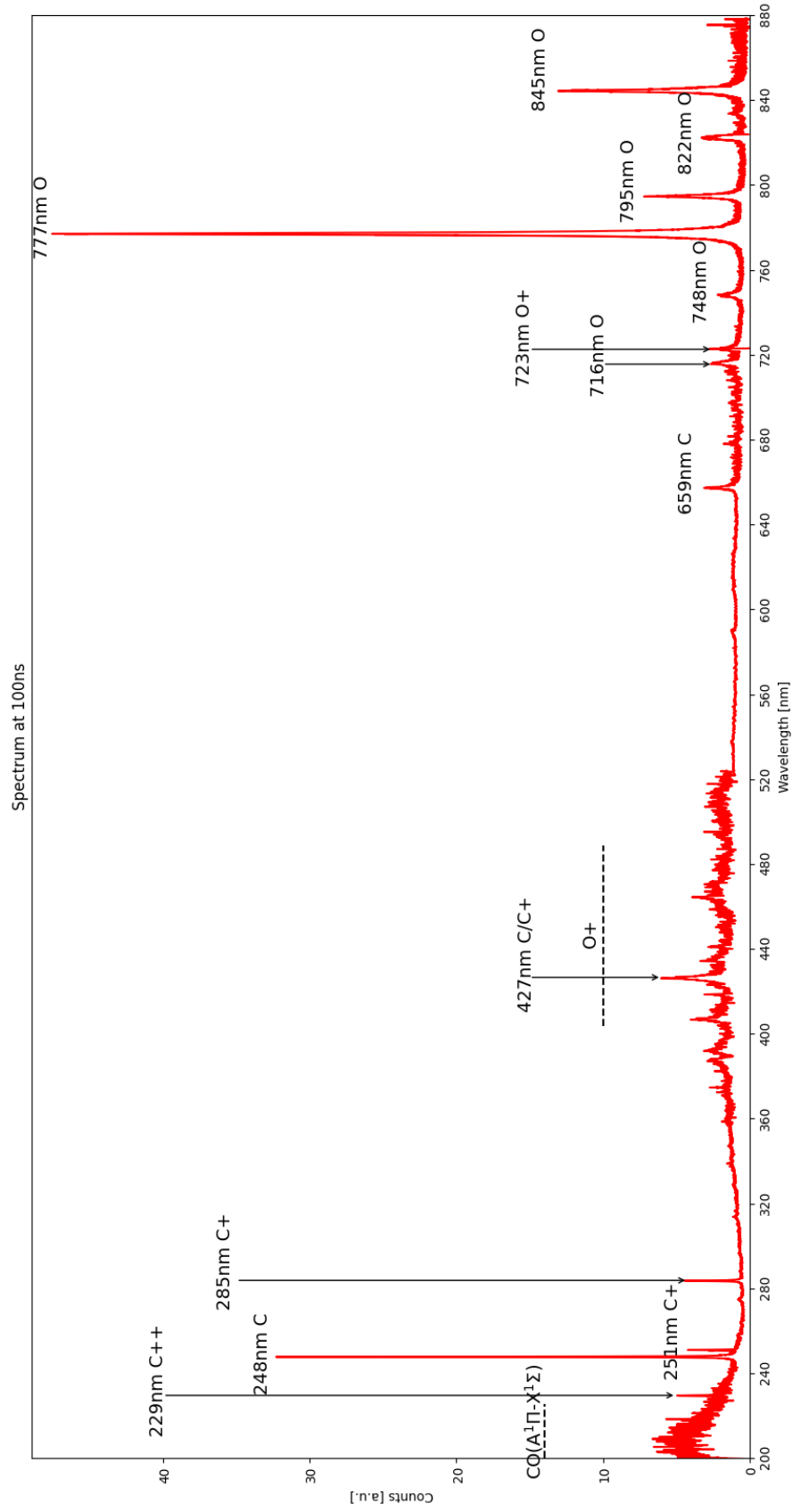


Figure 5.4: Spectrum 100ns after the start of the discharge for 200Hz unmatched in impedance, 5.5mm electrodes gap, the MCP exposure time is set to 5 ns.

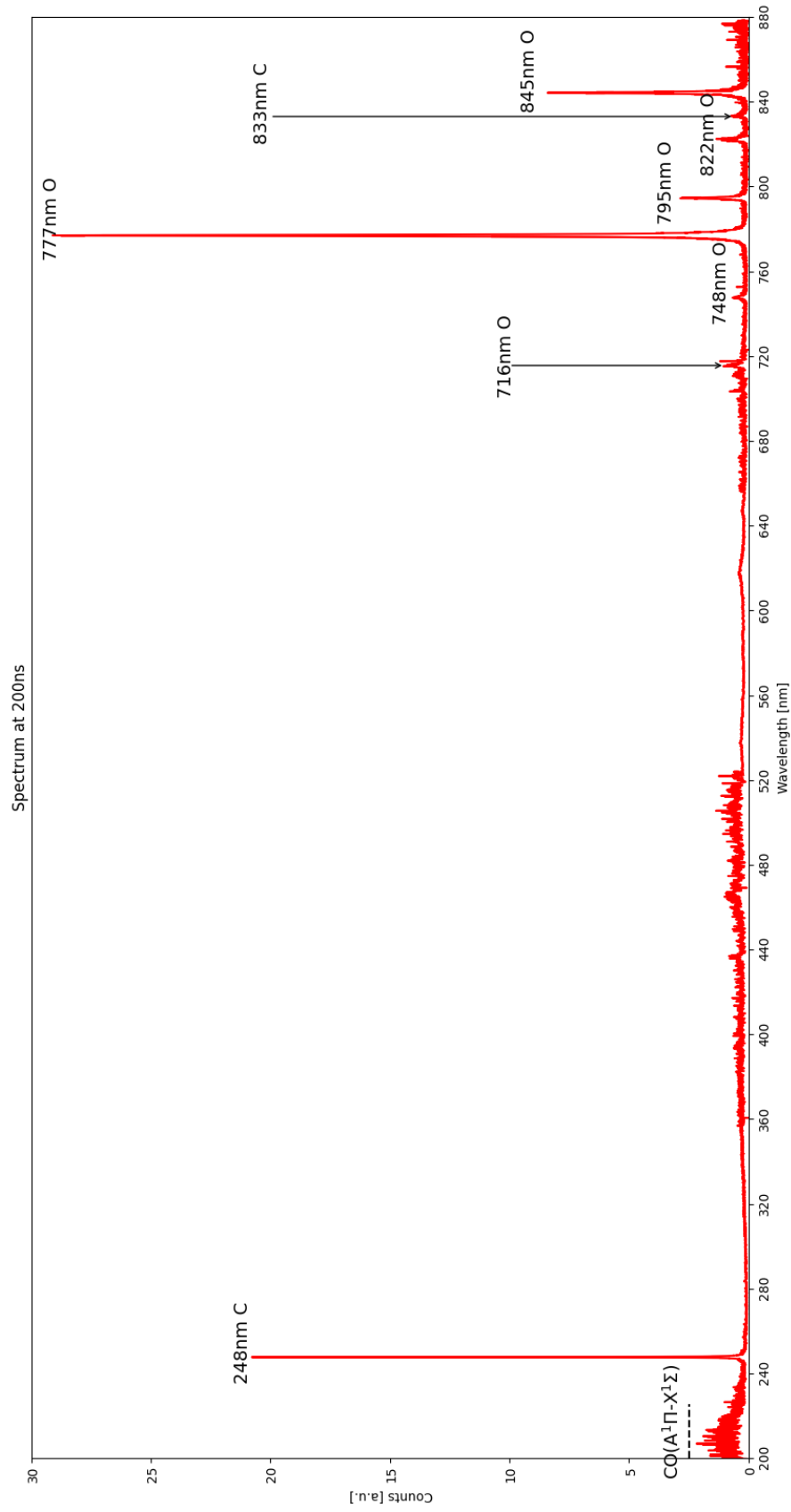


Figure 5.5: Spectrum 200ns after the start of the discharge for 200Hz unmatched in impedance, 5.5mm electrodes gap, the MCP exposure time is set to 5 ns.

The spectra are consistent with the findings of Ceppelli et al. [1]. Specifically, for Type I, with the discharge operating at 200 Hz, both the atomic and molecular emission lines observed are similar. Additionally, the O^+ emissions (400–480 nm) and the 427 nm emission from C and C^+ have been identified by referencing the work of Maillard et al. [55].

To gain a deeper understanding of the time progression of atomic and ion transitions, as well as discharge behavior (as done by Ceppelli et al. [1]), the integrals of the emission lines for selected atomic ions and atoms are plotted as a function of time. In particular, the emissions of C^{++} at 229 nm, C at 248 nm, C^+ at 251 nm, and O at 777 nm are considered (see Table 5.1).

The peak integral is determined by calculating the area under the emission peak after subtracting the baseline. The baseline is estimated as the average intensity between the start and end points of the peak. An example of this integration method is illustrated in the graph(5.6) for the case of atomic oxygen.

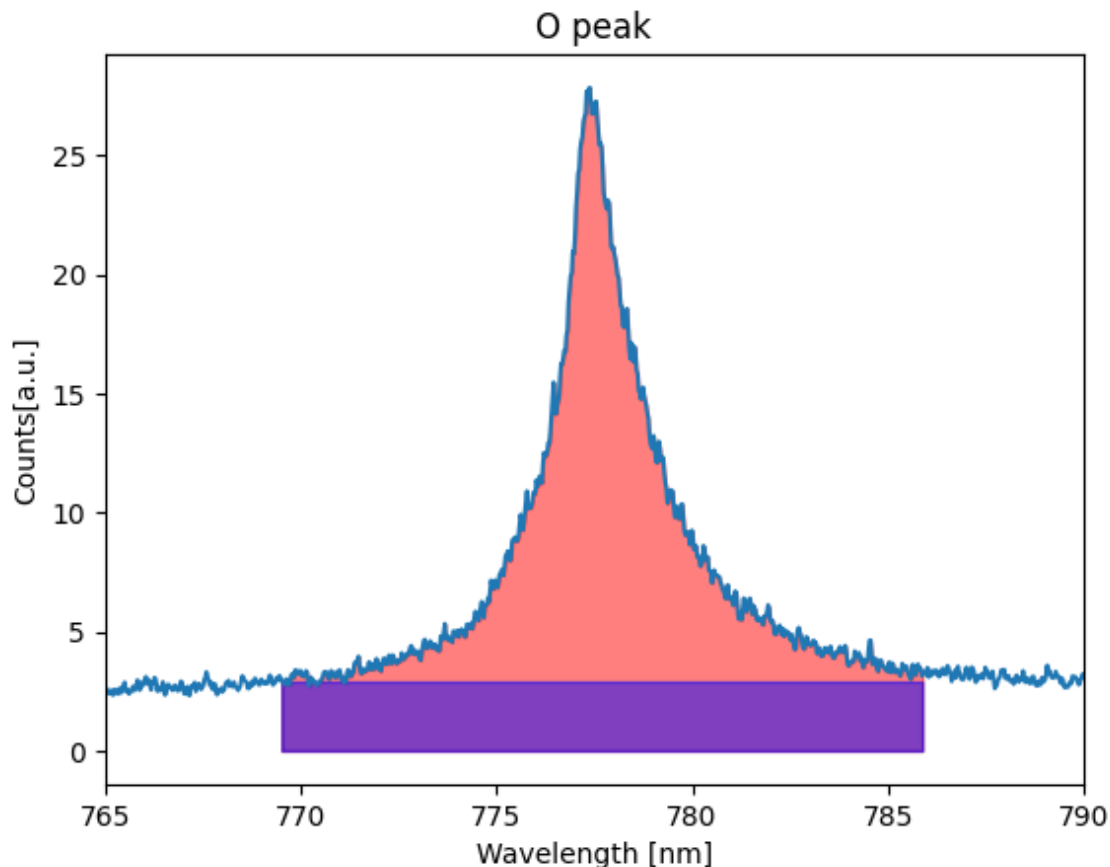


Figure 5.6: Integral of the oxygen peak at a given time: the red area represents the integrated emission, while the blue area corresponds to the baseline.

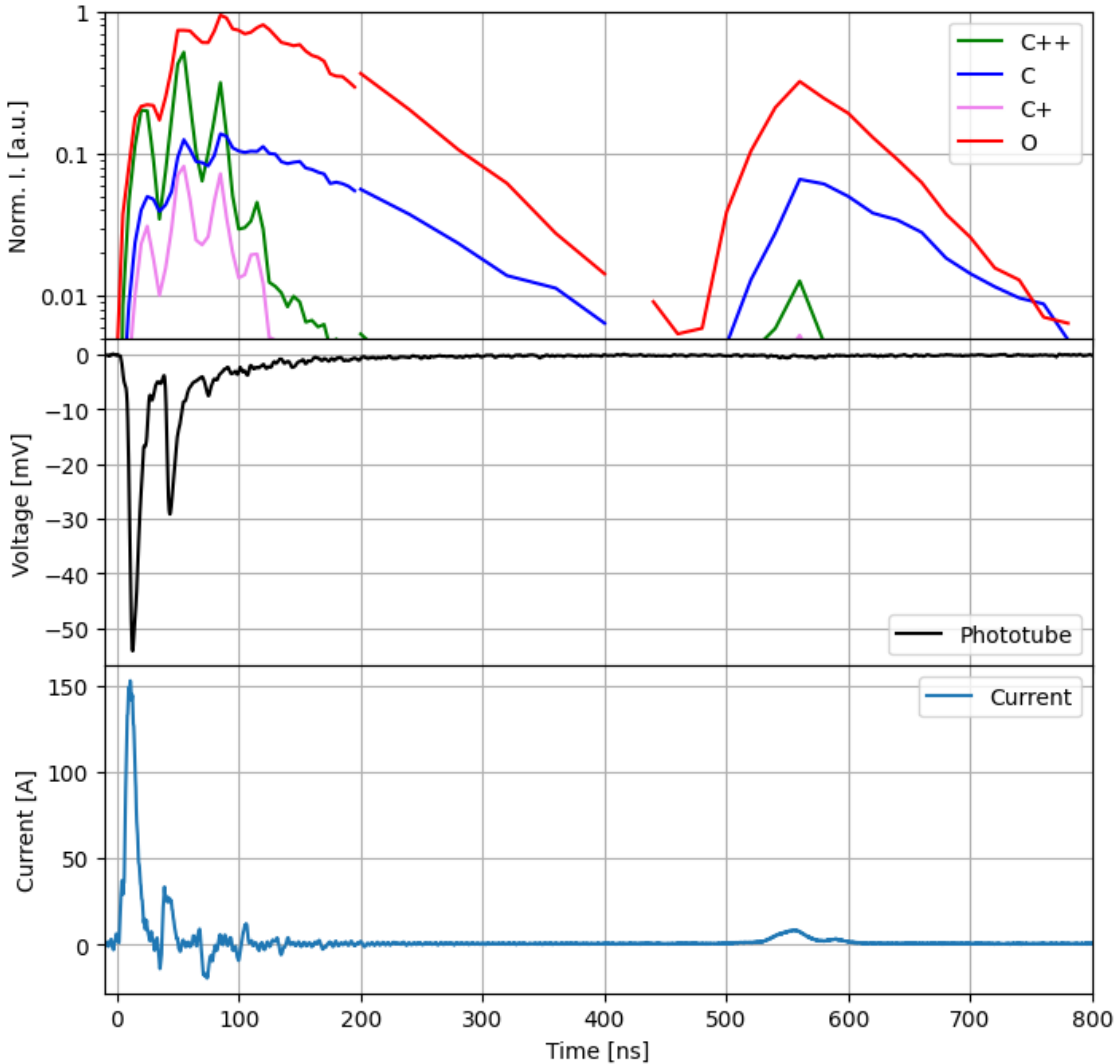


Figure 5.7: Time evolution of atomic lines in the centre of the electrodes gap (the y-axis is normalized to the maximum signal and expressed in logarithmic scale): C at 247.85 nm, C^+ at 250.91 nm and 251.21 nm, C^{++} at 229.68 nm and O triplet at 777.19 nm, 777.42 nm, 777.54 nm, the MCP exposure time is set to 5 ns for the time range 0–195 ns, 40 ns for 200–400 ns, and 20 ns for 440–880 ns.

In the first plot of 5.7, the integrated peak signals normalised(log scale) are shown as a function of time. The second plot displays the phototube signal, representing the overall emission profile of the discharge without spectral separation by the monochromator. The third plot illustrates the discharge current over time. The plots indicate a clear correlation between the emission profiles: each peak in the current is followed by a corresponding peak in the phototube signal and the integrated emission signal.

The current curve exhibits signal reflections between 0 and 200 ns due to impedance unmatched in the transmission line. Additionally, another re-trigger occurs at 550 ns.

The integrated peak signals exhibit reflections that follow the profiles of both the current

and phototube signals, with a re-emission observed at 550 ns. Notably, the maximum emission intensity of neutral oxygen and carbon atoms occurs during the third current rebound, whereas ionic carbon species reach their peak during the second rebound. Additionally, ion emission lines decay more rapidly over time, indicating fast recombination, while atomic lines persist much longer, decreasing at a significantly slower rate. This observation suggests that both ion and neutral atom emissions primarily originate from electron impact excitation. In contrast, the prolonged persistence of neutral carbon and oxygen lines might be due ascribed to different population mechanisms (e.g., energy transfer processes involving long-lived species) and/or different effective lifetimes.

5.3 TR-OES - Trasmission line unmatched in impedance at the cathode

To perform emission spectroscopy measurements at the cathode, the optical fiber is displaced by 1.3 mm toward the cathode image using a micrometer screw. This system allows precise adjustment of the fiber position both horizontally (along the anode-cathode direction) and along the optical axis to optimize image focus. These measurements provide valuable insights not only into the temporal dynamics but also into the spatial resolution of the discharge.

The spectra at 0ns for the molecules, 20 ns, 100 ns, and 200 ns are nearly identical at the center of the discharge and are therefore presented in the Appendix (7.1, 7.2, 7.3, 7.4). This observation suggests that the excited species are present in both regions of the discharge with similar temporal behavior.

It is interesting to examine in detail the temporal evolution of the integrals for neutral atomic species and atomic ions(Figure 5.8). In this configuration, the first emission peak is more pronounced for both neutral and ionic species compared to the center of the discharge (Figure 5.7). This suggests that the formation of atomic species is more intense near the cathode during the breakdown phase. In contrast, at the center of the discharge, the main peak in atomic emission occurs predominantly during the current rebounds. This observation implies that the excitation and formation processes at the discharge center require a longer timescale and multiple discharge events to reach their maximum intensity. Additionally, this behavior may be influenced by variations in the discharge channel,

potentially resulting in a lower energy density at the center of the plasma.

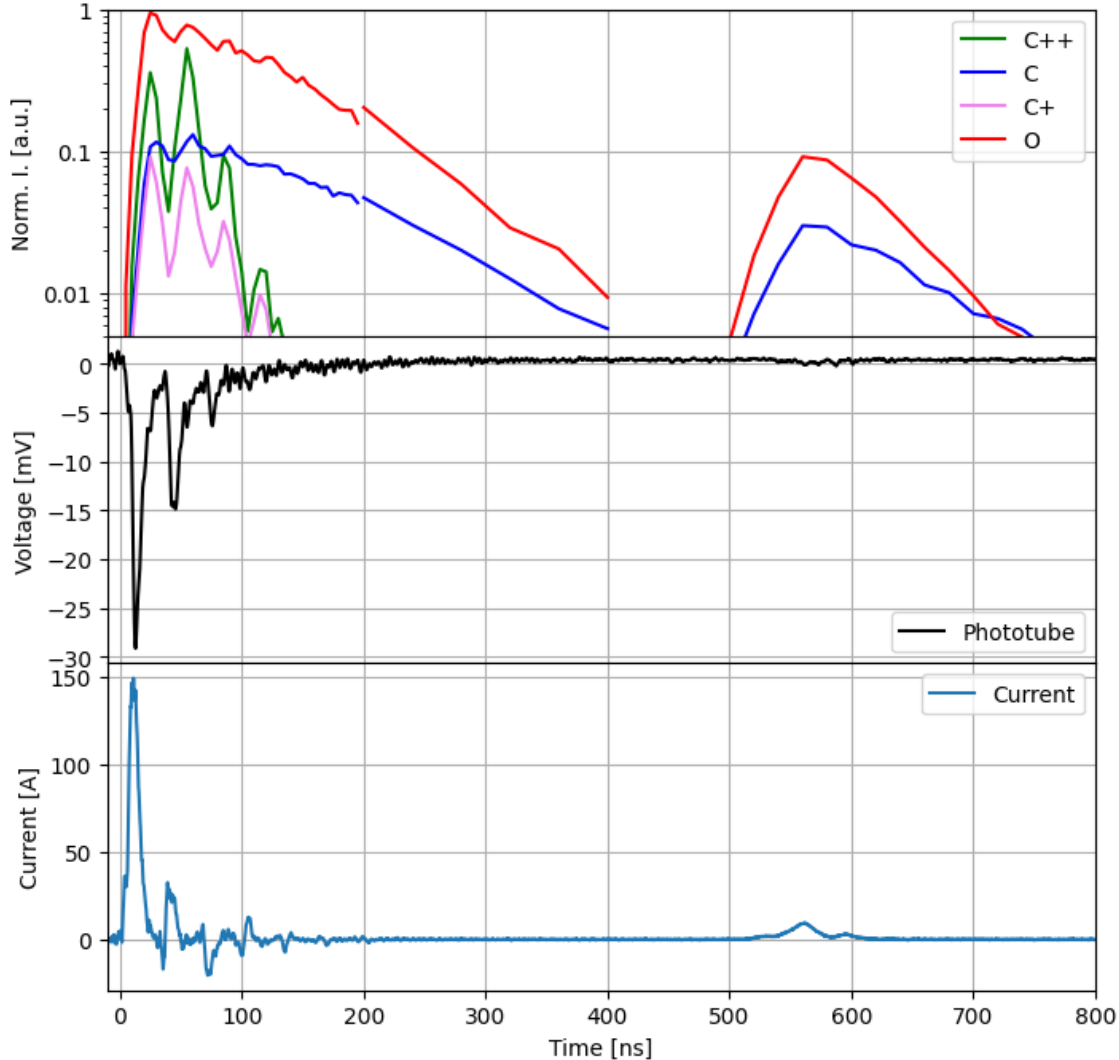


Figure 5.8: Time evolution of atomic lines at the cathode (the y-axis is normalized to the maximum signal and expressed in logarithmic scale): C at 247.85 nm, C^+ at 250.91 nm and 251.21 nm, C^{++} at 229.68 nm and O triplet at 777.19 nm, 777.42 nm, 777.54 nm with the phototube and current signals, the MCP exposure time is set to 5 ns for the time range 0–195 ns, 40 ns for 200–400 ns, and 20 ns for 440–880 ns.

5.4 TR-OES with burst mode and transmission line unmatched in impedance

In the following plots, the IV characteristics, the instantaneous power, and the cumulative energy are reported for the first(Figure 5.9) and second pulse(Figure 5.10) in a two-pulse burst(Figure 3.11).

The presence of multiple current rebounds during the second pulse can be attributed

to the memory effect (see Section 1.7). In this case, the discharge occurs immediately as the line is rapidly terminated with a short circuit, allowing the discharge channel to remain open—or reopen—for an extended duration, resulting in the persistence of current rebounds.

The cumulative energy and power are significantly reduced in the second pulse due to the decrease in voltage required to initiate a breakdown in the second pulse.

The mean energy deposited in the discharge for the first pulse is: 22.8 ± 0.5 mJ, while for the second pulse: 8.1 ± 2.0 mJ.

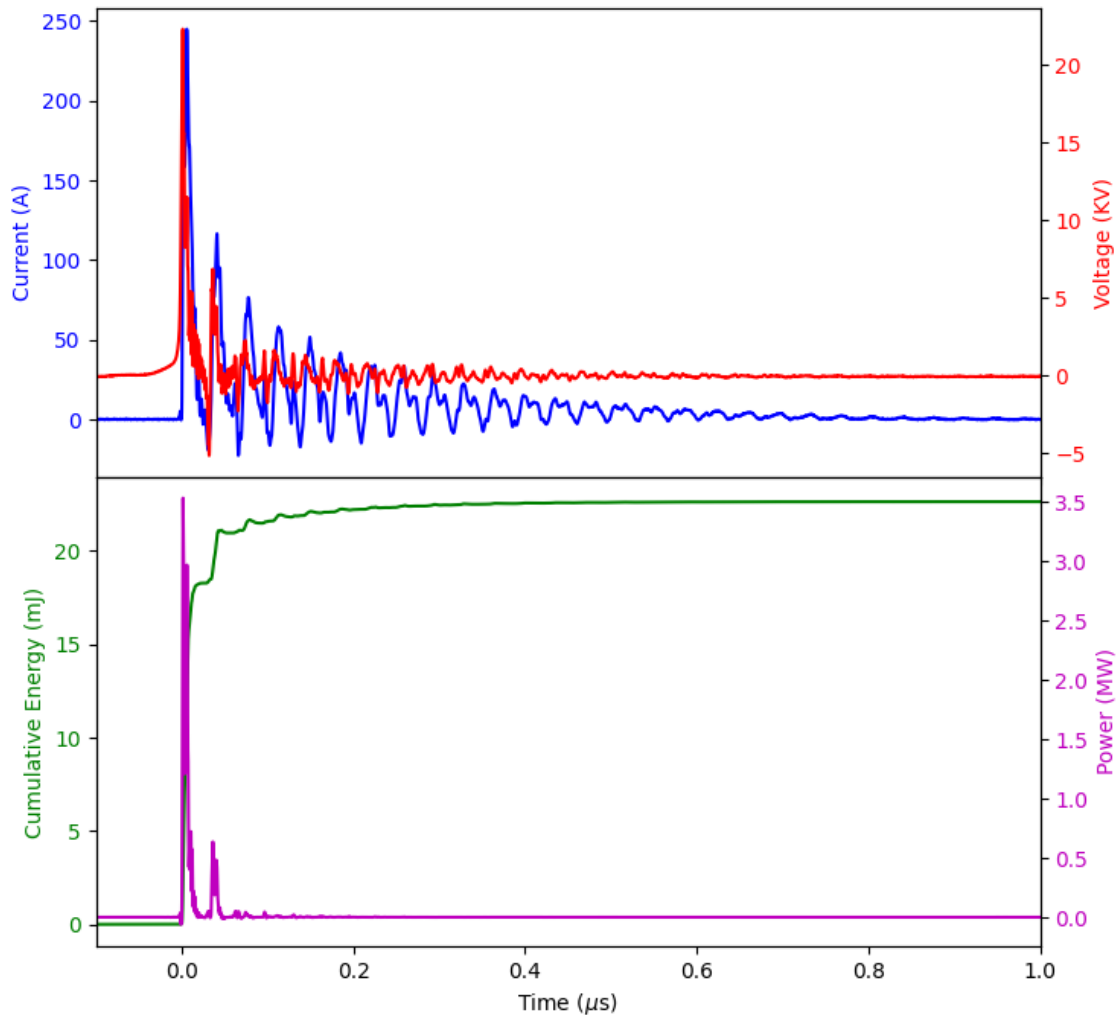


Figure 5.9: IV characteristics in the upper plot and energy and power in the bottom plot for the first pulse in burst mode(200Hz) with the line with unmatched impedance, 2.4 mm electrode gap.

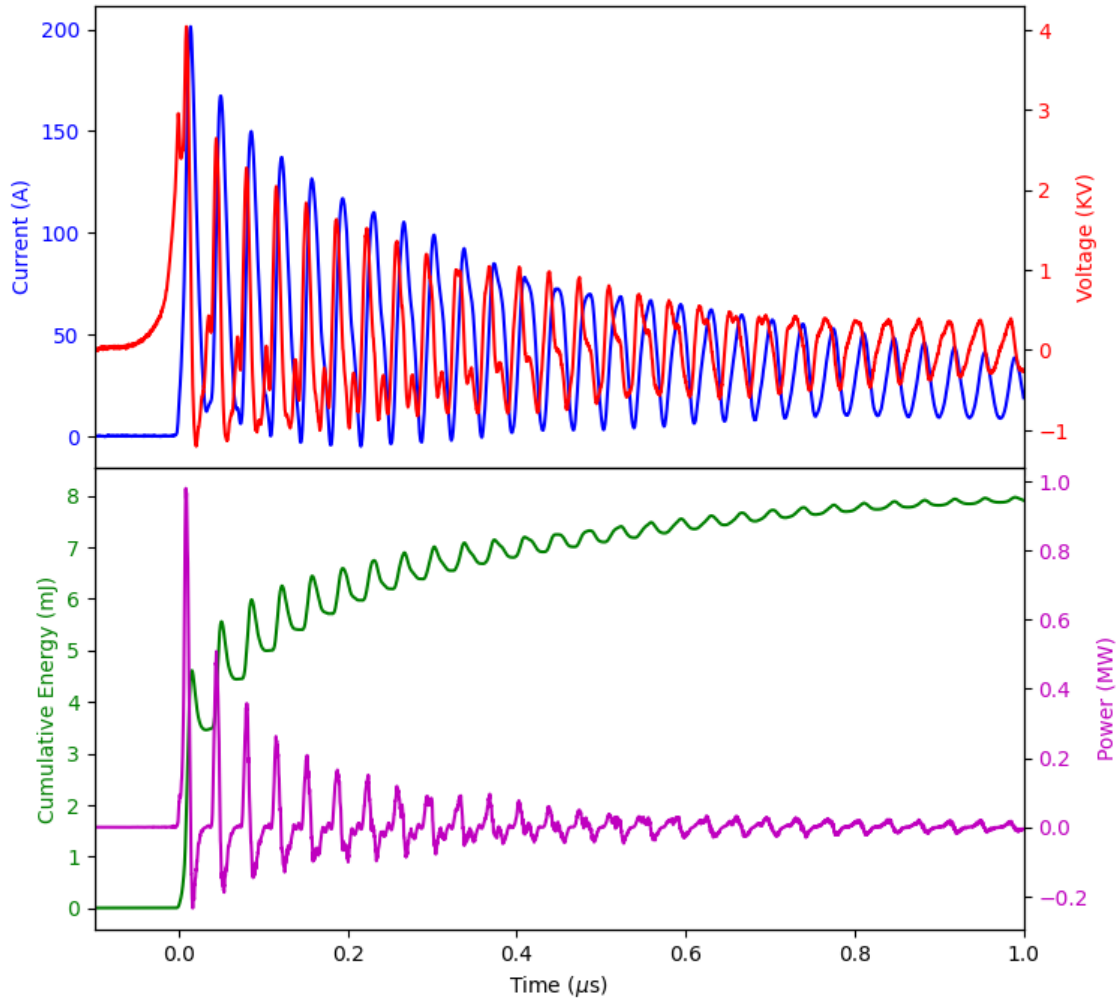


Figure 5.10: IV characteristics in the upper plot and energy and power in the bottom plot for the second pulse in burst mode(200Hz) with the line with unmatched impedance, 2.4 mm electrode gap.

In the following plots, the spectra at 20 ns (Figure 5.11), 100 ns (Figure 5.12), and 200 ns (Figure 5.13) are shown for the second pulse.

It can be observed that at both 100 ns and 200 ns, the O⁺ emission is significantly stronger compared to the other emission profiles. This is likely due to the presence of current rebounds, which continue to ionize the gas over time, resulting in sustained ionization even after 200 ns.

Additionally, the emission features in the UV region (200-350 nm) are absent, which is likely due to the sputtering of both tungsten from the electrodes and carbon from the CO₂ gas, which contaminates the reactor window. Notably, this measurement was conducted as the final one, without the usual cleaning of the reactor window. Future measurements should be performed with a cleaned window to avoid this contamination.

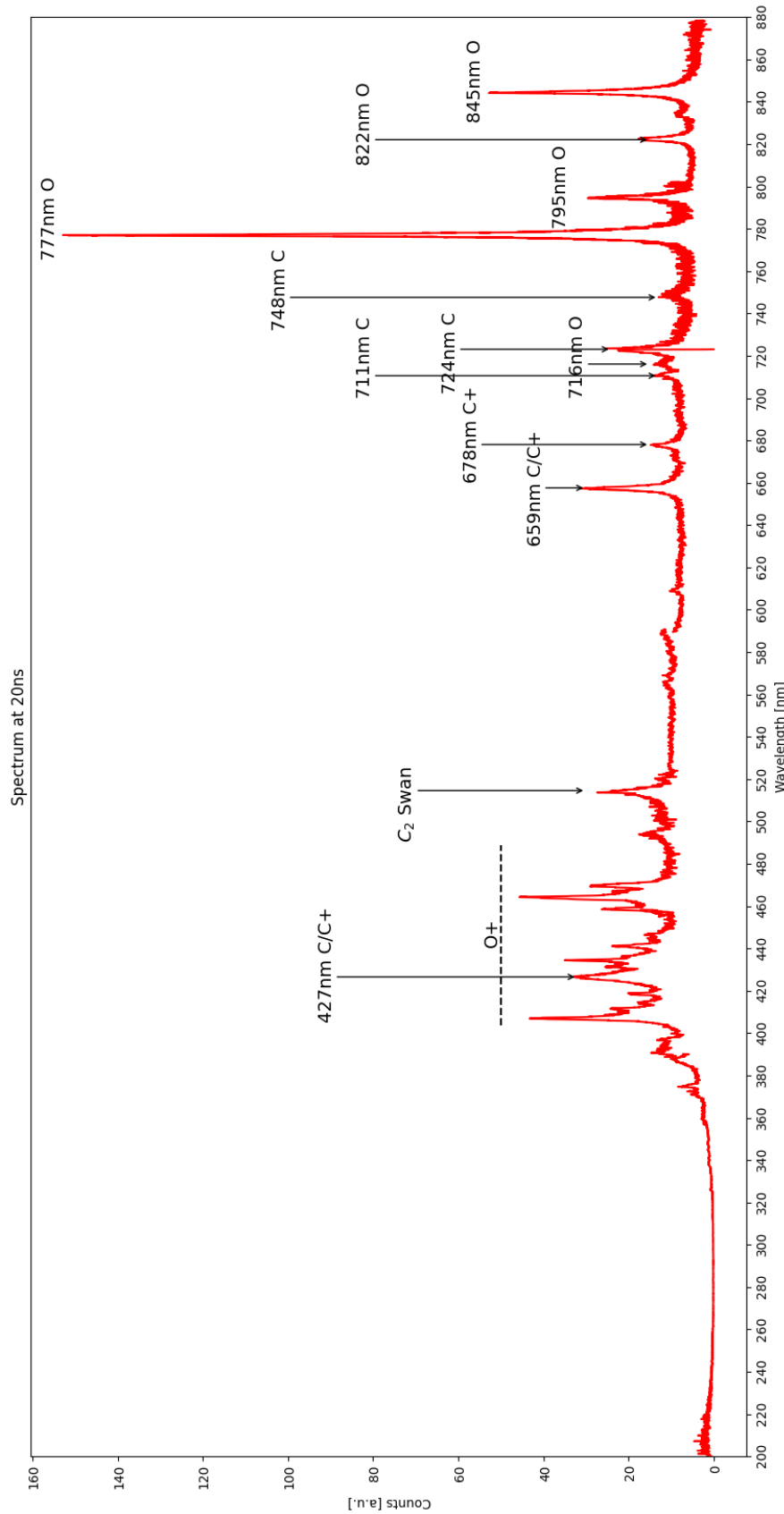


Figure 5.11: Spectrum 20ns after the start of the discharge for 200Hz unmatched in impedance, 2.4mm electrodes gap, second pulse of burst mode, the MCP exposure time is set to 5 ns.

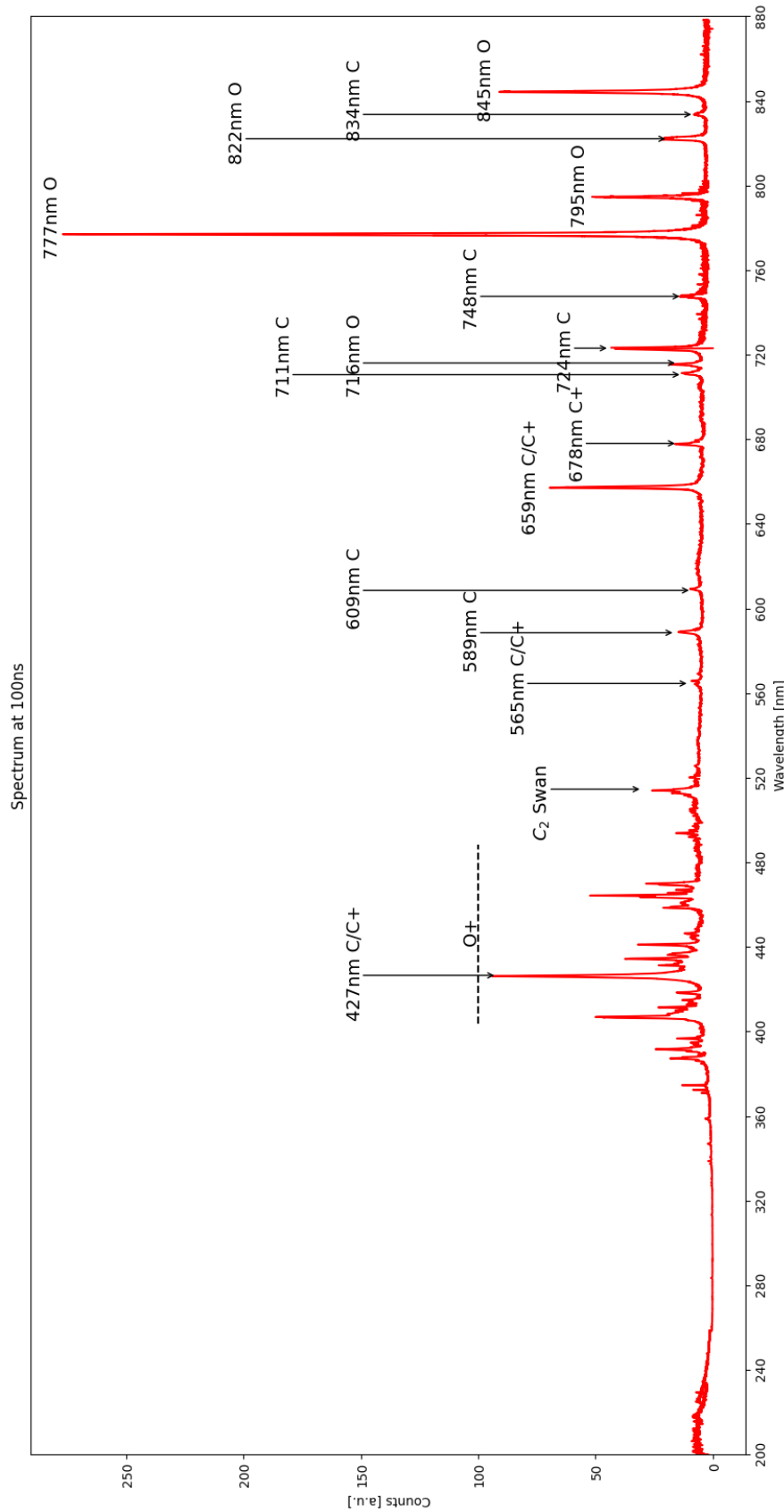


Figure 5.12: Spectrum 100ns after the start of the discharge for 200Hz unmatched in impedance, 2.4mm electrodes gap, second pulse of burst mode, the MCP exposure time is set to 5 ns.

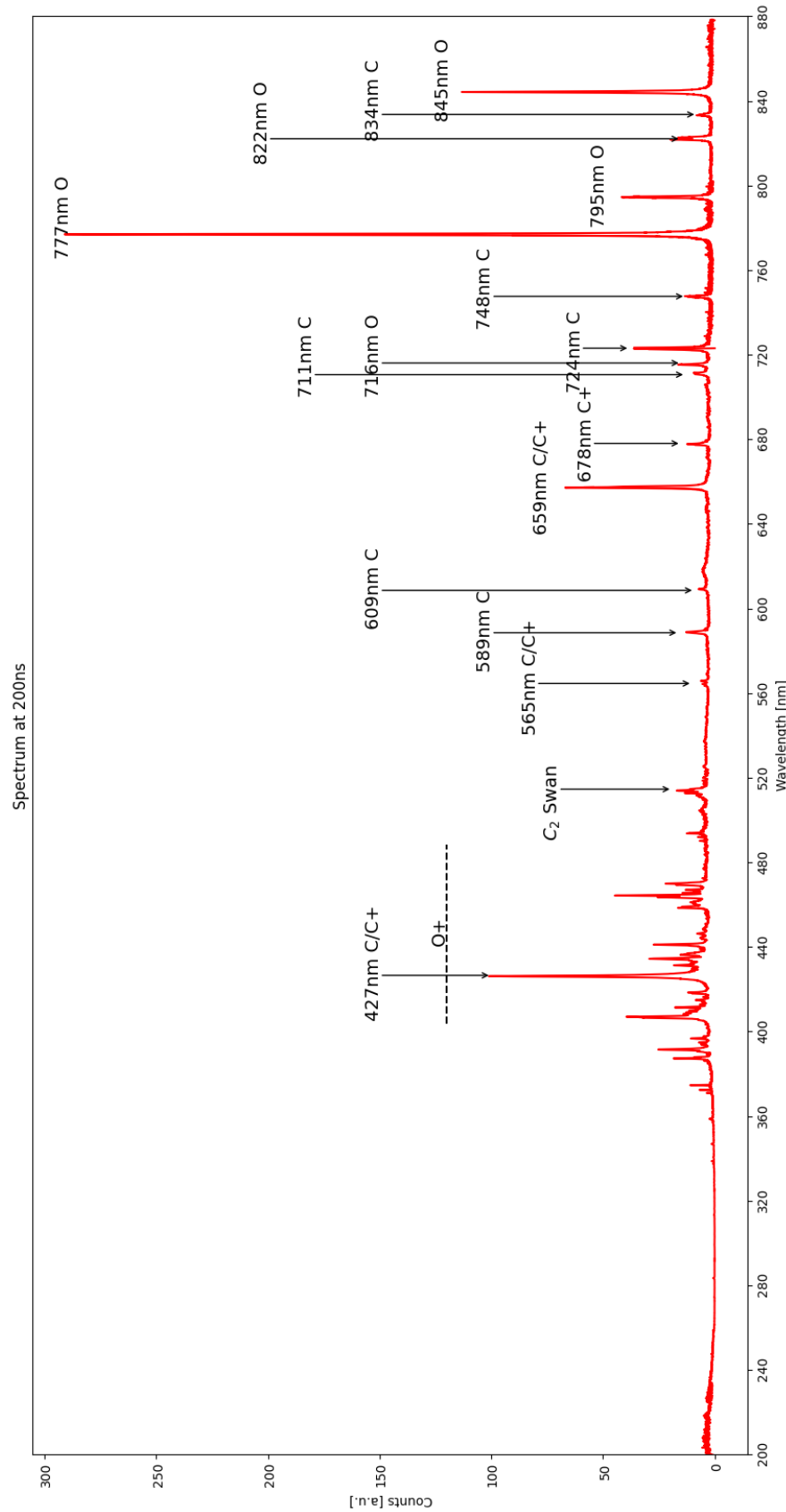


Figure 5.13: Spectrum 200ns after the start of the discharge for 200Hz unmatched in impedance, 2.4mm electrodes gap, second pulse of burst mode, the MCP exposure time is set to 5 ns.

5.5 TR-OES with burst mode and transmission line matched in impedance

Finally, the line is impedance-matched using a resistor placed downstream of the cathode. The discharge is operated in burst mode.

In the following plots, the IV characteristics, instantaneous power, and cumulative energy (Figures 5.14, 5.15) are shown as a function of time. It can be observed that the current rebounds are significantly reduced in the second pulse of the burst mode. Additionally, the power and cumulative energy decrease in the second pulse, likely due to the memory effect mentioned in section 1.7, which reduces the voltage required to initiate a breakdown. The mean energy deposited in the discharge for the first pulse is 10.7 ± 0.3 mJ, while for the second pulse, it is 3.7 ± 0.2 mJ. This reduction in deposited energy for both pulses is primarily attributed to energy dissipation via the Joule effect in the matching resistance.

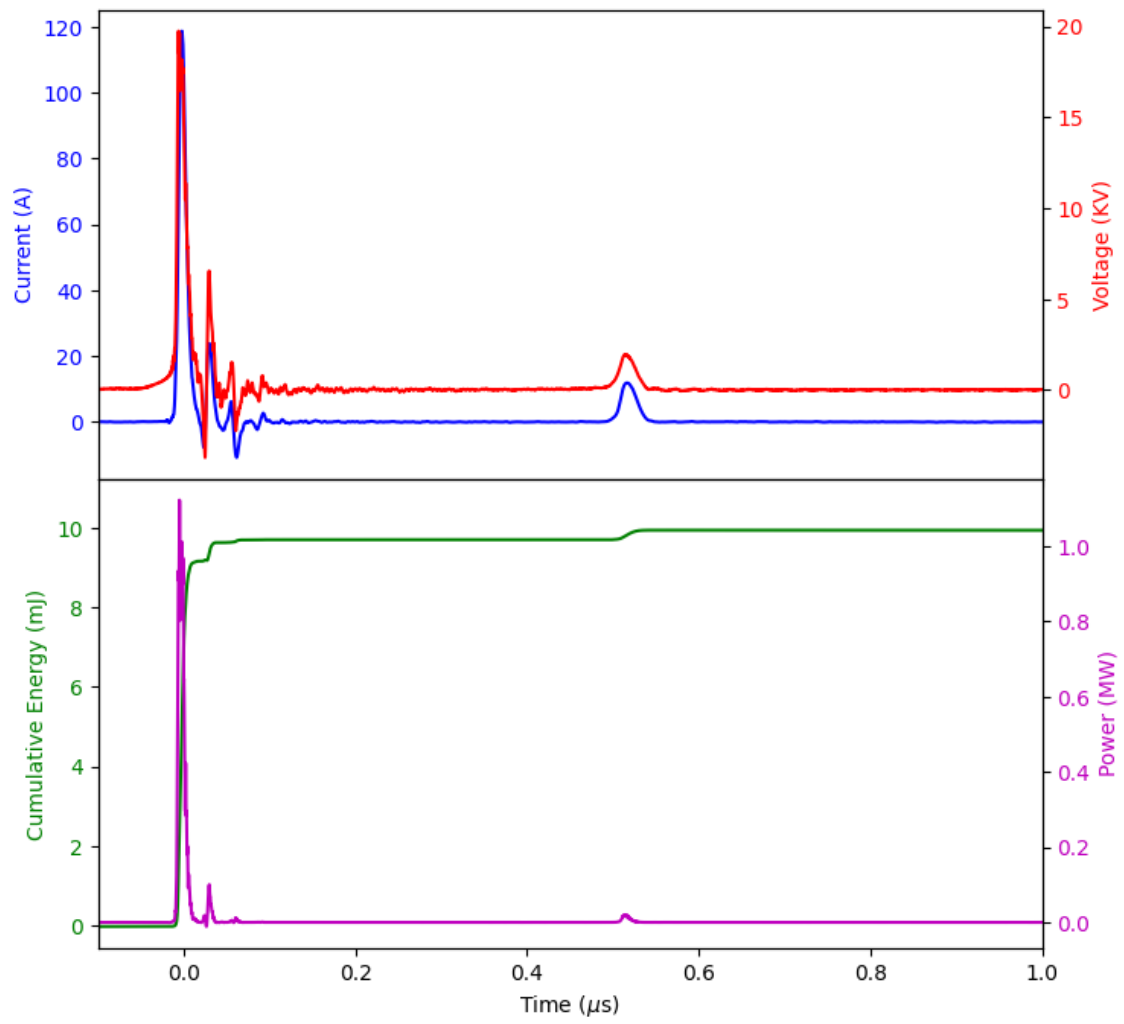


Figure 5.14: IV characteristics in the upper plot and energy and power in the bottom plot for the first pulse in burst mode(200Hz) with the line with matched impedance, 2.4 mm electrode gap.

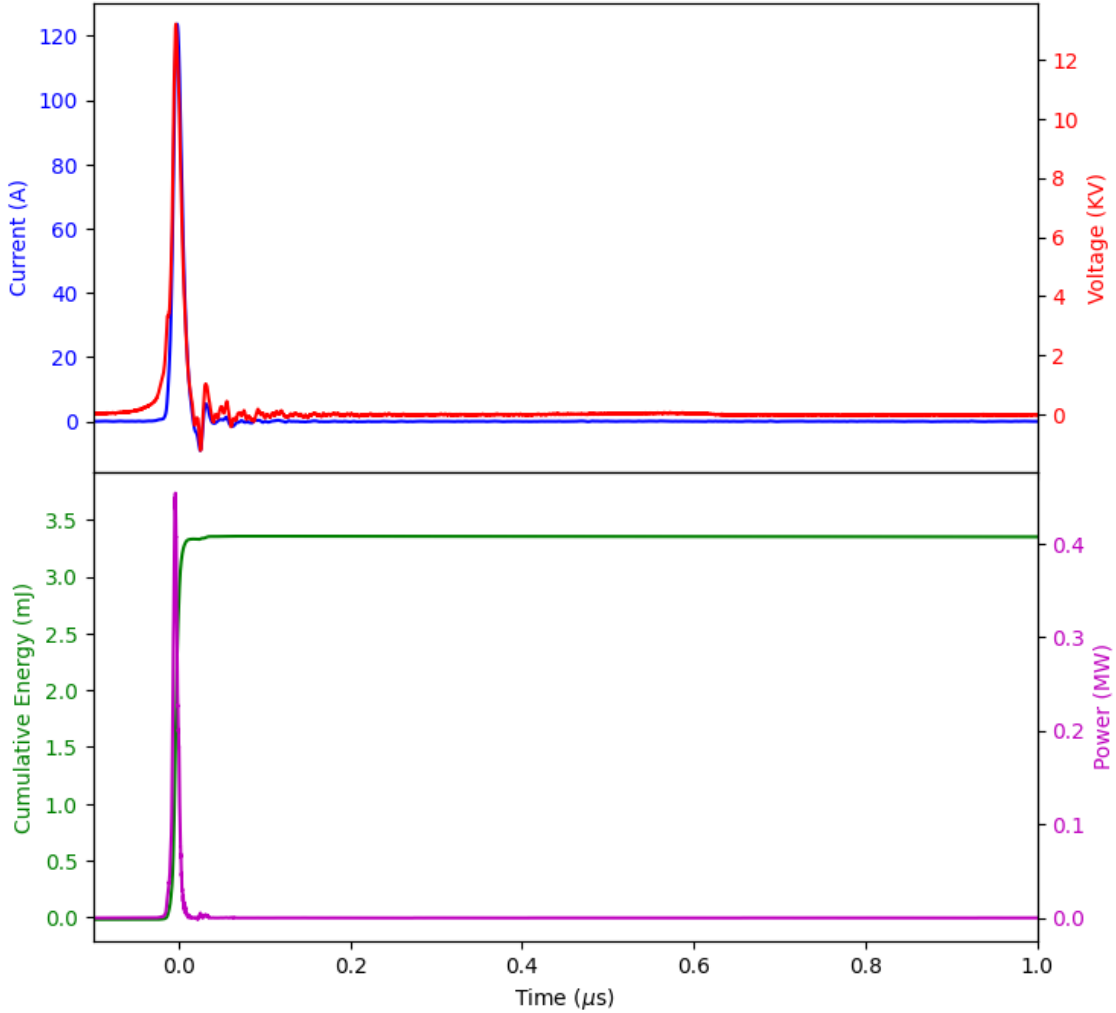


Figure 5.15: IV characteristics in the upper plot and energy and power in the bottom plot for the second pulse in burst mode(200Hz) with the line with matched impedance, 2.4 mm electrode gap.

The emission profile spectra are plotted for the second and first pulses at 20 ns (Figures 5.18, 5.16), 0 ns for the molecules(Figures 5.19, 5.17), 100 ns(Figures 5.22, 5.21), and 200 ns(Figures 5.24, 5.23), with the pulses delivered at 200 Hz in burst mode and separated by an interval of $18 \mu\text{s}$. It is evident that the counts from the second pulse are approximately an order of magnitude higher than those from the first pulse (for the ions), indicating that some level of ionization remains in the gas.

An interesting comparison can be made between the molecular bands (Figure 5.20), where it is evident that the discharge develops in a gas mixture of CO_2 that is already partially dissociated. Specifically, we observe CO emissions, which are absent in the first pulse emission, clearly marking the conversion from CO_2 to CO.

It is also observed that in the second pulse, the intensity of carbon emission slightly exceeds

that of oxygen at both 100 ns and 200 ns, implying a more consistent dissociation process during the second pulse (Figures 5.22, 5.22, 5.23, 5.24). Additionally, the disappearance of molecular bands at these time intervals suggests that three-body recombination of carbon monoxide with atomic oxygen has likely occurred, as described by the reaction:

$$\text{CO} + O + M \rightarrow \text{CO}_2 + M.$$

Furthermore, it is interesting to compare the second pulse of the burst mode in the impedance-matched configuration with the data reported by Ceppelli et al. [1] (Figure 13a), which corresponds to the second pulse of a burst mode operation in an unmatched line impedance configuration with a different reactor. The main difference lies in the presence of CO emission features at the start of the discharge in the impedance-matched spectrum, which are weak or absent in the unmatched spectrum.

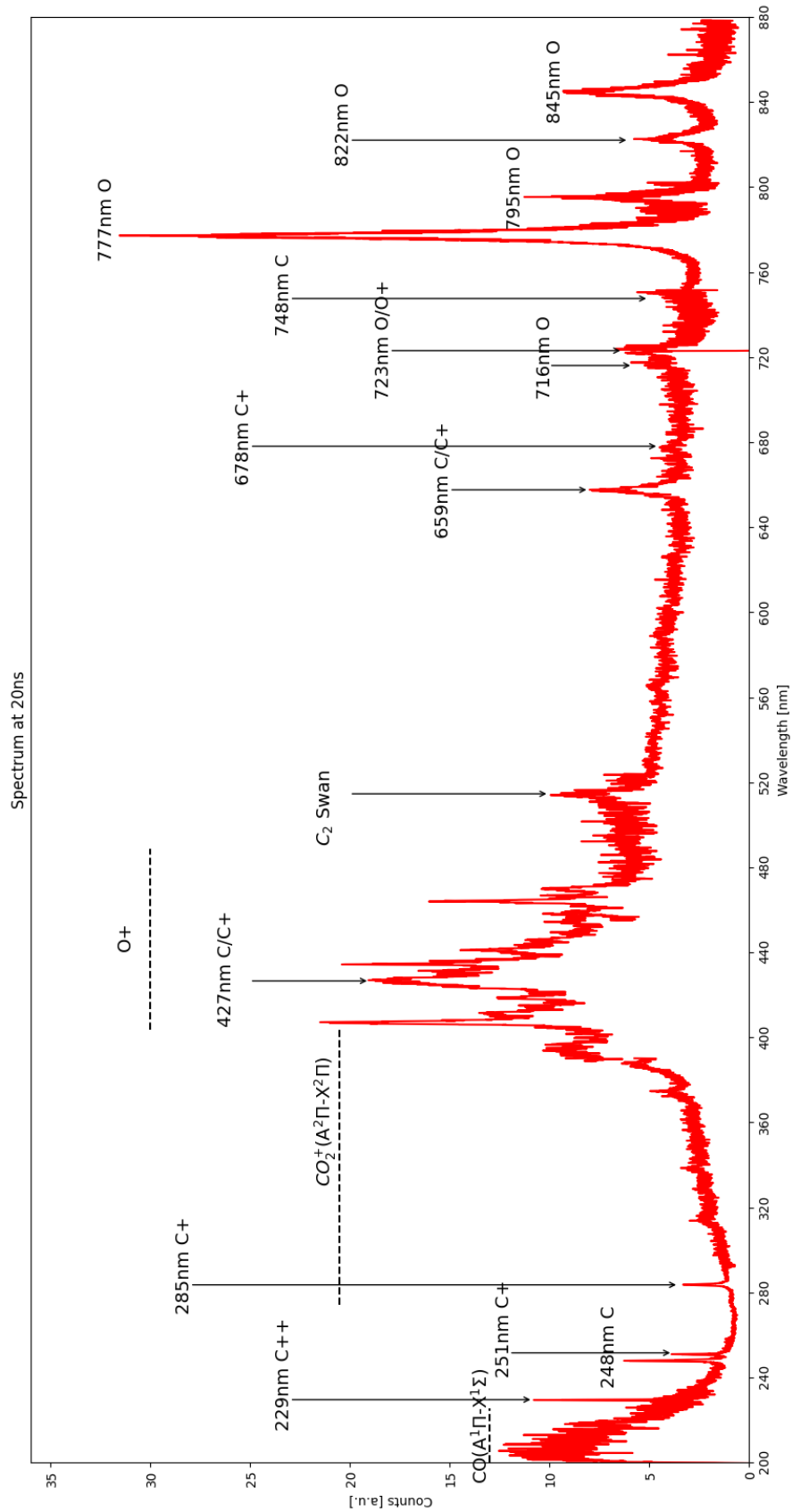


Figure 5.16: Spectrum 20ns after the start of the discharge for 200Hz matched in impedance, 2.4mm electrodes gap, first pulse of burst mode, the MCP exposure time is set to 5 ns.

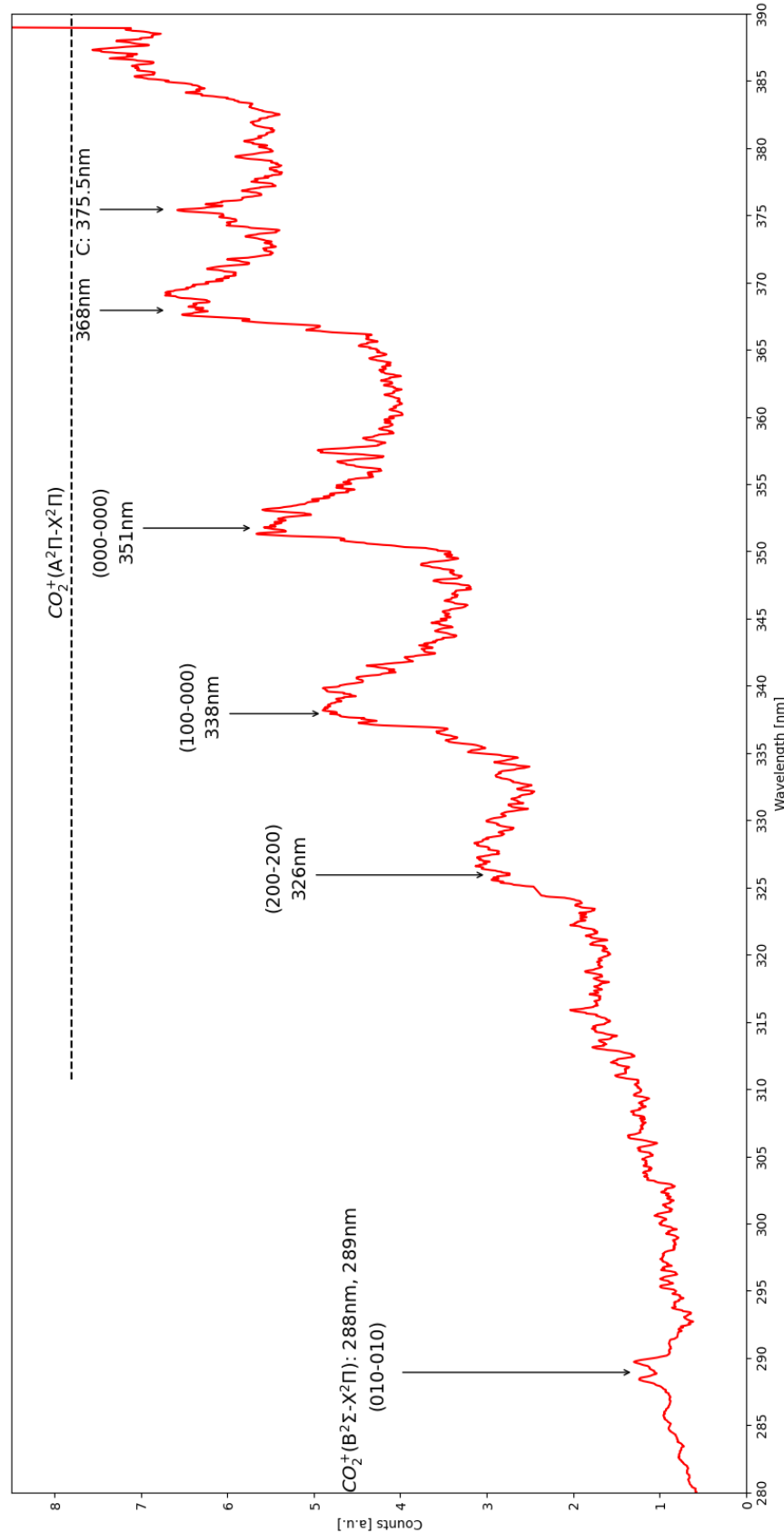


Figure 5.17: Molecular bands at 0ns after the start of the discharge for 200Hz matched in impedance, 2.4mm electrodes gap, the first pulse of burst mode, the MCP exposure time is set to 5 ns.

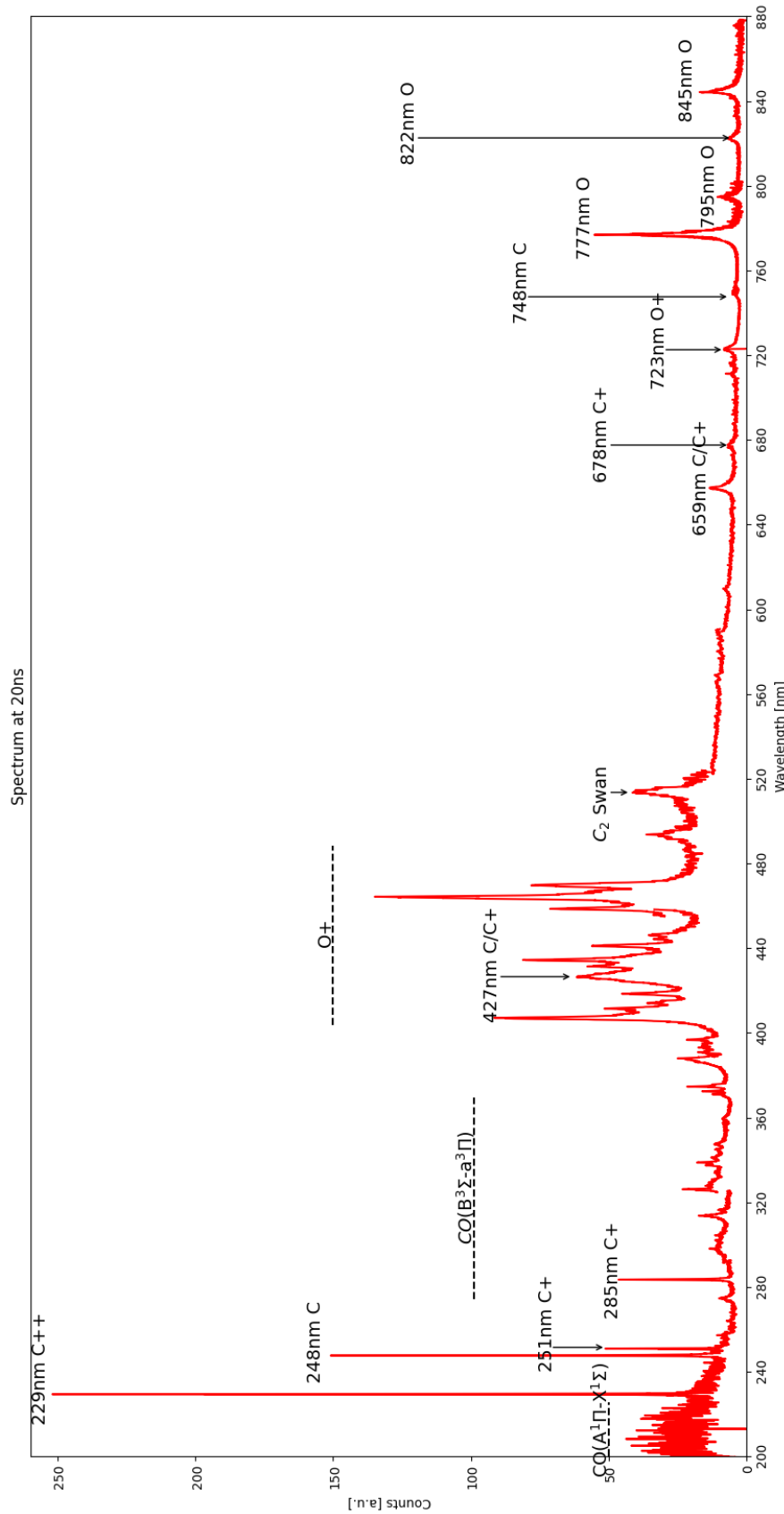


Figure 5.18: Spectrum 20ns after the start of the discharge for 200Hz matched in impedance, 2.4mm electrodes gap, second pulse of burst mode, the MCP exposure time is set to 5 ns

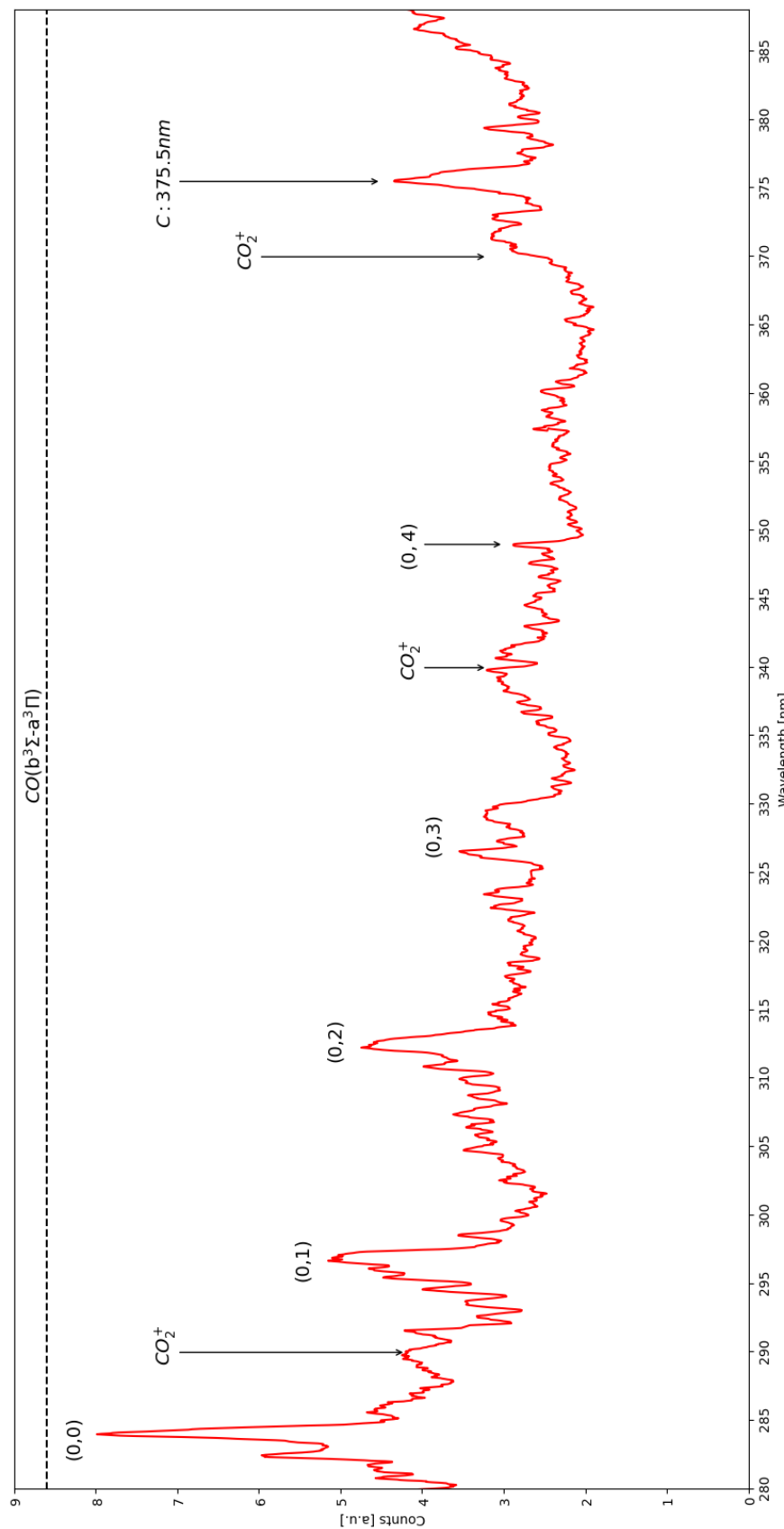


Figure 5.19: Molecular bands at 0ns after the start of the discharge for 200Hz matched in impedance, 2.4mm electrodes gap, the second pulse of burst mode, the MCP exposure time is set to 5 ns.

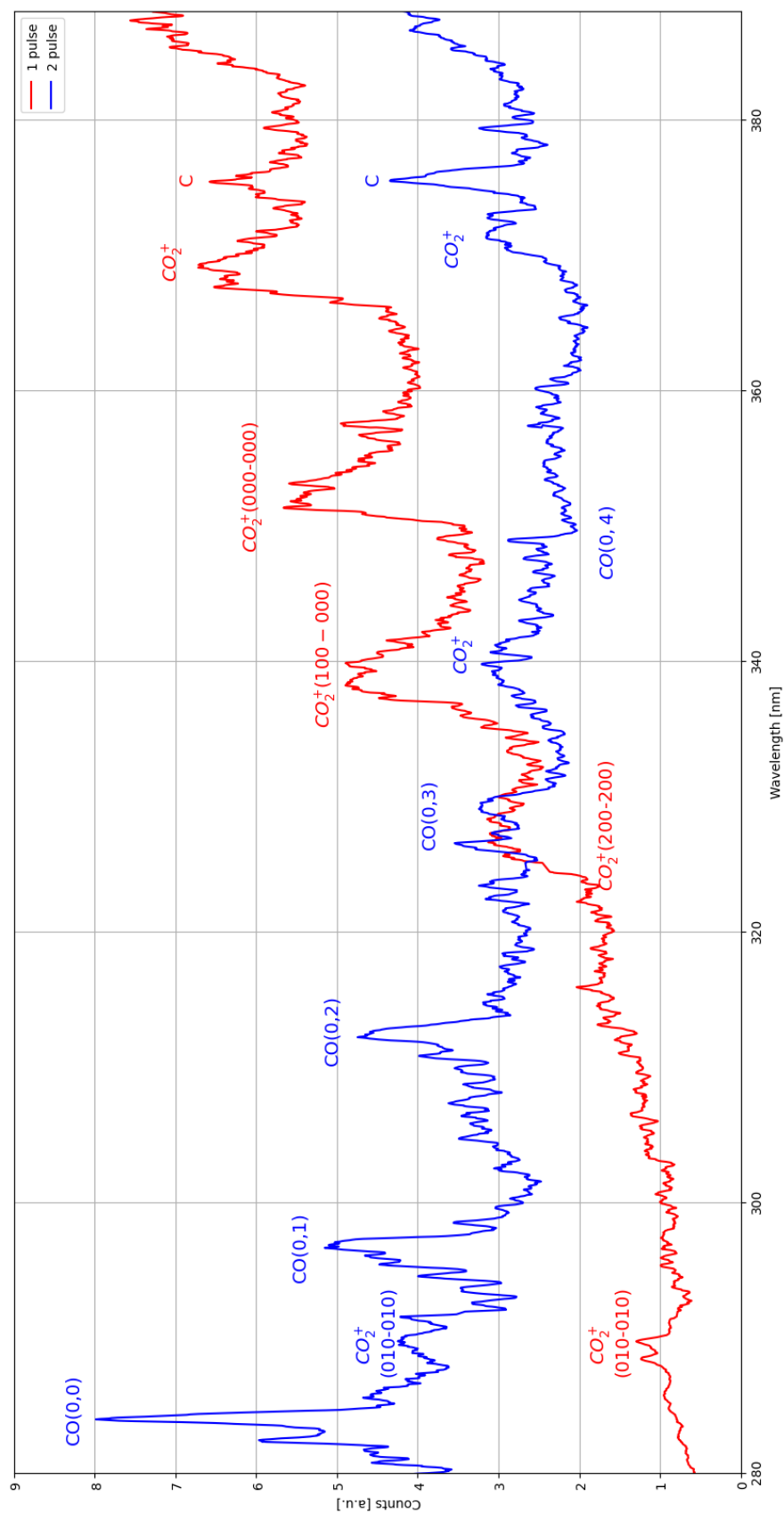


Figure 5.20: Comparison of molecular emissions between the two pulses

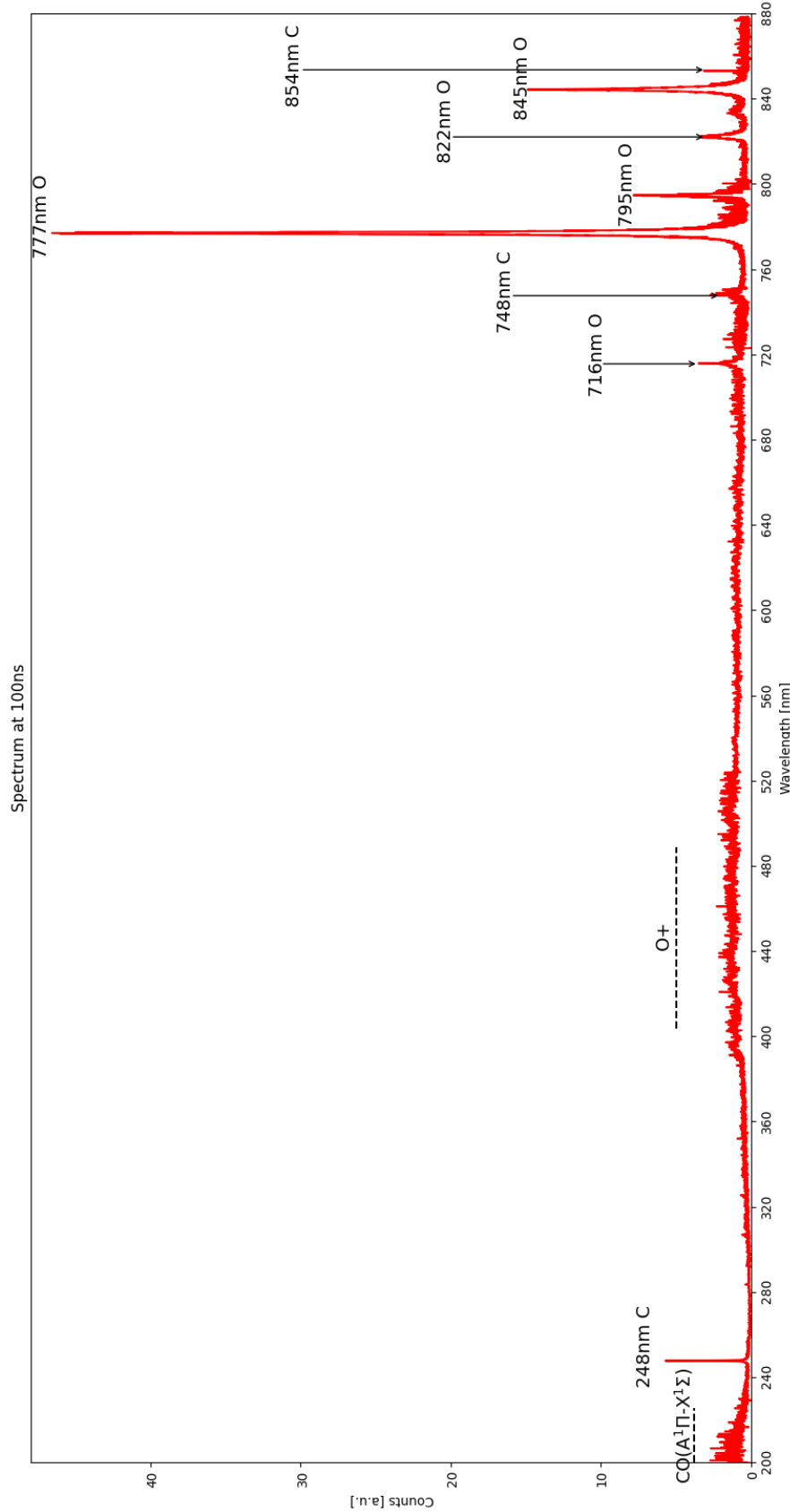


Figure 5.21: Spectrum 100ns after the start of the discharge for 200Hz matched in impedance, 2.4mm electrodes gap, first pulse of burst mode, the MCP exposure time is set to 5 ns.

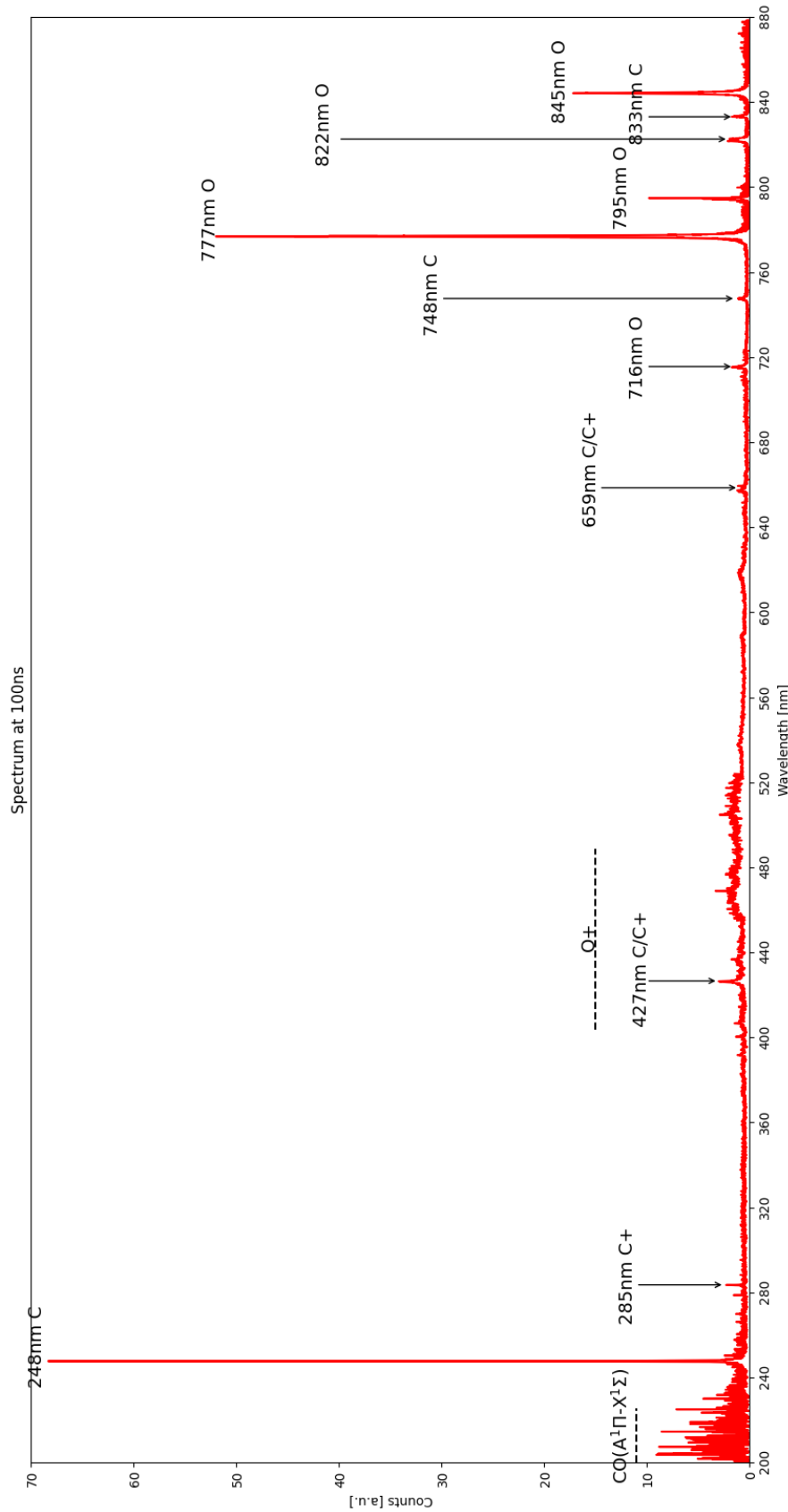


Figure 5.22: Spectrum 100ns after the start of the discharge for 200Hz matched in impedance, 2.4mm electrodes gap, second pulse of burst mode, the MCP exposure time is set to 5 ns.

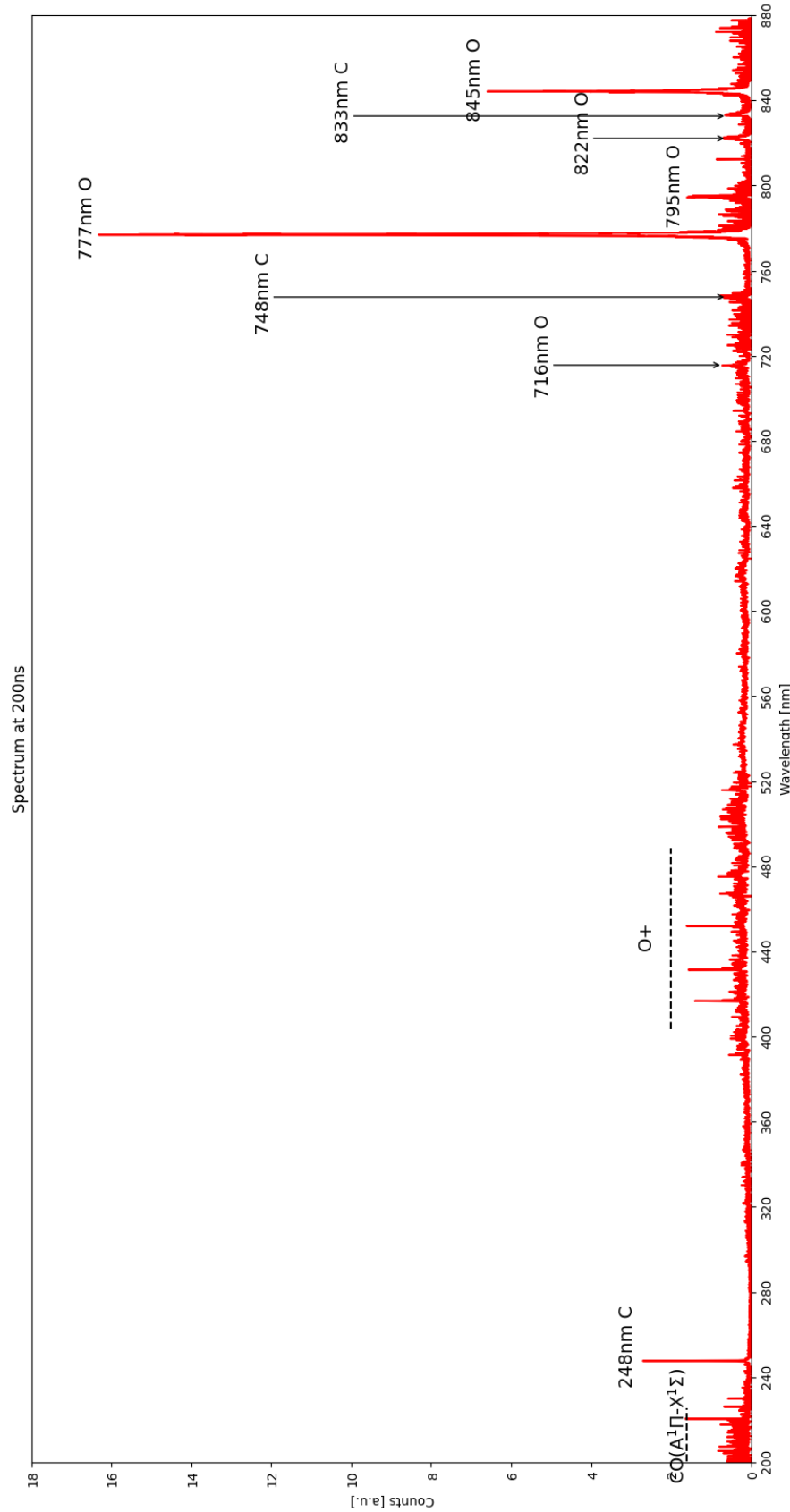


Figure 5.23: Spectrum 200ns after the start of the discharge for 200Hz matched in impedance, 2.4mm electrodes gap, first pulse of burst mode, the MCP exposure time is set to 5 ns.

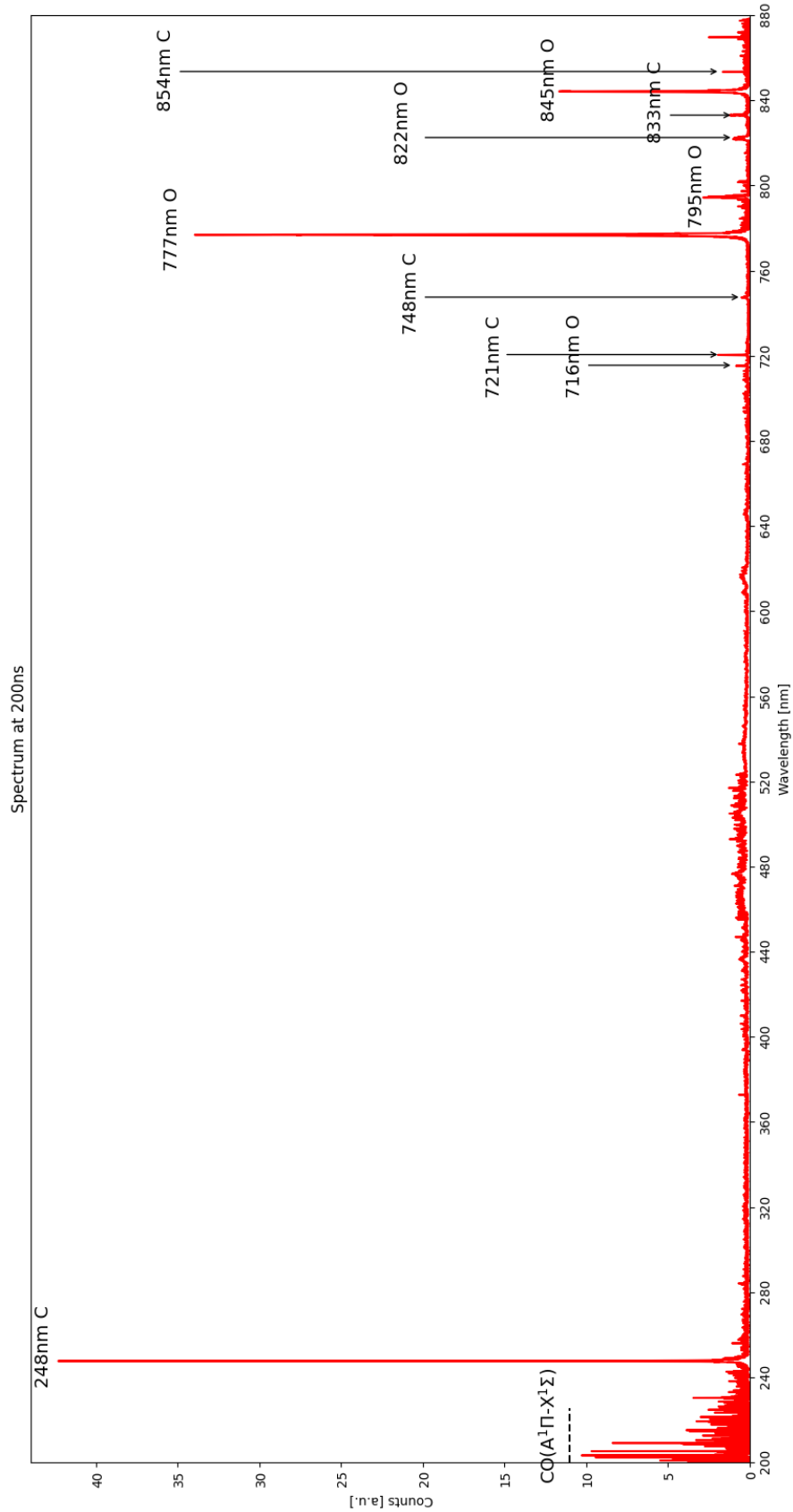


Figure 5.24: Spectrum 200ns after the start of the discharge for 200Hz matched in impedance, 2.4mm electrodes gap, second pulse of burst mode, the MCP exposure time is set to 5 ns.

From Figure 5.25 and 5.26, it is evident that the second pulse exhibits a single emission profile, whereas the first pulse presents three main signal reflections corresponding to current rebounds, confirming the effectiveness of the impedance matching. Additionally, the C⁺⁺ emission in the second pulse remains dominant up to 30 ns, indicating a high degree of ionization in the gas during the initial stage of the discharge. After 30 ns, the neutral atomic species exhibit a significantly slower exponential decay compared to the ionic species, suggesting a longer lifetime for neutral species in the plasma.

In the first pulse, atomic neutral oxygen is the dominant emission, maintaining nearly constant intensity during the first two current rebounds before beginning to decay after the third rebound at 75 ns. Notably, in both pulses, the oxygen emission begins approximately 5 ns earlier than the others. Notably, in both pulses, the oxygen emission begins approximately 5 ns earlier than the others. This can be attributed, probably, to O being produced through a single-stage dissociation of CO₂ via electron impact: $e^- + CO_2 \rightarrow CO + O + e^-$, whereas C requires an additional dissociation step from CO, leading to a delayed emission. Remarkably, the time resolution is 5 ns, so further studies have to be done.

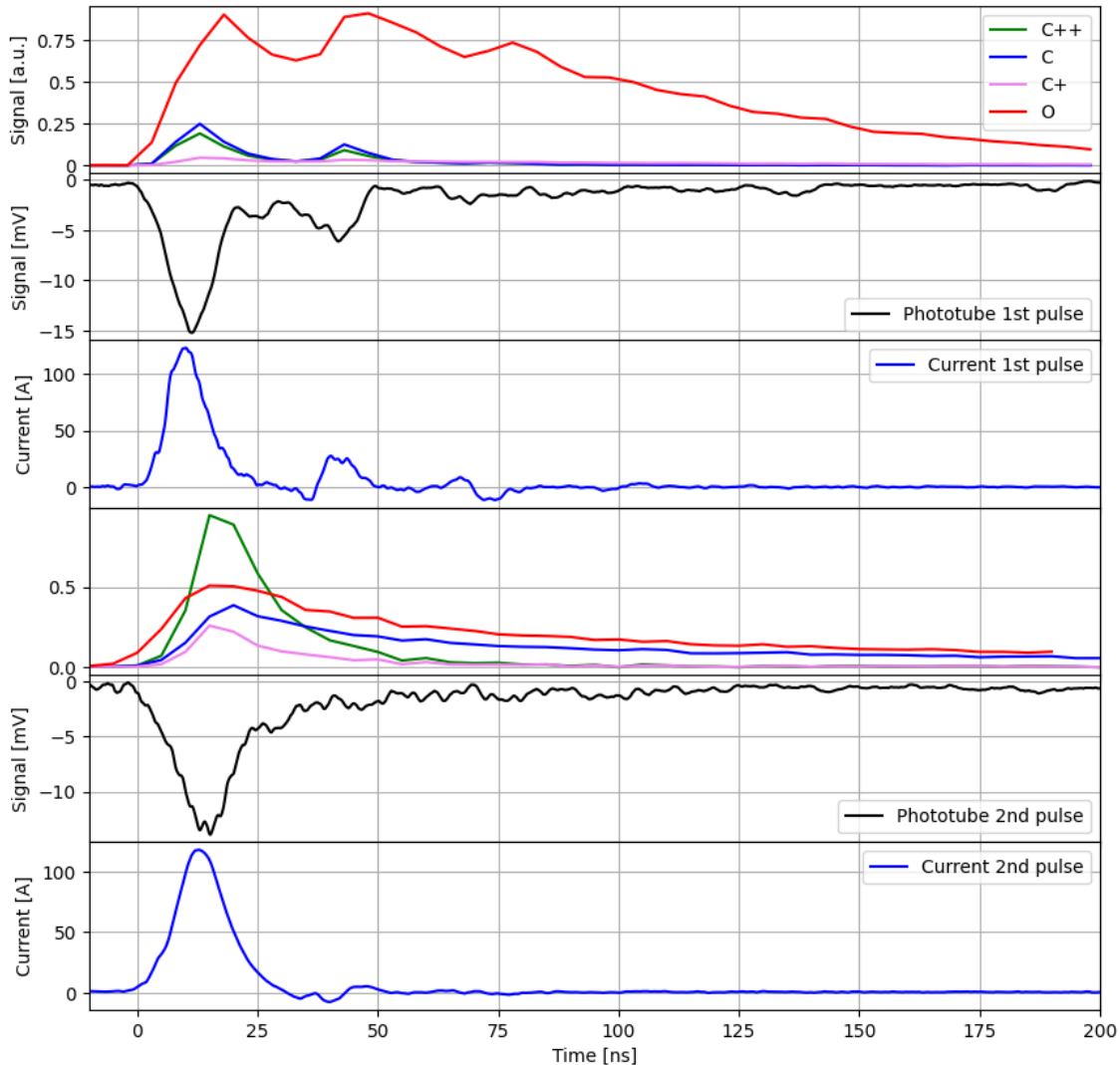


Figure 5.25: Time evolution of atomic lines for the first and second pulse in burst mode (the y-axis is normalized to the maximum signal): C at 247.85 nm, C^+ at 250.91 nm and 251.21 nm, C^{++} at 229.68 nm and O triplet at 777.19 nm, 777.42 nm, 777.54 nm with the phototube and current signals, the MCP exposure time and time resolution is 5 ns.

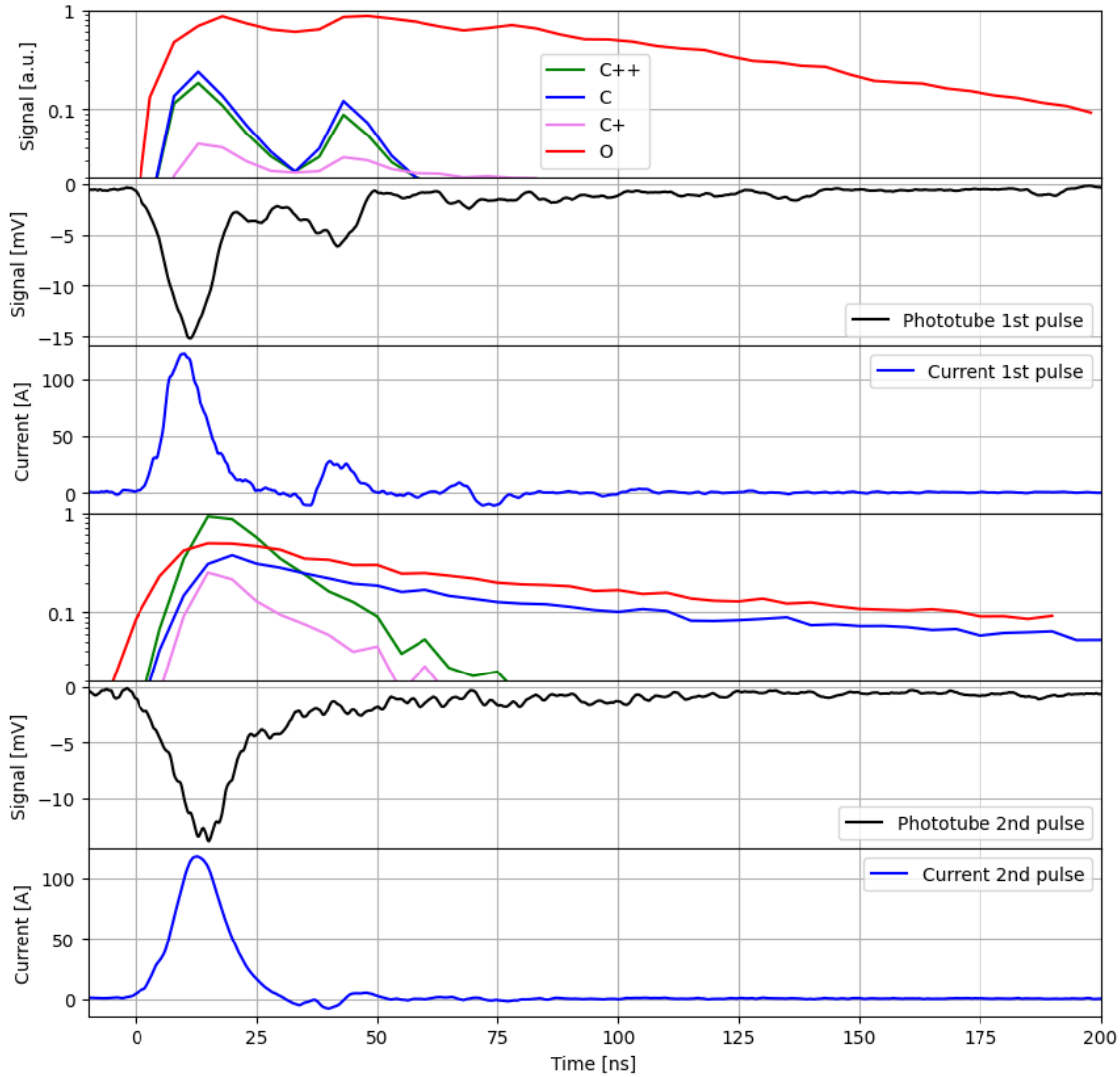


Figure 5.26: Time evolution of atomic lines for the first and second pulse in burst mode (the y-axis is normalized to the maximum signal and expressed in logarithmic scale): C at 247.85 nm, C^+ at 250.91 nm and 251.21 nm, C^{++} at 229.68 nm and O triplet at 777.19 nm, 777.42 nm, 777.54 nm with the phototube and current signals, the MCP exposure time and time resolution is 5 ns.

Chapter 6

Conclusions and future perspectives

The objective of this thesis was to investigate the temporal evolution of optical emission in a discharge for CO₂ conversion.

A new experimental setup was developed, specifically designed to eliminate unwanted re-triggers and reflections on the transmission line. Initially, the results of Ceppelli et al. were successfully reproduced under continuous operation with an electrode gap of 5.5 mm, confirming the dominance of molecular bands (CO 3PS, CO₂⁺ FDBS, and $\lambda\lambda$) and atomic ions in the early stages of the discharge (20 ns), while atomic lines prevail at later times(100 ns and 200 ns). Additionally, the emissions of O⁺, C, and C⁺ in the 400–500 nm range were identified, as in [55].

Furthermore, a detailed analysis of the optical emission at the cathode revealed a distinct temporal evolution of atomic species and ions. Specifically, the peak integrals of C, C⁺, C⁺⁺, and O were found to coincide with the first current peak, unlike in the center of the electrode gap, where they appear in later rebounds(Figure 5.8). This suggests that the formation of atomic species is more intense at the cathode during the breakdown phase. This indicates that the dissociation process in the center of the discharge likely requires a longer timescale and multiple discharge events to develop fully.

Moreover, the feasibility of mitigating bounces and retriggers caused by impedance mismatching in the transmission line connecting the reactor to the power supply was examined. In a configuration with a 2.4 mm discharge gap and an effective matching resistance of $80 \pm 3 \Omega$, reflections in the second pulse of a two-pulse burst were successfully sup-

pressed, as evidenced by the single emission profile of the second pulse (Figure 5.15). Notably, in the second pulse of the burst mode, dissociation and ionization is significantly more pronounced, as indicated by the presence of CO emission features (Figure 5.20) and the dominance of C⁺⁺ emission up to 25 ns (Figure 5.25).

This suppression in the emission rebounds enabled a clearer distinction in optical emission profiles at different time delays and revealed distinct temporal trends. The ability to effectively suppress reflections opens new opportunities for studying the time-resolved evolution of CO₂ dissociation on a 100 ns timescale within a single discharge event.

Future work will focus on the systematic investigation of the temporal evolution of other relevant emissions, such as O⁺ in the 400–500 nm range. Additionally, future experiments will focus on determining the electron density through Stark broadening, evaluating the electron temperature from the intensity of atomic and ionic emission lines, and estimating the gas temperature by introducing N₂ and analyzing its second positive system bands. Furthermore, CET-LIF measurements will be conducted to investigate the temporal evolution of CO₂ dissociation following the discharge pulse. These studies will provide further insights into the excitation and relaxation dynamics of species in the plasma.

Chapter 7

Appendix

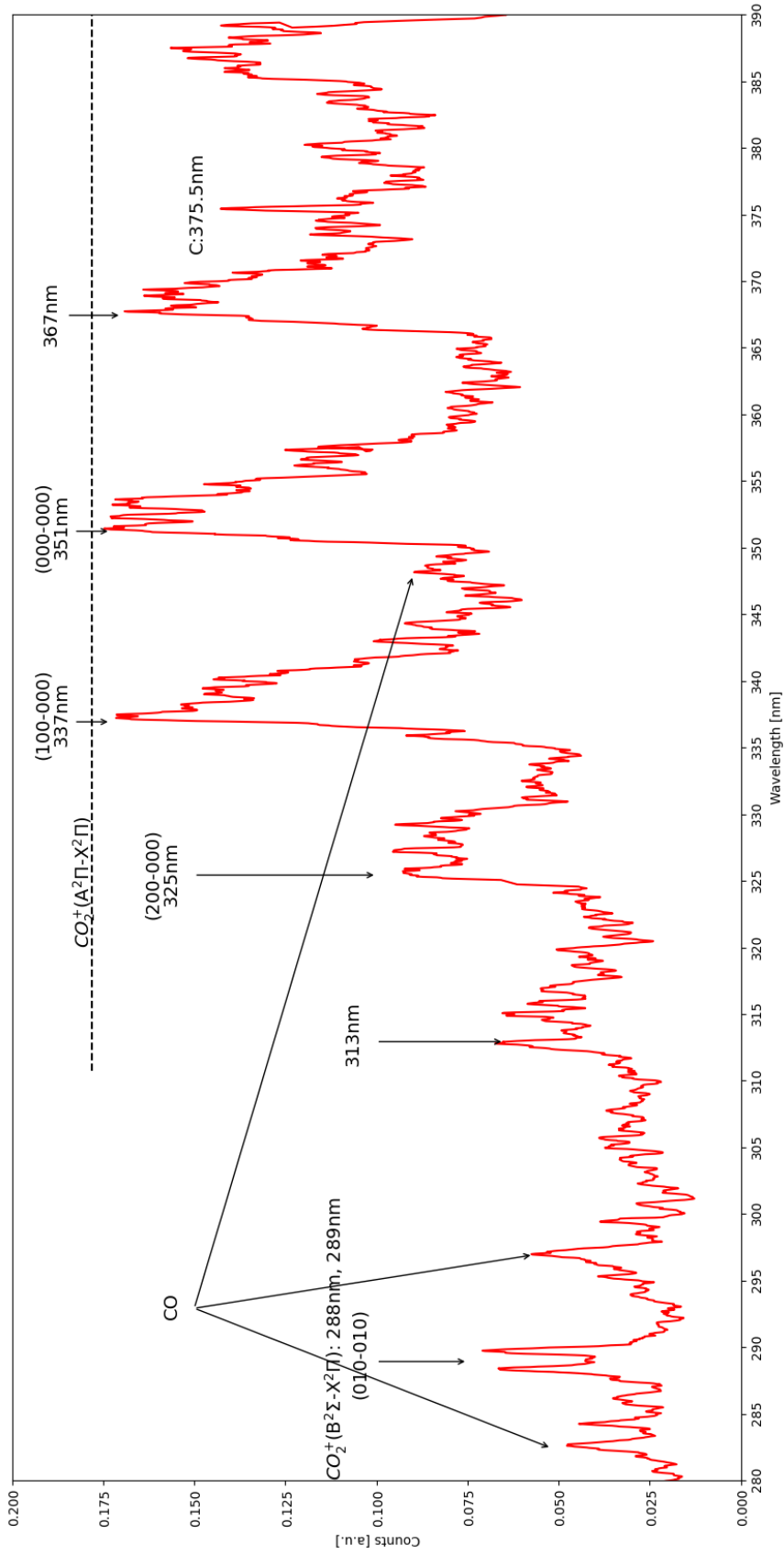


Figure 7.1: Molecular bands at 1 ns after the start of the discharge for 200Hz mismatched in impedance, 5.5mm electrodes gap at the cathode, the MCP exposure time is set to 5 ns

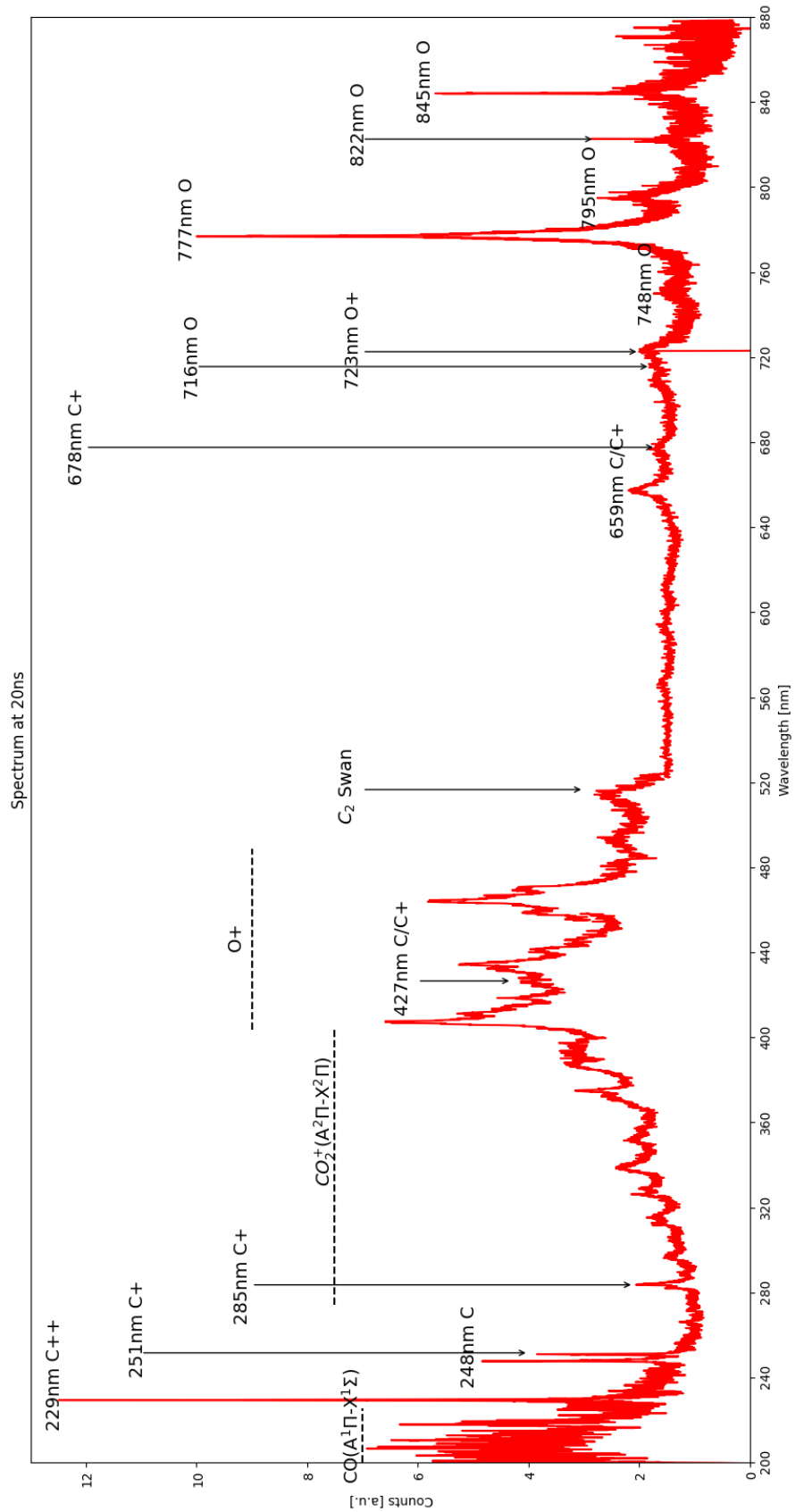


Figure 7.2: Spectrum 20ns after the start of the discharge for 200Hz unmatched in impedance, 5.5mm electrodes gap at the cathode, the MCP exposure time is set to 5 ns.

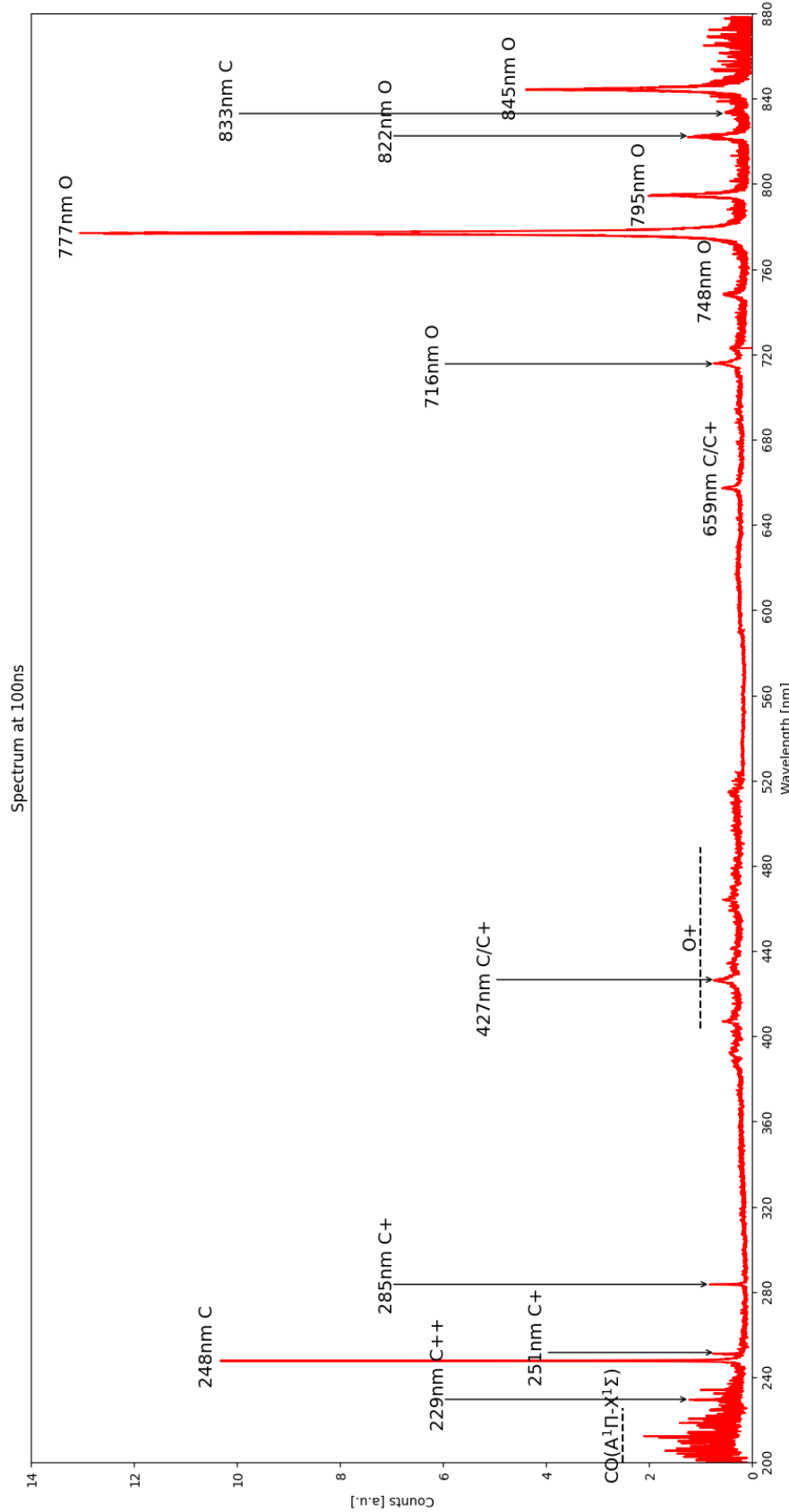


Figure 7.3: Spectrum 100ns after the start of the discharge for 200Hz unmatched in impedance, 5.5mm electrodes gap at the cathode, the MCP exposure time is set to 5 ns.

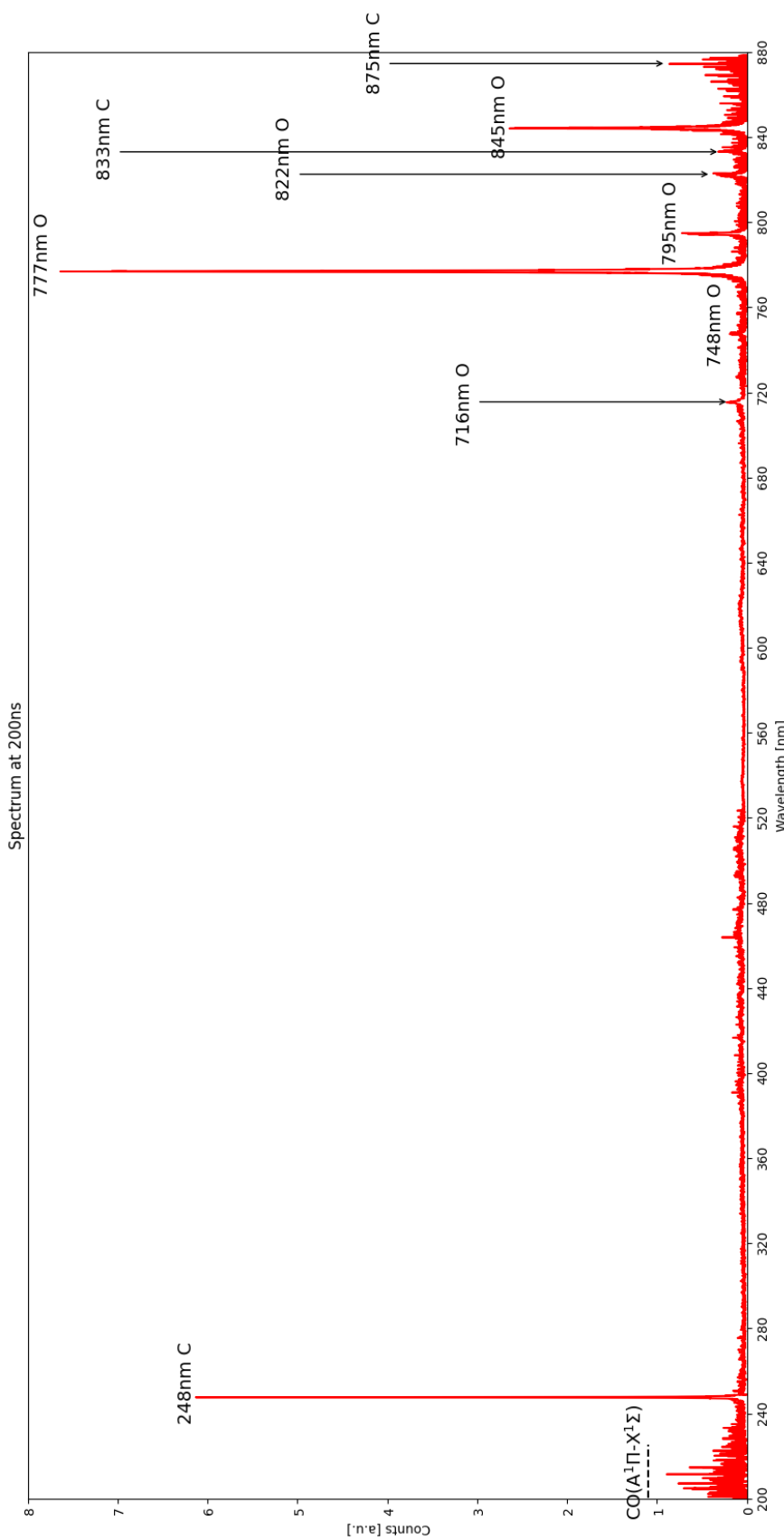


Figure 7.4: Spectrum 200ns after the start of the discharge for 200Hz unmatched in impedance, 5.5mm electrodes gap at the cathode, the MCP exposure time is set to 5 ns.

Bibliography

- [1] M. Ceppelli, T. P. W. Salden, L. M. Martini, G. Dilecce, and P. Tosi, “Time-resolved optical emission spectroscopy in co₂ nanosecond pulsed discharges,” *Plasma Sources Science and Technology*, vol. 30, p. 115 010, 2021. DOI: 10.1088/1361-6595/ac2411.
- [2] *Carbon dioxide vital signs*. [Online]. Available: <https://climate.nasa.gov/vital-signs/carbon-dioxide/?intent=121>.
- [3] O. Edenhofer, R. Pichs-Madruga, Y. Sokona, *et al.*, “Ipcc 2014: Climate change 2014: Mitigation of climate change. contribution of working group iii to the fifth assessment report of the intergovernmental panel on climate change,” Cambridge University Press, Cambridge, United Kingdom and New York, NY, USA, Technical Report, 2014.
- [4] K. E. Trenberth and J. T. Fasullo, “Tracking earth’s energy: From el niño to global warming,” *Surveys in Geophysics*, vol. 33, pp. 413–426, 2012. DOI: 10.1007/s10712-011-9150-2.
- [5] W. Zhong and J. D. Haigh, “The greenhouse effect and carbon dioxide,” *Weather*, vol. 68, no. 4, 2013.
- [6] R. L. Jaffe and W. Taylor, *The Physics of Energy*. 2018.
- [7] Energy Institute, *Statistical Review of World Energy*. Energy Institute, 2024.
- [8] R. Snoeckx and A. Bogaerts, “Plasma technology – a novel solution for co₂ conversion?” *Chemical Society Reviews*, vol. 46, p. 5805, 2017. DOI: 10.1039/c6cs00066e.
- [9] L. Colelli, N. Verdone, C. Bassano, V. Segneri, and G. Vilardi, “Optimization of power to gas system with cooled reactor for co₂ methanation: Start-up and shutdown tests with ru-based and ni-based kinetics,” *Energy*, vol. 312, p. 133 554, 2024, ISSN: 0360-5442. DOI: 10.1016/j.energy.2024.133554. [Online]. Available: <https://www.sciencedirect.com/science/article/pii/S0360544224033309>.

- [10] V. Cigolotti, M. Genovese, F. Piraino, and P. Fragiacomo, “Applications — overview of energy storage systems,” in *Encyclopedia of Electrochemical Power Sources (Second Edition)*, J. Garche, Ed., Second Edition, Oxford: Elsevier, 2025, pp. 47–59, ISBN: 978-0-323-95822-6. DOI: <https://doi.org/10.1016/B978-0-323-96022-9.00091-8>. [Online]. Available: <https://www.sciencedirect.com/science/article/pii/B9780323960229000918>.
- [11] M. Ceppelli, “Time-resolved optical diagnostics for plasma dissociation of co₂,” Tutor: Prof. Paolo Tosi, Ph.D. dissertation, University of Trento, 2022.
- [12] O. Cognography. “Energy density graph.” (2025), [Online]. Available: <http://www.olicognography.org/graph/energydensity.html>.
- [13] G. A. Olah, G. K. S. Prakash, and A. Goeppert, “Anthropogenic chemical carbon cycle for a sustainable future,” *Journal of The American Chemical Society*, vol. 133, pp. 12 881–12 898, 2011.
- [14] Carbon Recycling International, *Carbon recycling international*, 2025. [Online]. Available: <https://www.carbonrecycling.is/>.
- [15] F. Taccogna and G. Dilecce, “Non-equilibrium in low-temperature plasmas,” *The European Physical Journal D*, vol. 70, 2016. DOI: 10.1140/epjd/e2016-70474-0.
- [16] O. Biondo, C. Fromentin, T. Silva, V. Guerra, G. van Rooij, and A. Bogaerts, “Insights into the limitations to vibrational excitation of co₂: Validation of a kinetic model with pulsed glow discharge experiments,” *Plasma Sources Science and Technology*, vol. 31, p. 074 003, 2022. DOI: 10.1088/1361-6595/ac8019.
- [17] A. Berthelot and A. Bogaerts, “Modeling of co₂ splitting in a microwave plasma: How to improve the conversion and energy efficiency,” *The Journal of Physical Chemistry C*, vol. 121, no. 15, pp. 8236–8251, 2017. DOI: 10.1021/acs.jpcc.6b12840.
- [18] B. Zhang, H. Zuo, B. Wu, *et al.*, “Recent progress in co₂ splitting processes with non-thermal plasma-assisted,” *Journal of Environmental Chemical Engineering*, vol. 12, no. 6, p. 114 692, 2024, ISSN: 2213-3437. DOI: <https://doi.org/10.1016/j.jece.2024.114692>. [Online]. Available: <https://www.sciencedirect.com/science/article/pii/S2213343724028240>.

- [19] S. Heijkers, L. M. Martini, G. Dilecce, P. Tosi, and A. Bogaerts, “Nanosecond pulsed discharge for CO_2 conversion: Kinetic modeling to elucidate the chemistry and improve the performance,” *The Journal of Physical Chemistry C*, vol. 123, no. 19, pp. 12 104–12 116, 2019, ISSN: 1932-7447. DOI: 10.1021/acs.jpcc.9b01543. [Online]. Available: <https://doi.org/10.1021/acs.jpcc.9b01543>.
- [20] S. Paulussen, B. Verheyde, X. Tu, *et al.*, “Conversion of carbon dioxide to value-added chemicals in atmospheric pressure dielectric barrier discharges,” *Plasma Sources Science and Technology*, vol. 19, p. 034 015, 2010, ISSN: 0963-0252. DOI: 10.1088/0963-0252/19/3/034015.
- [21] A. Ozkan, A. Bogaerts, and F. Reniers, “Routes to increase the conversion and the energy efficiency in the splitting of CO_2 by a dielectric barrier discharge,” *Journal of Physics D: Applied Physics*, vol. 50, p. 084 004, 2017, ISSN: 0022-3727. DOI: 10.1088/1361-6463/aa562c.
- [22] T. Silva, N. Britun, T. Godfroid, and R. Snyders, “Optical characterization of a microwave pulsed discharge used for dissociation of CO_2 ,” *Plasma Sources Science and Technology*, vol. 23, p. 025 009, 2014, ISSN: 0963-0252. DOI: 10.1088/0963-0252/23/2/025009.
- [23] G. J. van Rooij, D. C. M. van den Bekerom, N. den Harder, *et al.*, “Taming microwave plasma to beat thermodynamics in CO_2 dissociation,” *Faraday Discussions*, vol. 183, pp. 233–248, 2015, ISSN: 1359-6640. DOI: 10.1039/c5fd00045a.
- [24] A. Indarto, D. R. Yang, J.-W. Choi, H. Lee, and H. K. Song, “Gliding arc plasma processing of CO_2 conversion,” *Journal of Hazardous Materials*, vol. 146, pp. 309–315, 2007, ISSN: 0304-3894. DOI: 10.1016/j.jhazmat.2006.12.023.
- [25] M. Ramakers, J. A. Medrano, G. Trenchev, F. Gallucci, and A. Bogaerts, “Revealing the arc dynamics in a gliding arc plasmatron: A better insight to improve CO_2 conversion,” *Plasma Sources Science and Technology*, vol. 26, p. 125 002, 2017, ISSN: 1361-6595. DOI: 10.1088/1361-6595/aa9531.
- [26] L. F. Spencer and A. D. Gallimore, “Efficiency of CO_2 dissociation in a radio-frequency discharge,” *Plasma Chemistry and Plasma Processing*, vol. 31, pp. 79–89, 2011, ISSN: 0272-4324. DOI: 10.1007/s11090-010-9273-0.

- [27] M. S. Moss, K. Yanallah, R. W. K. Allen, and F. Pontiga, “An investigation of co₂ splitting using nanosecond pulsed corona discharge: Effect of argon addition on co₂ conversion and energy efficiency,” *Plasma Sources Science and Technology*, vol. 26, p. 035 009, 2017, ISSN: 1361-6595. DOI: 10.1088/1361-6595/aa5b1d.
- [28] M. Budde, L. M. Martini, M. Ceppelli, S. Quercetti, and R. Engeln, “Absolute oh density measurements in a co₂–h₂o glow discharge by laser-induced fluorescence spectroscopy,” *Plasma Sources Science and Technology*, vol. 31, no. 5, p. 055 002, 2022. DOI: 10.1088/1361-6595/ac5ecc.
- [29] S. Tao, S. Guangsheng, Y. Ping, *et al.*, “An experimental investigation of repetitive nanosecond pulse breakdown in air,” *J. Phys. D: Appl. Phys.*, vol. 39, pp. 2192–2197, 2006. DOI: 10.1088/0022-3727/39/10/030.
- [30] Z. Zhao and J. Li, “Repetitively pulsed gas discharges: Memory effect and discharge mode transition,” *High Volt.*, vol. 5, no. 5, pp. 569–582, 2020.
- [31] T. Huiskamp, “Nanosecond pulsed streamer discharges part i: Generation, source-plasma interaction and energy-efficiency optimization,” *Plasma Sources Sci. Technol.*, vol. 29, 023002 (47pp), 2020. DOI: 10.1088/1361-6595/ab53c5.
- [32] C. Montesano, S. Quercetti, L. M. Martini, G. Dilecce, and P. Tosi, “The effect of different pulse patterns on the plasma reduction of co₂ for a nanosecond discharge,” *Journal of CO₂ Utilization*, vol. 39, p. 101 157, 2020. DOI: 10.1016/j.jcou.2020.101157.
- [33] C. Montesano, M. Faedda, L. M. Martini, G. Dilecce, and P. Tosi, “Ch₄ reforming with co₂ in a nanosecond pulsed discharge. the importance of the pulse sequence,” *Journal of CO₂ Utilization*, vol. 49, p. 101 556, 2021. DOI: 10.1016/j.jcou.2021.101556.
- [34] C. Montesano, T. P. W. Salden, L. M. Martini, G. Dilecce, and P. Tosi, “Co₂ reduction by nanosecond-plasma discharges: Revealing the dissociation’s time scale and the importance of pulse sequence,” *The Journal of Physical Chemistry C*, vol. 127, pp. 10 045–10 050, 2023. DOI: 10.1021/acs.jpcc.3c02547.
- [35] R. Engeln, B. Klarenaar, and O. Guaitella, “Foundations of optical diagnostics in low-temperature plasmas,” *Plasma Sources Science and Technology*, vol. 29, no. 6, p. 063 001, 2020.

- [36] U. Fantz, "Basics of plasma spectroscopy," *IOPscience*, 2006.
- [37] J. W. Daily, "Laser induced fluorescence spectroscopy in flames," *Progress in Energy and Combustion Science*, vol. 23, pp. 133–199, 1997, ISSN: 0360-1285.
- [38] O. Carrivain, M. Orain, N. Dorval, C. Morin, and G. Legros, "Experimental spectroscopic studies of carbon monoxide (co) fluorescence at high temperatures and pressures," *Applied Spectroscopy*, vol. 71, no. 10, pp. 2353–2366, 2017. DOI: 10.1177/0003702817709439. [Online]. Available: <https://journals.sagepub.com/home/asp>.
- [39] Avantes, *Avalight-dh-s deuterium-halogen light source*, Technical specifications and product details for the AvaLight-DH-S deuterium-halogen light source., 2024. [Online]. Available: <https://www.avantes.com>.
- [40] C. Montesano, "Experimental investigation of nanosecond pulsed discharges for CO₂ recycling," Philosophiae Doctor - Dottore di Ricerca, University/Institution Name, 2023.
- [41] I. Thorlabs, *Optical filters datasheet*, Technical datasheet for Thorlabs optical filters., 2024. [Online]. Available: <https://www.thorlabs.com>.
- [42] A. Kramida, Y. Ralchenko, J. Reader, and N. A. Team, *Nist atomic spectra database (ver. 5.9)*, <https://physics.nist.gov/asd>, Accessed: 2021-01-31, Gaithersburg, MD: National Institute of Standards and Technology, 2021.
- [43] R. W. B. Pearse, *The Identification of Molecular Spectra*. London, New York: Chapman and Hall Wiley, 1976.
- [44] P. H. Krupenie, "The band spectrum of carbon monoxide," N/A, Tech. Rep., 1966.
- [45] M. A. Johnson and J. Rostas, "Vibronic structure of the CO₂⁺ ion: Reinvestigation of the antisymmetric stretch vibration in the x⁻, a⁻, and b⁻ states," *Molecular Physics*, vol. 85, pp. 839–868, 1995.
- [46] D. Gauyacq, C. Larcher, and J. Rostas, "The emission spectrum of the CO₂⁺ ion: Rovibronic analysis of the band system," *Canadian Journal of Physics*, vol. 57, pp. 1634–1649, 1979.

- [47] M. L. da Silva and M. Dudeck, “Arrays of radiative transition probabilities for co₂-n₂ plasmas,” *Journal of Quantitative Spectroscopy and Radiative Transfer*, vol. 102, no. 3, pp. 348–386, 2006, ISSN: 0022-4073. DOI: 10.1016/j.jqsrt.2006.02.018. [Online]. Available: <https://www.sciencedirect.com/science/article/pii/S0022407306000240>.
- [48] J. Park, I. Henins, H. W. Herrmann, and G. S. Selwyn, “Neutral bremsstrahlung measurement in an atmospheric-pressure radio frequency discharge,” *Physics of Plasmas*, vol. 7, no. 8, pp. 3141–3144, Aug. 2000, ISSN: 1070-664X. DOI: 10.1063/1.874220. eprint: https://pubs.aip.org/aip/pop/article-pdf/7/8/3141/19249329/3141_1_online.pdf. [Online]. Available: <https://doi.org/10.1063/1.874220>.
- [49] E. Iordanova, N. de Vries, M. Guillemier, and J. J. A. M. van der Mullen, “Absolute measurements of the continuum radiation to determine the electron density in a microwave-induced argon plasma,” *Journal of Physics D: Applied Physics*, vol. 41, no. 1, p. 015 208, 2008. DOI: 10.1088/0022-3727/41/1/015208. [Online]. Available: <https://doi.org/10.1088/0022-3727/41/1/015208>.
- [50] S. Park, W. Choe, S. Y. Moon, and J. Park, “Electron density and temperature measurement by continuum radiation emitted from weakly ionized atmospheric pressure plasmas,” *Applied Physics Letters*, vol. 104, no. 8, p. 084 103, 2014. DOI: 10.1063/1.4866804. [Online]. Available: <https://doi.org/10.1063/1.4866804>.
- [51] R. Bazinette, J. Paillol, and F. Massines, “Optical emission spectroscopy of glow, townsend-like and radiofrequency dbds in an ar/nh₃ mixture,” *Plasma Sources Science and Technology*, vol. 24, no. 5, p. 055 021, 2015. DOI: 10.1088/0963-0252/24/5/055021. [Online]. Available: <https://doi.org/10.1088/0963-0252/24/5/055021>.
- [52] D. Z. Pai, S. Stauss, and K. Terashima, “Field-emitting townsend regime of surface dielectric barrier discharges emerging at high pressure up to supercritical conditions,” *Plasma Sources Science and Technology*, vol. 24, no. 2, p. 025 021, 2015. DOI: 10.1088/0963-0252/24/2/025021. [Online]. Available: <https://doi.org/10.1088/0963-0252/24/2/025021>.
- [53] A. Y. Nikiforov, E.-R. Ionita, G. Dinescu, and C. Leys, “Characterization of a planar 8 mm atmospheric pressure wide radiofrequency plasma source by spectroscopy

- techniques,” *Plasma Physics and Controlled Fusion*, vol. 58, no. 1, p. 014013, 2016. DOI: 10.1088/0741-3335/58/1/014013. [Online]. Available: <https://doi.org/10.1088/0741-3335/58/1/014013>.
- [54] Z. Navrátil, T. Morávek, J. Ráhel, J. Čech, O. Lalinský, and D. Trunec, “Diagnostics of pre-breakdown light emission in a helium coplanar barrier discharge: The presence of neutral bremsstrahlung,” *Plasma Sources Science and Technology*, vol. 26, no. 5, p. 055025, 2017. DOI: 10.1088/1361-6595/aa66b5. [Online]. Available: <https://doi.org/10.1088/1361-6595/aa66b5>.
- [55] J. Maillard, “Energy efficiency of co₂ conversion with nanosecond plasma discharges,” English, NNT: 2024UPAST043, tel-04807114, PhD Thesis, Université Paris-Saclay, 2024.